



**PREPERATION AND CHARACTERIZATION OF PLASMONIC
DYE-SENSITIZED SOLAR CELLS BASED ON Au@SiO₂ AND Ag@SiO₂
CORE-SHELL NANOPARTICLES FOR SOLAR ENERGY UTILIZATION**

Mohammed ADIL MOHAMMED MOHAMMED

**MSc. THESIS
PHYSICS DEPARTMENT**

**GAZI UNIVERITY
GRADUATE SCHOOL OF NATURAL AND APPLIED SCIENCES**

DECEMBER 2022

ETHICAL STATEMENT

I hereby declare that in this thesis study I prepared in accordance with thesis writing rules of Gazi University Graduate School of Natural and Applied Sciences;

- All data, information and documents presented in this thesis have been obtained within the scope of academic rules and ethical conduct,
 - All information, documents, assessments and results have been presented in accordance with scientific ethical conduct and moral rules,
 - All material used in this thesis that are not original to this work have been fully cited and referenced,
 - No change has been made in the data used,
 - The work presented in this thesis is original,
- or else, I admit all loss of rights to be incurred against me.

MOHAMMED ADIL MOHAMMED MOHAMMED

19/12/2022

GÜNEŞ ENERJİSİ KULLANIMI İÇİN Au@SiO₂ VE Ag@SiO₂
ÇEKİRDEK-KABUK NANOPARAÇACIKLARINA DAYALI PLAZMONİK BOYA-
SENSİTİZE GÜNEŞ PİLLERİNİN HAZIRLANMASI VE KARAKTERİZASYONU
(Yüksek Lisans Tezi)

Mohammed ADIL MOHAMMED MOHAMMED

GAZİ ÜNİVERSİTESİ
FEN BİLİMLERİ ENSTİTÜSÜ

Aralık 2022

ÖZET

Uzun vadeli çevresel ve ekonomik uygulanabilirliği sağlamak için artan enerji taleplerini yenilenebilir ve temiz kaynaklarla karşılamak çok önemlidir. Uygulanabilir bir yenilenebilir enerji kaynağı olarak güneş pillerinin geleceği, bu bileşenlerde yapılan verimlilik ve maliyet iyileştirmelerine bağlıdır. Boyaya duyarlı güneş pili (DSSC), güneş ışığı enerjisinden elektron üretmek için en etkili cihazlardan biridir. Avantajları, düşük maliyetli işlemeyi içerir. Çeşitli faydalarına rağmen, DSSC'ler diğer güneş pillerinden daha düşük bir güç dönüşüm verimliliğine (PCE) sahiptir. Yüksek verimli DSSC'ler oluşturmak için, ışık hasadı ve elektron taşınmasını artırma dahil olmak üzere farklı yöntemler mevcuttur. Bu tezde, sıvıda lazer ablasyon tekniği kullanılarak Au@SiO₂ ve Ag@SiO₂ çekirdek-kabuk nanoparçacıkları hazırlandı ve bu nanoparçacıklar Plazmonik Boyaya Duyarlı güneş pillerinde (DSSC) kullanıldı. DSSC'lerin akım-gerilim(I-V) karakteristik eğrileri hem karanlıkta hem de 100 mW/cm² altında gerçekleştirilmiş ve oda sıcaklığında birbirleriyle karşılaştırmalı deneysel sonuçlar elde edilmiştir. Au@SiO₂ ve Ag@SiO₂ çekirdek-kabuk NP'leri, sulu bir silika solüsyonunda darbeli lazer ablasyonu ile farklı lazer enerjileri (50 mJ, 100mJ, 150 mJ) kullanılarak hazırlandı. Sonuçlar, kullanılan lazer enerjisinin hazırlanan nanoparçacıkların yapısal özellikleri üzerindeki etkisini yüksek oranda göstermiştir ve bu da diğer özellikleri de etkilemektedir. Au@SiO₂ ve Ag@SiO₂ için XRD, artan lazer enerjisiyle kristallığın arttığını ve kristalit boyutunun arttığını gösterir. Transmisyon elektron mikroskobu, lazer enerjisiyle her iki NP türü için artan bir ortalama çap gösterir. UV-görünür absorpsiyon, lazer enerjisini artıran hafif bir kırmızı kayma ile her iki NP için de önemli plazmonik rezonans gösterir. Metal NP'lerin güneş pili katmanlarına dahil edilmesi, özellikle plazmonik frekansta aktif katmanın absorpsiyonunu artırarak verimliliklerini artırır. Farklı NP'lerin etkisi incelendi ve nanopartikül içermeyen çıplak güneş pili ile karşılaştırıldı. Au@SiO₂ ve Ag@SiO₂ NP'lerinden oluşan DSSC güneş pili, özelliklerinde önemli bir gelişme gösterir. Sonuçlar, Au@SiO₂ ve Ag@SiO₂'nin seçici saçılma faktörleri olarak kullanılabilirliğini ve verimli DSSC'ler vaat ettiğini ortaya koydu.

Bilim Kodu : 20227
Anahtar Kelimeler : Çekirdek kabuğu; Nanoyapı; Lazer ablasyon; plazmon; Boyaya duyarlı güneş pilleri.
Sayfa Adedi : 109
Danışman : Prof.Dr. Mehmet Mahir BÜLBÜL
İkinci Danışman : Dr. Odai N. SALMAN

PREPERATION AND CHARACTERIZATION OF PLASMONIC
DYE-SENSITIZED SOLAR CELLS BASED ON Au@SiO₂ AND Ag@SiO₂
CORE-SHELL NANOPARTICLES FOR SOLAR ENERGY UTILIZATION

(MSc. Thesis)

Mohammed ADIL MOHAMMED MOHAMMED

GAZI UNIVERSITY

GRADUATE SCHOOL OF NATURAL AND APPLIED SCIENCES

December 2022

ABSTRACT

It is crucial to fulfill rising energy demands with renewable and clean sources to ensure long-term environmental and economic viability. The future of solar cells as a viable renewable energy source hinges on the efficiency and cost improvements made these components. The dye-sensitized solar cell (DSSC) is one of the most effective devices to producing electrons from solar light energy. Their benefits include low-cost processing. Despite their various benefits, DSSCs have a lower power conversion efficiency (PCE) than other solar cells. Different methods exist to create highly efficient DSSCs, including enhancing light harvesting and electron transport. In this thesis, Au@SiO₂ and Ag@SiO₂ core-shell nanoparticles were prepared using the laser ablation technique in liquid and these nanoparticles were employed in Plasmonic Dye Sensitized solar cells (DSSC). Current-voltage(I-V) characteristic curves of DSSCs were performed both in the dark and under 100 mW/cm² and obtained experimental results compared to each other at room temperature. Au@SiO₂ and Ag@SiO₂ core-shell NPs were prepared using different laser energies (50 mJ,100mJ,150 mJ) by pulsed laser ablation in an aqueous silica solution. The results highly showed the effect of the used laser energy on the structural properties of the prepared nanoparticles, which in turn affect the other properties. The XRD for Au@SiO₂ and Ag@SiO₂ shows that the crystallinity enhanced, and the crystallite size increased with increased laser energy. The transmission electron microscopy shows an increasing average diameter for both NPs types with the laser energy. The UV-visible absorbance shows significant plasmonic resonance for both NPs, with a slight red shift increasing the laser energy. Incorporating metal NPs into solar cell layers enhances their efficiency by increasing the active layer's absorption, especially at the plasmonic frequency. The effect of the different NPs was examined and compared with the bare-solar cell without nanoparticles. The DSSC solar cell composed of Au@SiO₂ and Ag@SiO₂ NPs shows significant enhancement in their characteristics. The results revealed that Au@SiO₂ and Ag@SiO₂ could be employed as selective scattering factors, promising efficient DSSCs.

Science Code : 20227
Key Word : Core-shell; Nanostructure; Laser ablation; Plasmon; Dye-sensitized solar cells.
Page Number : 109
Supervisor : Prof. Dr. Mehmet Mahir BÜLBÜL
Co-Supervisor : Dr. Odai N. SALMAN

ACKNOWLEDGMENT

We praise and thank ALLAH as it should be for the majesty of his countenance and the greatness of his authority. At first, we ask ALLAH's forgiveness and ask Him to accept our deeds and our efforts and be pleased with them on our behalf. Then we pray for the most honorable of creation, our prophet Muhammad - may God bless him and grant him peace - and his family.

Here, I would like to thank the Gazi university administration, represented by the university director, Prof. Dr. Musa YILDIZ, and the dean of the Faculty of Sciences, Prof. Dr. Suat KIYAKN. And the head of the physics department, Prof. Dr. Bülent KUTLU.

All credit and thanks also go to my professors who supervised my thesis and supported me after ALLAH, Prof. MEHMET MAHİR BÜLBÜL, and Co-supervisor Dr. ODAI N. SALMAN. Without them, I would not have had this much knowledge and awareness, and I would not be standing here now. I would also like to extend my sincere thanks to all teachers who encouraged me throughout the period I lived at the university, especially Prof. ŞEMSETTİN ALTINDAL and his team of teachers, students, and employees.

Then I would like to extend my thanks and gratitude to the following:

All honorable members of my thesis discussion committee:

- 1- Prof.Dr. Mehmet Mahir BÜLBÜL (I Danışman)
- 2- Dr. ODAI N. SALMAN (II Danışman)
- 3- Prof.Dr. Şemsettin ALTINDANL
- 4- Prof.Dr. Sebahaddin ALPTEİN

Honorable members of the jury, thanks for their guidance and advice.

In the end, I cannot forget to thank my mother, father, and my beloved wife, who supported me in my journey and was patient. She was the wife, friend, and beloved. I thank my daughters and brothers for supporting me throughout the study period and preparing for this discussion, and thanks to my sheik and teacher, Sidqi Al-Nuaimi, and all my friends and colleagues for their support, especially Abdul Majeed ALBadri , Salman Aziz, Murat Ulusoy and Ahmed Demir.

Thanks also to the Photonic Laboratories of Gazi University and the University of Technology, Department of Applied Sciences, Physics Branch, for their cooperation while conducting experiments and examinations for this thesis.

TABLE OF CONTENTS

	Page
ÖZET	iv
ABSTRACT.....	v
ACKNOWLEDGMENT.....	vi
TABLE OF CONTENTS.....	vii
LIST OF TABLES	xi
LIST OF FIGURES	xii
LIST OF SYMBOLS AND ABBREVIATIONS	xvi
1. INTRODUCTION.....	1
1.1. The Dye Sensitized Solar Cells (DSSCs).....	5
1.2. Components of the DSSC	6
1.3. The fundamental Plasmonic and Physical Properties of Surface Plasmons	7
1.3.1. The propagating of surface plasmon resonance (PSPR)	8
1.3.2. The localized surface plasmon resonance (LSPR)	9
1.3.3. Plasmonic effect in photovoltaic cell.....	10
1.3.4. Noble Metal Nanoparticles	11
1.4. Aims of the work.....	14
2. LITERATURE REVIEW	15
3. THEORETICAL BACKGROUND.....	21
3.1. The Dye Sensitized Solar Cells (DSSCs).....	21
3.2. Solar cells Basic principle	21
3.2.1. Performance of photovoltaic solar cells	22
3.2.2. Solar cells and their efficiency	24
3.3. Design and construction of a DSSCs	25
3.3.1 Transparent and conductive substrate of DSSCs.....	25

	Page
3.3.2. Transparent and conductive substrate.....	26
3.3.3. Working electrode	26
3.3.4. The sensitizer of dye	26
3.3.5. The electrolyte	27
3.3.6. Counter electrode(CE).....	28
3.4. DSSC's Working Principles	29
3.4.1. Plasmonic dye-sensitized solar cell (PDSSC)	32
3.4.2. Plasmonic metal nanoparticles	32
3.4.3. Methods of metal nanoparticle synthesis.....	35
3.5. The Mechanisms of Laser Liquid Ablation	40
3.5.1. The mechanisms of Laser ablation using bulk Metal targets in liquid.....	40
3.5.2. Mechanism of Thermal Evaporation	40
3.5.3. Mechanism of explosive ejection	41
3.5.4. Physical and chemical changing processing over time in LAL. For t less than zero: Pulse infiltration in the solution	42
3.6. Laser Ablation in Liquid-Formed Nanomaterials Applications.....	44
3.6.1. Noble Metal NPs functionalized for bio applications	44
3.6.2. Semiconductor NPs for applications in luminescence	44
3.6.3. Applications for Surface Enhanced Raman Scattering (SERS) Detection Using NP Thin – Films	44
3.6.4. Nano fertilizers for Increasing Seed Germination and Growth.....	44
3.7. Nanoparticle characterization.....	45
3.7.1. X-Ray Diffraction (XRD) characterization techniques	45
3.7.2. Calculation of crystal grains' size	46
3.8. Optical Characterization Techniques	49
3.8.1. The UV-Visible spectroscopy	49
3.8.2. Photoluminescence (PL) spectroscopy characterization techniques	51

	Page
3.8.3. Transmission electron microscopy (TEM)	52
3.9. Solar Simulator.....	53
4. EXPERIMENTAL PROCEDURE	55
4.1. Preparation of Metal@core-shell (Au@SiO ₂ and Ag@SiO ₂) Nanoparticles	56
4.1.1. The technique for pulse laser ablation in liquid	56
4.2. Materials.....	57
4.2.1. Materials for Laser Ablation Technique.....	57
4.3. Dye-sensitized solar cell materials (DSSC)	58
4.3.1. TiO ₂ paste	58
4.3.2. Dye type N719.....	58
4.2.3. Platine paste.....	58
4.2.4. (FTO) coated glass with fluorine-doped tin oxide.....	59
4.2.5. Thermoplastic sealant	59
4.4. Experimental Procedure to Prepare Core-Shell Nanostructure.....	59
4.4.1. LAL Experimental Procedure.....	59
4.4.2. Film deposition	62
4.4.3. The screen-printing technique	62
4.5. Dye-Sensitized Solar Cell (DSSC) Preparation	64
4.6. Device and Sample Characterization	68
4.6.1. Spectrophotometer	68
4.6.2. Photoluminescence (PL).....	68
4.6.3 Optical Microscope.....	68
4.6.4. The analysis of X-ray diffraction (XRD)	68
4.6.5. Transmission electron microscopy (TEM)	69
4.7. The Dye-Sensitized Solar Cells (DSSCs) Characterization.....	69
5. RESULTS AND DISCUSSIONS	71

	Page
5.1. XRD analysis results	71
5.1.1. XRD analysis results for Ag@SiO ₂ Nanoparticles prepared by Laser Ablation Technique	71
5.1.2. XRD analysis results for Au@SiO ₂ Nanoparticles prepared by Laser Ablation Technique	73
5.2. Optical Properties Results	76
5.2.1. Optical properties of Ag@SiO ₂ nanoparticles.....	76
5.2.2. Optical characterization for Au@SiO ₂ nanoparticles	78
5.3. Transmission Electron Microscope (TEM).....	82
5.3.1. TEM for Ag@SiO ₂	82
5.3.2. TEM for Au@SiO ₂	84
5.4. Plasmon Dye-Sensitized Solar Cell (PDSSC) Results.....	86
5.5. Conclusion	90
REFERENCE.....	93
CURRICULUM VITAE	109

LIST OF TABLES

Table	Page
Table 1.1. Summarizes some properties of gold and silver metals.....	13
Table 5.1. Summarizes the results of the XRD measurement for Ag@SiO ₂	72
Table 5.2. Summarizes the results of some XRD calculations for the (111) plane of Ag@SiO ₂	72
Table 5.3. Results for XRD measurement for Au@SiO ₂	74
Table 5.4. Shows the results of some XRD calculations for the (111) plane of Au@SiO ₂	75
Table 5.5. Summarizes the results of the energy gap values estimated from the UV-Vis and PL measurements	78
Table 5.6. Results of the energy gap values estimated from the UV-Vis and PL measurements	81
Table 5.7. The characteristics parameters for the fabricated DSSC loaded with the Ag@SiO ₂ and Au@SiO ₂	90

LIST OF FIGURES

Figure	Page
Figure 1.1. Diagram explain the Classification of solar cell generation.....	2
Figure 1.2. S1. Best Research-Cell Efficiencies	3
Figure 1.3. Dye-sensitized nanocrystalline solar cells: structure and operation principle	6
Figure 1.4. (a) Recent publications in the field of "plasmonic plus solar cell" that is mentioned here, as well as the distribution of these publications, (b) by field and (c) by document type. Data came from Scopus, a database of abstracts and citations that experts carefully put together	7
Figure 1.5. SPR waves (a) SPR waves moving along the boundary between the dielectric material and metal, and (b) field size across the boundary and perpendicular to the direction of propagation. The magneto-optic SPR effect demonstrates the directed magnetic field parallel to the metal-dielectric interface along the y-axis	9
Figure 1.6. A graphical view of localized surface plasmon resonance for a plasmonic nanosphere	10
Figure 1.7. Shows thin-film solar cells with plasmonic shapes that trap light.	11
Figure 1.8. Describe Plasmonic nanostructures for solar energy conversion	12
Figure 3.1. An illustration of the photovoltaic effect.....	21
Figure 3.2. Silicon photovoltaic cell (a) in both its dark and illuminated J-V states; (b) An illustration of a J-V curve that is illuminated, together with a voltage-dependent output power density curve that highlights the short-circuit point (0, J_{sc}), open-circuit point (0, V_{oc}), and maximum power point (P_{max}); (V_{mp} , J_{mp})	22
Figure 3.3. The solar cell's J-V characteristic	23
Figure 3.4. The effect of (a) resistance series (R_s) and (b) resistance shunt (R_{sh}) on the shape curve for I-V	24
Figure 3.5. Structure and components of DSSCs	25
Figure 3.6. A diagram demonstrates how a DSSC operates.	29
Figure 3.7. Timescales of various processes in DSSC.....	31

Figure	Page
Figure 3.8. Shows estimated the extinction (black), absorption (red), and scattering (blue) spectra for a) spherical, b) cuboid, c) tetrahedral, d) octahedral, and e) triangular plate-shaped Ag nanoparticles. Black, red, and f) red extinction spectra of rectangular bars with 2, 3, and 4 aspect ratios (blue)	34
Figure 3.9. Different methods exist for fabricating substrates.....	35
Figure 3.10. Top-down (shown in the photographs with a green backdrop) and bottom-up (not shown) perspectives are depicted schematically (images with pale yellow background) methods for creating nanoparticles	36
Figure 3.11. Brief summary of bottom-up and top-down techniques.....	36
Figure 3.12. TEM pictures, average and standard deviations of Pd sizes (Palladium) Laser ablation in water at (a) 532 nm, 8.92 J/ cm ² , (b) 532 nm, and 19.90 J cm ⁻² , (c) 1064 nm, 8.92 J cm ⁻² , (d) 1064 nm, 19.90 J cm ⁻² , and (e) 355 nm, 0.10 J cm ⁻² produced nanoparticles of different sizes and shapes ...	38
Figure 3.13. Shows that nanostructures can be created using either bottom-up or top-down manufacturing processes	39
Figure 3.14. Laser ablation's interaction effects	41
Figure.3.15. Diagrammatic depictions of nanodroplet ejection and nanostructure production	42
Figure 3.16. LaL timeline sketch with ns pulse ablation.	43
Figure 3.17. A Diffract Meter Schematic Diagram with Four Circles	45
Figure 3.18. Instruments for X-Ray Diffraction	46
Figure 3.19. A crystalline powder example's grain size and crystallite distribution are depicted in this schematic illustration	47
Figure 3.20. Schematic of UV-Vis spectrophotometer's main components.	49
Figure 3.21. Transmit	50
Figure 3.22. Displayed Organic (a) and inorganic (b) materials: PL reactions (direct bandgap). Some of the abbreviations used are internal conversion (IC), phosphorescence (P), absorption (A), fluorescence (F), intersystem crossover (ISC), emission (e), and bandgap (E _g). The "kinetic energy" of electrons or holes is represented by the letters "E" and "k," moment vector, respectively	51
Figure 3.23. Essential Parts of the TEM.....	53
Figure 4.1. Flowchart of the experiment Works	55

Figure	Page
Figure 4.2. Shows PLAL system setup for the experimental	56
Figure 4.3. Optical emission from the laser interaction with the Au target.....	57
Figure 4.4. Gold target ounce from PAMP and plate target after drawing by draw machine	57
Figure 4.5. Illustrate the Au plate when pulsed by laser with flounce 50 J/cm^2	60
Figure 4.6. Nanoparticle solution.....	61
Figure 4.7. Centrifuge process	61
Figure 4.8. Diagram of the method for preparation for Au@SiO ₂ and Ag@SiO ₂ films, respectively	62
Figure 4.9. Optical microscope image of 45T	63
Figure 4.10. Screens (20 x 30 cm) with wood frames and 45T	63
Figure 4.11. TiO ₂ film deposited by 45T screen printing	64
Figure 4.12. Flow chart of Dye sensitized solar cell preparation.	65
Figure 4.13. Coating the blocking TiO ₂ Layer	65
Figure 4.14. FTO-glass plates were cut into 2.5 x 2 cm pieces with two holes drilled into each piece.....	66
Figure 4.15. Doctor blade technique.....	67
Figure 4.16. (a) Design of thermoplastic seal, and (b) a photograph of a dye sensitized solar Cell.....	67
Figure 5.1. XRD pattern of nanoparticles Ag@SiO ₂ core shell prepared using laser ablation technique	71
Figure 5.2. Crystallite size verse laser energy for Ag@SiO ₂ NPs.....	73
Figure 5.3. XRD pattern of Au@SiO ₂ core-shell nanoparticles prepared by laser ablation technique	74
Figure 5.4. Crystallite size versus laser energy for Au@SiO ₂ NPs.....	75
Figure 5.5. Absorbance relates to the wavelength of Ag@SiO ₂ core-shell nanoparticles for different laser energies. The inset shows the images of Ag@SiO ₂ samples.....	76
Figure 5.6. Optical energy bandgap for Ag@SiO ₂ nanoparticles core-shell prepared at different laser energies.	77

Figure	Page
Figure 5.7. The photoluminescence (PL) spectra of Ag@SiO ₂ core-shell NPs at various laser Powers.....	78
Figure 5.8. Absorbance relates to the wavelength of Au@SiO ₂ core-shell nanoparticles for different laser energies. The inset shows the images of Au@SiO ₂ samples.....	79
Figure 5.9. Optical energy bandgap for Au@SiO ₂ nanoparticles core-shell prepared at different laser energies.	80
Figure 5.10. The photoluminescence (PL) spectra of Au@SiO ₂ core-shell NPs at various laser powers.....	81
Figure 5.11. Transmission electron micrograph (TEM) and size distribution chart of laser- ablated Ag@SiO ₂ core-shell NPs synthesis at (1) 50, (2)100, and (3)150 mJ.....	82
Figure 5.12. Average diameter against laser energy for Ag@SiO ₂	83
Figure 5.13. TEM picture of Ag@SiO ₂ , which distinctly shows the presence of SiO ₂ Nano Shell	83
Figure 5.14. Transmission electron micrograph (TEM) and size distribution chart of laser- ablated Au@SiO ₂ core-shell nanoparticles synthesis at 50, 100, and 150 mJ	84
Figure 5.15. Average diameter against laser energy for Au@SiO ₂	85
Figure 5.14. TEM picture of Au@SiO ₂ , which distinctly shows the presence of SiO ₂ Nano shell	85
Figure 5.15. (A)I-V characteristics at dark and under illumination for the fabricated DSSC, (B) DSSC loaded with the Ag@SiO ₂ , (c) Au@SiO ₂ loaded	86
Figure 5.16. P-V characteristics under illumination for the fabricated DSSC (A), DSSC loaded with Ag@SiO ₂ (B) and with Au@SiO ₂ (c).....	87
Figure 5.17. Ln(I) versus V at dark and under illumination for the fabricated DSSC (A), DSSC loaded with Ag@SiO ₂ (B) and with Au@SiO ₂ (C).....	88
Figure 5.18. Ln (I) versus V for the dark condition at the two regions for the fabricated DSSC (A), DSSC loaded with Ag@SiO ₂ (B) and with Au@SiO ₂ (C).....	89

LIST OF SYMBOLS AND ABBREVIATIONS

The symbols and abbreviations used in this study are presented below along with their explanations.

Symbols	Descriptions
A°	Angstrom
AM	Air mass
AuNP	Gold nanoparticle
AuNR	Gold nanorod
AuNW	Gold nanowire
AgNP	Silver nanoparticle
AgNW	Silver nanowire
Au@SiO₂	Gold-silica-core-shell nanoparticle
Ag@SiO₂	Silver-silica-core-shell nanoparticle
CIGS	Copper indium gallium selenide
CTAB	Cetyltrimethylammonium bromide
c-Si	Crystalline silicon
CZTS	Copper zinc tin sulfide
CB	Conduction band
CdTe	Cadmium tellurium
CE	Counter Electrode
DSSC	Dye Sensitized Solar Cell
-ve	Negative charge
+ve	Positive charge
FTO	Fluorine-doped tin oxide
FF	Fill factor
HOMO	Highest occupied molecular orbital
HTM	Hole transporting material
I₃⁻/I⁻	triiodide/iodide
IPCE	Incident photon conversion efficiency
ITO	Indium-doped oxide

Symbols	Descriptions
I-V	Current-voltage
I_{sc}	Short circuit current
J_{sc}	Short-circuit current density
LUMO	Lowest unoccupied molecular orbital
LSPR	Localized surface plasmon resonance
NIR	Near-infrared
OPV	Organic photovoltaic
P3HT	Poly(3-hexylthiophene-2,5-diyl)
PEDOT	Poly(3,4-ethylene dioxythiophene)
PDSSC	Plasmonic dye sensitized solar cell
PV	Photovoltaic
PEC	Photoelectrochemical conversion
P_{in}	Solar power incident
P_m	Maximum power
PL	Photoluminescence
QD	Quantum dot
QDSC	Quantum dots solar cells
Si	Silicon
SiO₂	Silicon dioxide(silica)
TCO	Transparent conductive oxide
TiO₂	Titanium dioxide
TEM	Transmission electron microscopy
m²	Meter square
m³	Meter cubic
nm	nanometer
UV-vis	Ultraviolet-visible
VB	Valence band
WE	Working electrode
XRD	X-ray diffraction

1. INTRODUCTION

Since the increasing population necessitates the utilization of energy in its many guises, researchers working in the field of energy are concentrating on the process of extracting energy from a variety of different sources. The use of nonrenewable energy sources like fossil fuels is coming to an end, and these resources will not be able to be replaced in our lifetimes [1].

As a result of the emission of carbon dioxide, which is one of the primary contributors to both global warming and global climate change, depleted (non-renewable) energy sources using fossil fuels (such as coal, oil, and gas) pose a threat to both the globe and humanity [2]. Three-quarters of the world's electricity comes from nonrenewable sources that cannot be reused or recycled [3].

In addition to the recent developments in the world that prompted many European countries to turn to clean energy alternatives, the necessity of speeding up the transition to these alternatives, including solar energy, moved fast to change this fact [4].

Solar cell technology can convert solar energy to electrical energy as humanity's dependence on electricity increases. Solar energy is enormous, providing approximately 10,000 times more energy than the world's daily energy needs [5].

Every day, the Earth gets so much energy from the sun that we are lucky to be able to use it with solar cell technology. Although solar energy is free, the technologies required to convert and store it are very expensive, making it difficult for more people to access it [6]. Solar harvesting has evolved since the 18th century. Edmond Becquerel discovered photovoltaics in 1839 [7].

Applications that utilize solar energy harvesting begin with this effect. Photovoltaics are photoactive devices optimized for the conversion of light energy into electricity. When light is absorbed by a semiconductor, a voltage is produced. The photovoltaic effect is the name for this phenomenon [8-10].

Based on this effect, Solar cell generations can be roughly put into three groups based on their material properties and how long they have existed [9]. (Figure 1.1) shows the generation of solar cells.

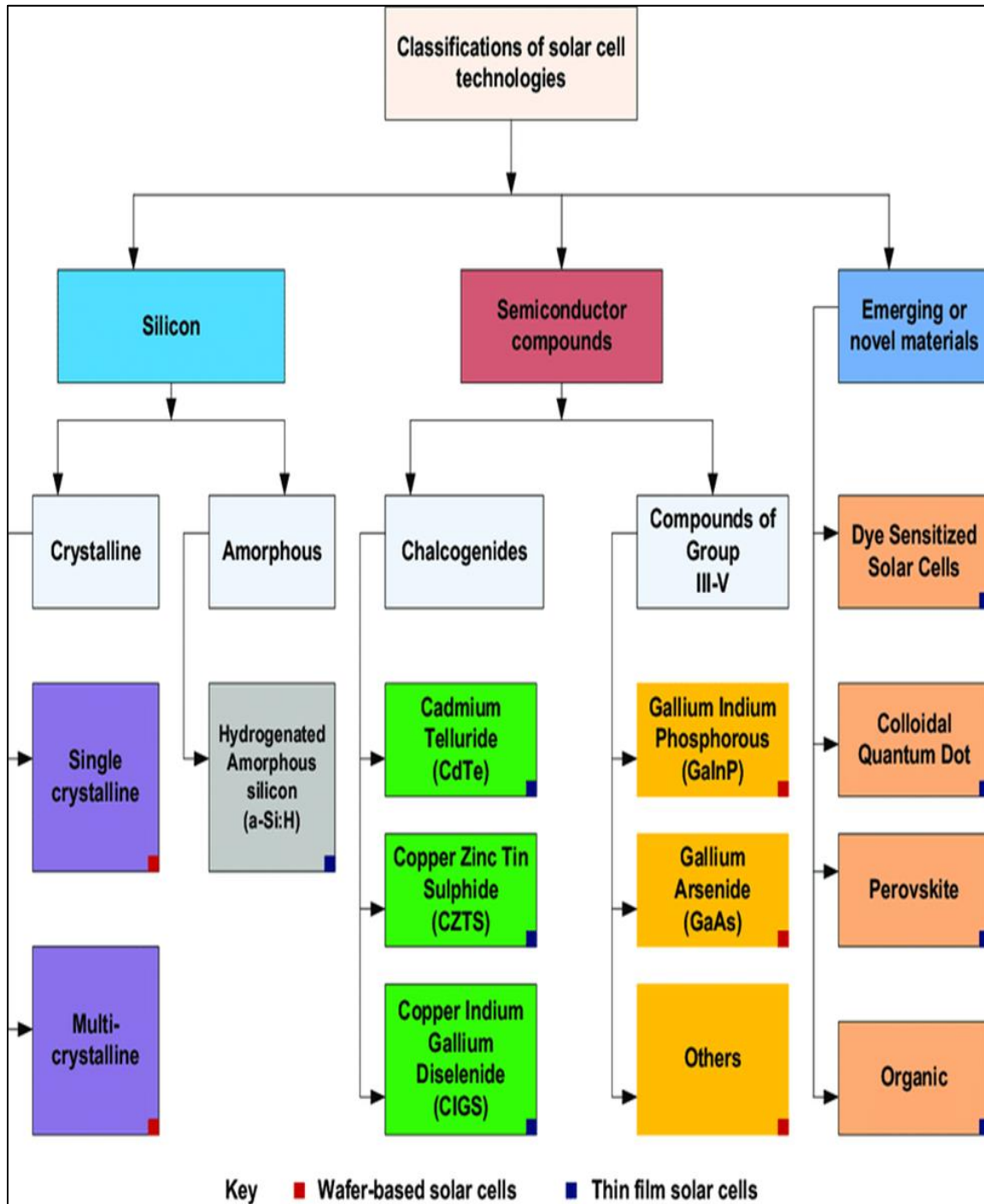


Figure 1.1. Diagram explain the Classification of solar cell generation [9]

The development of solar technology has been constant. It has flourished with diversification

in matrices and shapes, reaching a record efficiency at a laboratory scale of 47.1% (S1. Best Research-Cell Efficiencies) [11].

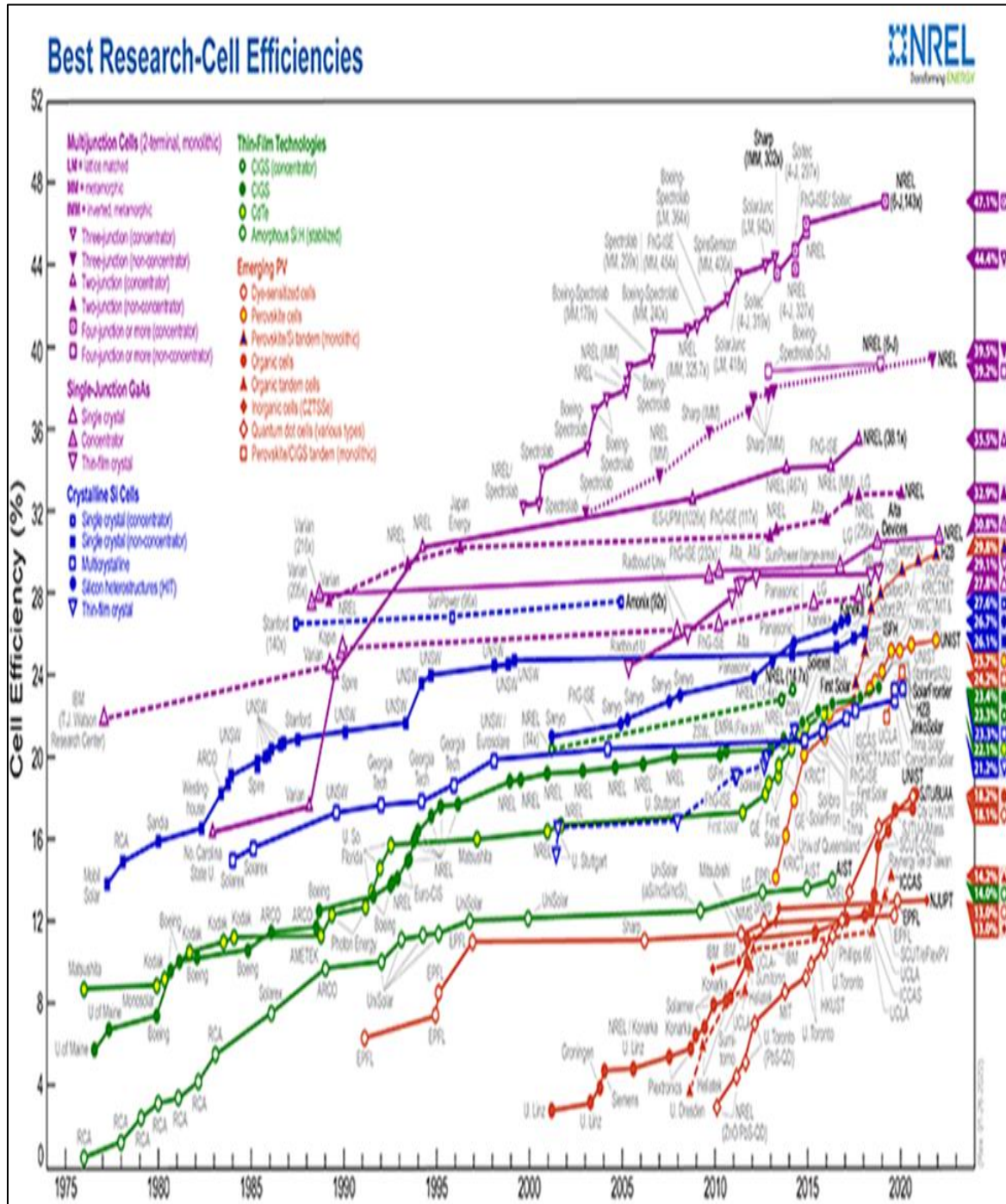


Figure 1.2. S1. Best Research-Cell Efficiencies[11]

Different types of photovoltaics have been created since, which can be grouped into different generations depending on their characteristics:

The First-generation: These solar cells are constructed from crystalline silicon wafers. This technology uses the most expensive method of generating pure Silicon crystal since it is made from silicon crystals (c-Si). These solar cells have the highest commercial efficiency that utilized everywhere [12]. Approximately 80% of the market for solar cells consists of monocrystalline cells. According to Zhao et al. (1998), the efficiency of honeycomb-structured polycrystalline solar cells is 19.8%. Polycrystalline solar cells are less efficient than crystalline solar cells [13].

1. Solar cells with single crystalline
2. Solar cells with polycrystalline

The Second-generation (the technology of thin film - solar cells): Since the technique of Si crystal wafer primarily uses Si (pure crystalline), it is expensive. The thin film solar cells that are most effective include Based on the molecules CdTe and Cu(In, Ga)(S, Se)₂ (CIGSSe), referred to as second-generation thin polycrystalline films [14]. The difficulty with these materials is lowering the price. However, in terms of solar energy conversion costs per watt, they are produced in the Earth's crust by expensive and scarce toxic materials, such as In, Ga, Te, and other concerns, such as CD [15]. New materials having characteristics have emerged in recent years. Furthermore, developed a keen interest in photovoltaic applications; plentiful and non-toxic metals have been suggested for the primary second-generation CdTe and CIGSSe-based solar cells [16].

The Third generation: This new generation of photovoltaic cell technology refers to solar cells with a power efficiency greater than the Shockley-Quisser limit of 31-41% [17]. This generation of solar cells consists of [18]:

- a) CZTS solar cells, including materials CZTSe and CZTSSe
- b) Dye-sensitized solar cells
- d) The Quantum Dot (QD) solar cells
- e) Perovskite solar cells
- f) Organic solar cells

These solar cell generations have low power conversion efficiencies compared to silicon-based and thin-film solar cells. Nonetheless, it has distinct advantages, such as low processing costs and minimal environmental impact, which have led to extensive research and development in this field [19].

1.1. The Dye Sensitized Solar Cells (DSSCs)

(DSSCs) are a good alternative to (pn junction photovoltaic) devices in point of view technical and financial. In the 1970s, he did a lot of research on ZnO single crystals, but the (ZnO) layer on his DSSCs does not absorb much light, so they are not very good [20-21]. Moreover, it can be made better by making it more porous. The first good modern DSSCs, called Grätzel cell, were made by O'Regan and Grätzel at the University of California, Berkeley, in 1991. They had a power conversion efficiency of 7.2% [22].

The popularity of dye-sensitive solar cells has increased significantly. As was already said, each of the solar cell technologies described has some drawbacks. Proper charge domain ordering is a problem for OPVs; moisture sensitivity and stability are problems for PSCs. For DSSCs to operate more effectively, photosensitive materials must have a wide absorption spectrum. Overall, DSSC performed best in the natural outdoor environment [3]. DSSCs generate significant amounts of power throughout the day regardless of the angle of light incidence, even when worked under low light levels [23].

Single-molecule properties determine the photophysical performance of DSSCs. Because of this, it is easy to change at the molecular level by changing the structure of the molecules and adding replacements.

Even when their moisture is present, DSSCs are stable and perform well in challenging circumstances like low temperatures and intense light levels [24-26].

So, DSSC is still promising ways to make solar cells, and both practical and theoretical research is still going on to make it even better. Most sensitizers are made with functional groups like (-B(OH)₂, -COOH, -PO₃H₂, and) to make sure they absorb light well [26-28].

1.2. Components of the DSSC

The Dye Sensitizer Solar Cell consists of four main parts [3].

1. Working electrode (also known as a photoelectrode or, more broadly, a semiconductor)
2. Dye sensitizer
3. Electrolyte
4. Counter electrode

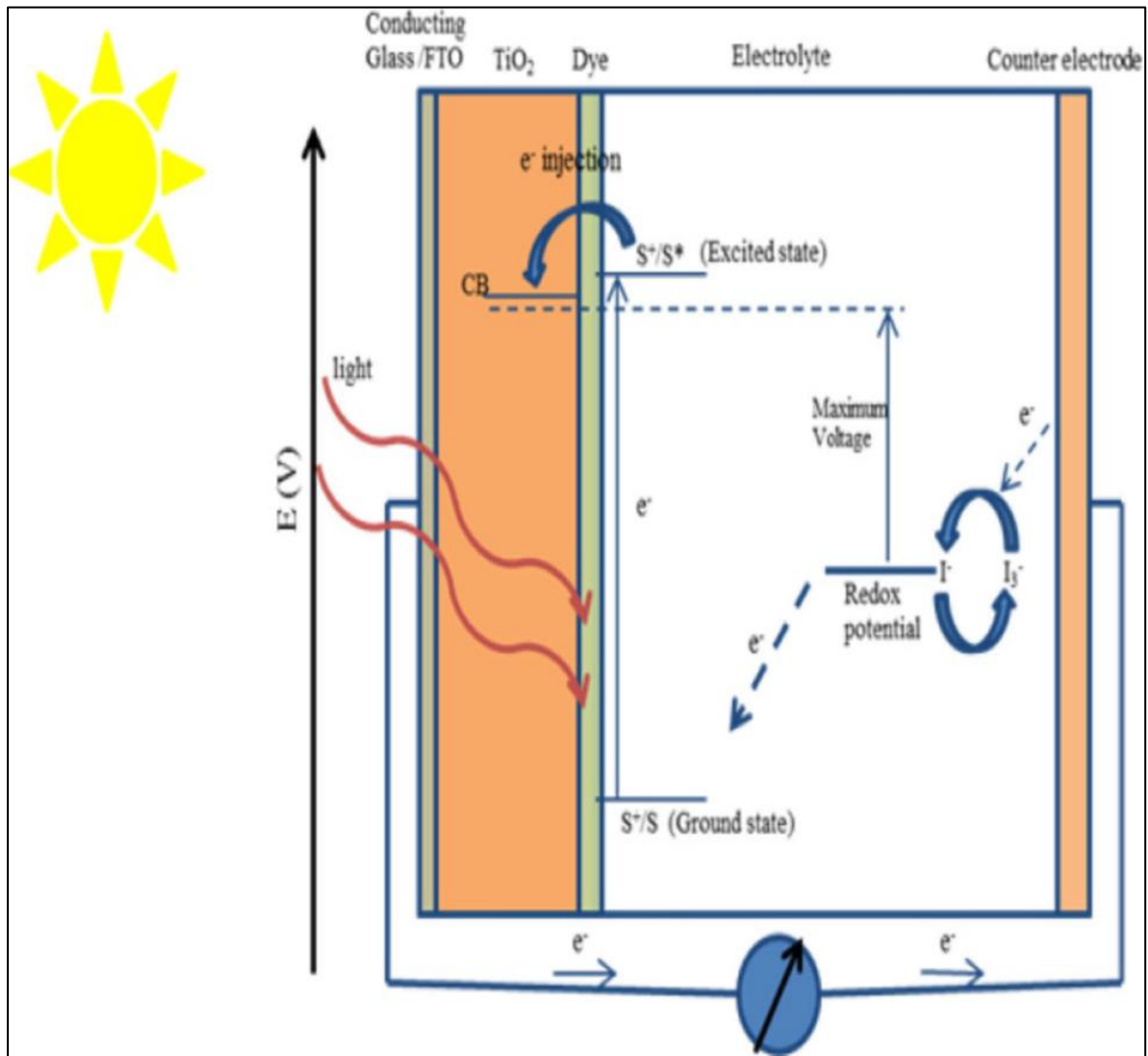


Figure 1.3. Dye-sensitized nanocrystalline solar cells: structure and operation principle [3]

DSSC represents a major advanced technology. Because of its inexpensive use of renewable energy sources, its numerous improvements have received a great deal of attention.

Plasmonic Dye-Sensitized Solar Cells (PDSSC) are a brighter option for solar energy conversion, with the highest absorption values compared to other photovoltaic systems.

Plasmonic dye - sensitized solar cells (PDSSCs) get lots of attention and great interest because to their cheap price and ease of production under mild conditions. PDSSC can be a flexible solar cell for indoor applications under normal lighting conditions [3,28-32].

1.3. The fundamental Plasmonic and Physical Properties of Surface Plasmons

Plasmonic nanostructure applied to solar cells has recently emerged as a rapidly expanding research area, significantly increasing between 2007 and 2021 (peaking in 2015). Furthermore, it can be seen by looking at the number of published studies shown in (Figure 1.4) These results came from searching the Scopus database with the terms “plasmonic and solar cell,” respectively [33].

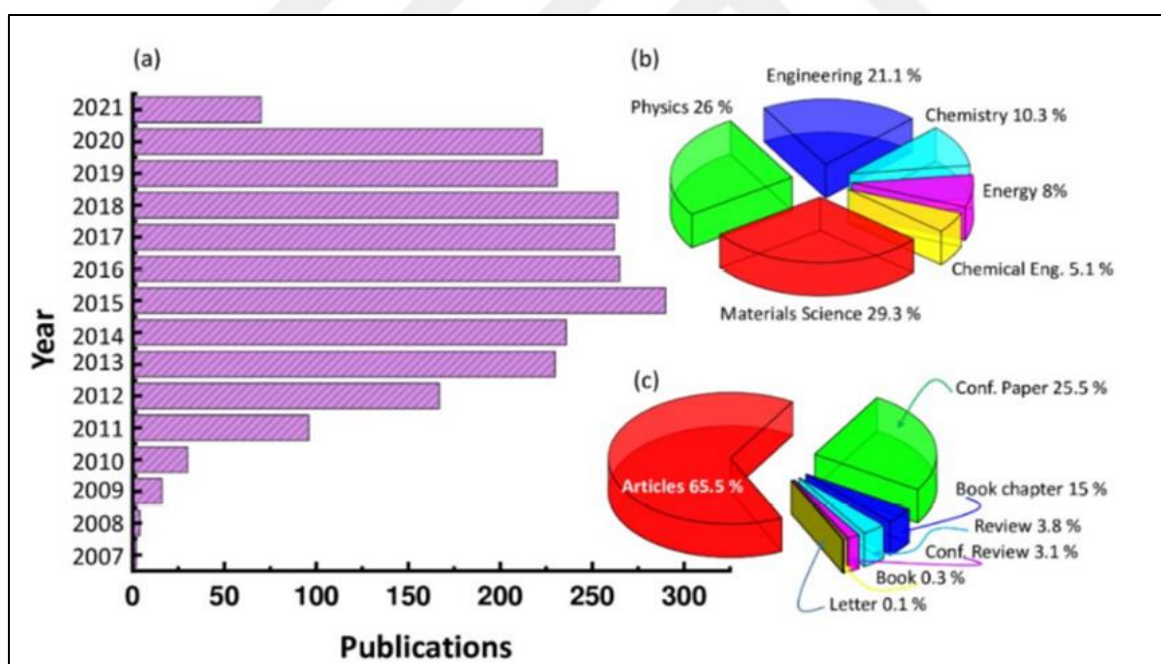


Figure 1.4. (a) Recent publications in the field of "plasmonic plus solar cell" that is mentioned here, as well as the distribution of these publications, (b) by field and (c) by document type. Data came from Scopus, a database of abstracts and citations that experts carefully put together [33]

Solid-state surface plasmon resonance is used to describe this phenomenon (SPR). Surface plasmons are caused by the collective oscillations of surface conduction electrons.

They are induced when electromagnetic radiation interacts with metal nanoparticles that have a negative real dielectric constant and a small positive imaginary dielectric constant. Some examples of these nanoparticles include silver and gold. Excitation of surface plasmons augments the electromagnetic field at specific locations on nanoparticles that are illuminated. The brilliant colors of silver and gold colloids are produced by the light-induced activation of surface plasmons in the nanoparticles of both metals [34,35]. For many of their applications, the optical properties of nanoparticles made from IB metals are fundamental. While a nugget of gold is yellow and an ingot of silver is grey, the colors of Au nanoparticles and Ag nanoparticles highly depend on the size and shape of nanoparticles and range from red to purple [36].

The generated plasmon polariton, stronger than the incident light, appears as an evanescent wave that rapidly degrades as it goes away from the contact in a vertical direction. The metal nanoparticles' surface stores light energy through the SPR phenomenon, providing optical control at a distance below the optical diffraction limit [37-39]. Because of their optical that have unique characteristics, for example, their ability to confine and control light, SPRs have attracted wide interest in different fields, like optoelectronics and biological and sensing applications. There are two types of surface plasmon resonance (SPR): propagating surface plasmon resonance (PSPR) and bound surface plasmon resonance. (LSPR) [40-42].

1.3.1. The propagating of surface plasmon resonance (PSPR)

A propagating surface plasmon resonance (PSPR) is seen at the interface between the plating metal (100 nm to 1 m) and the dielectric [43]. PSPR happens when electromagnetic waves and oscillations in the metal electron plasma mix. (Figure 1.5) demonstrates that the (PSPR) moves in the direction -x and the direction- y along the metal dielectric interface and fades very slowly along the direction of z [44].

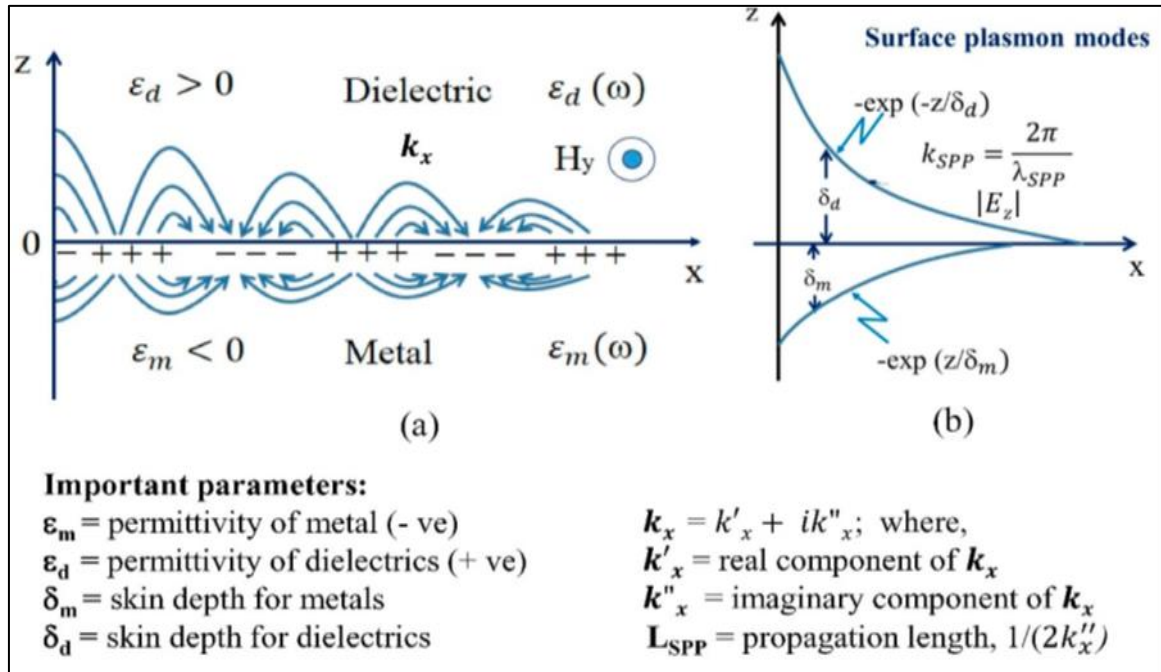


Figure 1.5. SPR waves (a) SPR waves moving along the boundary between the dielectric material and metal, and (b) field size across the boundary and perpendicular to the direction of propagation. The magneto-optic SPR effect demonstrates the directed magnetic field parallel to the metal-dielectric interface along the y-axis [44]

1.3.2. The localized surface plasmon resonance (LSPR)

Metal nanoparticles (5–20 nm) that are less than incident light wavelength show localized surface plasmon resonance (LSPR). The LSPR manifests as (Figure 1.6) when the oscillation frequency of free electrons in metal NPs closely resembles the frequency of the electric field of incident light [33]. Unlike PSPR, LSPR is a non-propagating oscillation of free electrons connected to an electromagnetic field. The local electromagnetic fields and free electron oscillations close to metal nanoparticles are amplified dramatically by the LSPR. The strong secondary electromagnetic field of metal nanoparticles can produce more electron-hole pairs in surrounding organic or inorganic semiconductors [45]. LSPR depends on the metal nanoparticle's local dielectric environment, shape, and size [46].

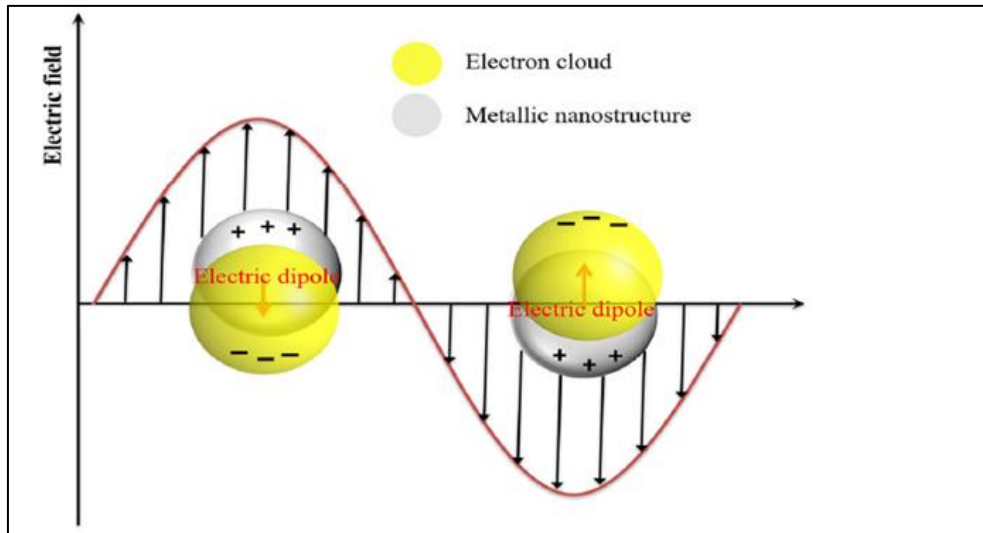


Figure 1.6. A graphical view of localized surface plasmon resonance for a plasmonic nanosphere [47]

1.3.3. Plasmonic effect in photovoltaic cell

Their short physical length severely hampers thin films' inefficient capacity to absorb light. As a result, it gets a less free carrier. Plasmonic nanoparticles (NPs) can increase the light absorption of solar cells with thin film in three primary configurations [48].

First, plasmonic metal nanoparticles with a diameter of more than 50 nm can be used as light-scattering material. Therefore, the light that strikes the material is linked or trapped in the thin absorbing semiconductor layer as a result of the scattering effects. (see Fig 1.7a).

In this case, the light absorption increases when the optical path length within the solar cell's photoactive layer gets longer.

Second, metal nanoparticles between 5 and 20 nm can be used as antennas to make areas with strong electric fields caused by LSPR excitations (Fig 1.7b).

In this configuration, the nanostructures are located close to the photoactive layer so that the layer can absorb more light. Thirdly, periodic nanoarrays of plasmonic metallic nanostructures are placed on the surface's back to connect incident light to an SPP mode in the semiconductor. The light then travels along the plane of the semiconducting layer until it is entirely absorbed by the active medium (see Fig 1.7c) [49].

Light absorption across a broad range of angles and polarizations can be enhanced by arranging plasmonic metallic nanostructures in these three ways. In this instance, the plasmonic-assisted solar cell could significantly affect the efficiency with which it absorbs light and, by extension, converts light into electricity [50].

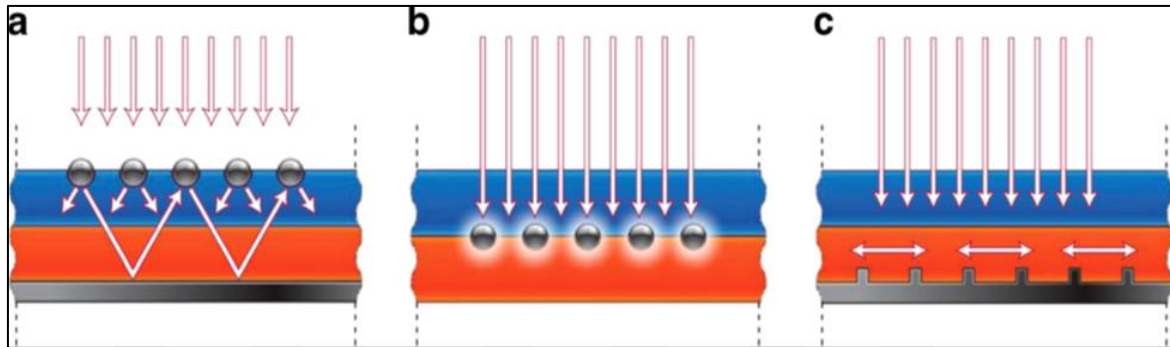


Figure 1.7. Shows thin-film solar cells with plasmonic shapes that trap light. a) Metal nanoparticles trap light on the solar cell's surface. Multiple and high-angle scattering preferentially scatters and traps light in the thin semiconductor film, making the cell's real optical path length is longer. b) capturing light in a semiconductor utilizing metal nanoparticles excited locally by surface plasmons. In the case of semiconductors, electron-hole pairs are made when excited particles are close to each other. c) Exciting surface plasmon polaritons at the metal-semiconductor contact trap light. Light-to-surface Moving plasmon polaritons or photonic modes in the semiconductor layer's plane are linked by the rear surface's corrugations in the metal [49].

1.3.4. Noble Metal Nanoparticles

Since the earliest Egyptian civilization, noble metals have been valued as a sign of superior power and wealth. As a result, they have been found throughout history in the form of valuable artworks, coins, and jewels, among other things [51]. Given how widespread they are in the crust of the Earth, these metals are typically more costly than others [52-53]. Localized surface plasmon resonance (LSPR) is an important property of metal NPs, particularly Au nanoparticles and Ag nanoparticles. When photons with specific frequencies hit the surface of metal NPs, free electrons around the surface start to oscillate as a group—leading to stronger electromagnetic fields and more precise light manipulation [54-57].

LSPR properties can be tuned for particular applications by adjusting the size, shape, composition, and dielectric environment of NPs [58-61].

The plasmonic resonant peaks of Au Nanospheres (NSs) undergo a gradual from 521 to 806 nm in the red, displaying a striking color appearance from red to purple, then to yellow, as the NSs' size increases from 24 to 221 nm. As the Au NS grows, the amount of heat it radiates rises, and the resulting spectrum becomes broader [62].

Exceptional sunlight harvesting and solar energy conversion capabilities are present in plasmonic metal nanostructures because of their remarkable optical properties. It is common knowledge that the sea-level solar spectrum illuminates an extensive spectrum of wavelengths from 200 nm to 2.5 μ m. Ultraviolet light makes up about 3% of solar energy, visible light 43%, and infrared light 54%, respectively [63].

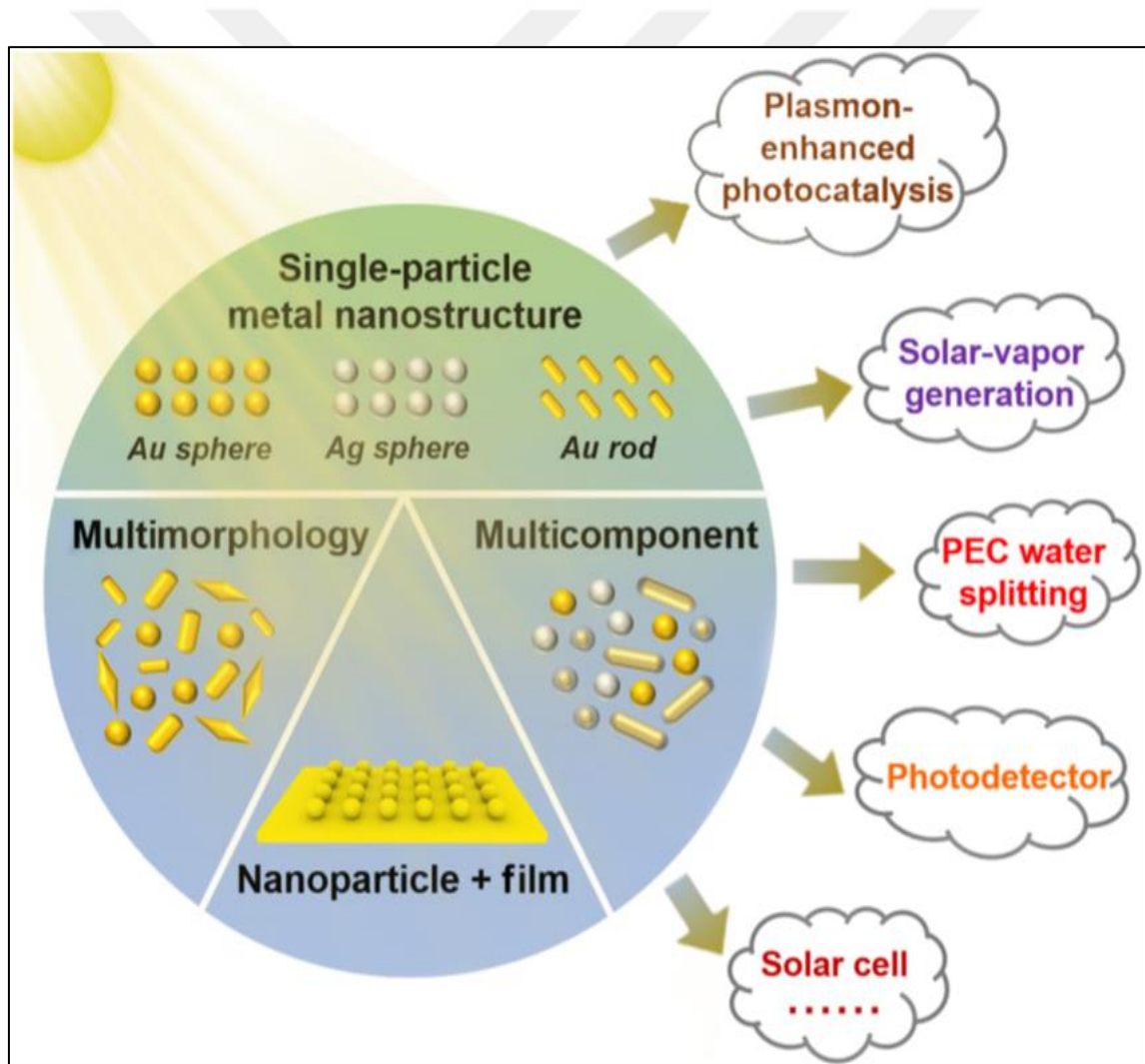


Figure 1.8. Describe Plasmonic nanostructures for solar energy conversion [63].

The rapid progress in synthesis and characterization techniques has led to the development a massive range of metallic NPs and nanostructures. Plasmonic resonances should extend from the ultraviolet to the near-infrared, allowing them to absorb as much sunlight as possible. However, individual metal nanoparticles usually only react to a narrow range of wavelengths, severely restricting their ability to harness solar energy. Therefore, multiplex (composition, size, shape, or array) NP structures are anticipated to enable integrated (i.e., optical, electrical, and magnetic) features, which may play key roles in maximizing photon absorption and total solar energy [64-66].

Table 1.1. Summarizes some properties of gold and silver metals.

<i>General properties</i>		
Name	Gold	Silver
Symbol	Au	Ag
Appearance	Metallic yellow	Lustrous white metal
<i>Gold and Silver in the periodic table</i>		
Atomic number	79	47
Standart atomic eight	196,966569(5)	107,8682(2)
Element category	Transition metal	Transition metal
Group	Group 11	Group 11
Block	d-block	d-block
Peiod	Period 6	Period 5
Electron configuration	[Xe]4f ¹⁴ 5d ¹⁰ 6s ¹	[Kr] 4d ¹⁰ 5s ¹
Per Shell	2, 8, 18, 32, 18, 1	2, 8, 18, 18, 1
<i>Physical properties</i>		
Pahse	Solid	Solid
Melting point	1064.18 °C	961.78 °C
Boiling point	2970 °C	2162 °C
Density near R.T. when liquid, at M.P.	19.30 g cm ⁻³ 17.31 g cm ⁻³	10.49 g cm ⁻³ 9.320 g cm ⁻³
Heat of fusion	12.55 kJ mol ⁻¹	11.28 kJ mol ⁻¹
Heat of vaporization	342 kJ mol ⁻¹	254 kJ mol ⁻¹
Molar heat capacity	25.418 J mol ⁻¹ K ⁻¹	25.350 J mol ⁻¹ K ⁻¹
<i>Miscellanea</i>		
Crystal structure	Face-centered cubic (fcc)	Face-centered cubic (fcc)
Speed of sound thin rod	2030 m s ⁻¹ (at r.t)	2680 m s ⁻¹ (at r.t.)
Thermal expansion	14.2 μm m ⁻¹ K ⁻¹ (at 25 °C)	18.9 μm m ⁻¹ K ⁻¹ (At 25°C)
Thermal conductivity	318 W m ⁻¹ K ⁻¹	429 W m ⁻¹ K ⁻¹
Electrical resistivity	22.14 nΩ m (at 20 °C)	15.87 nΩ m (at 20 °C)
Magnetic ordering	diamagnetic	diamagnetic

1.4. Aims of the work

- 1- Preparation of Au @SiO₂ and Ag@SiO₂ nanoparticles core-shell using laser ablation technique in liquid with different laser flounce values.
- 2- Study the structural and optical properties, morphology, and nanoparticles for Au@SiO₂ and Ag@SiO₂.
- 3- We use the most effective outcome from fabricating a DSSC based on noble metal @ silica core-shell nanoparticles.



2. LITERATURE REVIEW

Recent studies show that surface plasmon resonance makes noble metal NPs absorb more light. Park and his colleagues made DSSCs with 100nm Au NPs inside TiO₂ NPs. By incorporating plasmonic metal nanoparticles, device efficiency and photocurrent are both improved. Due to their excellent SPR optical properties, Au NPs and Ag NPs are used to starting plasmonic enhancement in solar cells. Several groups have tried to improve DSSCs with the help of NPS [67].

Compared to a film made of simply TiO₂ NPs, this show absorbs significantly more light, and light travels longer distances due to scattering. In contrast, low charge separation and carrier loss at the electrodes occur when Nanoparticles of metal are exposed to the dye molecules or the electrolytes due to issues like corrosion, recombination, and the back reaction of the charge carriers. One strategy for resolving such problems is coating the nanoparticles of metal containing metallic oxide coatings, like SiO₂ or TiO₂. It does not just prevent corrosion of metal nanoparticles with I⁻ / I₃⁻, but also electrolyte enhances dye absorption. Reducing To maximize the LSPR effect on dye molecules' ability to absorb light, photoanodes should be as thick as possible, and the effectiveness of dye-sensitive solar cells for converting energy with a photoactive layer but not be thick. Jifa Qi et al. made DSSCs using an Ag@TiO₂ core shell [68].

Michael D. Brown explores the use of Au-SiO₂ nanoparticles in DSSCs. Show that I-/I₃ solar cells that use an electrolyte and those that use a solid state (dye-sensitized) benefit from augmentation of an increase in absorption due to plasmons of light, photocurrent, and performance. Spectroscopic research shows that after light absorption within the first few tens of femtoseconds, enhanced photocarrier generation by plasmons is competitive with the oscillation damping of plasmons [69].

Prashant V. Kamat et al. shell material impacts DSSCs performance; they created Au@SiO₂ nanoparticles and Au@TiO₂ nanoparticles. For the DSSCs containing Au@TiO₂ nanoparticles, The Au core was charged with electrons. This increased voltage open-circuit (V_{oc}) due to charging influence. However, for the DSSCs that use Au@SiO₂ nanoparticles, SiO₂ hinders core metal charging with electrons, resulting in larger J_{sc} due to surface

plasmonic effect dampening within the initial tens of femtoseconds after light absorption [70].

Nanocubes of Au@SiO₂ were integrated into the photoanodes of DSSCs by Holly Zarick et al. to enhance light harvesting. As a result of their strong light scattering and absorption region, simulations of finite domain difference time revealed that the disappearance of all light for Au@SiO₂ nano cubes between the 700 nm to 900 nm range is exceptionally high. Photocurrent characteristics and spectra from the IPCE indicate that the device's performance can be controlled by controlling the concentration of Au@SiO₂ nano cubes. Consequently, the J_{sc} was significantly raised with a 1.8 weight-percent increase in Au@SiO₂ nano cubes, contributing 34% improvement in DSSCs working and an increase in PCE from 5.8% to 7.8%. The strong electromagnetic field in the edges and corners of the nano cubes improves carrier generation and DSSCs performance by increasing the molecular coupling of plasmonic, leading to the best performance of plasmon-enhanced DSSC [71].

To improve the performance of N719-based DSSC, Elbohy et al. added Au Nano stars to the dye-sensitized mixture and observed absorption at the near-infrared read wavelength of 785 nm. PCE of DSSC with Au nanostars rose 20% to 8.2%. DSSCs that used N749 dye had a maximum absorption light (410 nm, 610 nm) than N719, and PCE increased by 30%, from 3.9% to 5.0%. Strong and broad LSPRs between 500 and 1,000 nm improve PCE [72].

By altering the sizes for sides of the nanorods' (NRs), there are 2 LSPR bands with significantly different spectral characteristics were produced.

created DSSCs with a composite Au NR@SiO₂ photoanode. The usage of Au NR@SiO₂ increased the efficiency of DSSCs by 23%. They saw that the max, at 514 nm, and 656 nm, went from 5.86% to 7.21%. As a result of the dye's spectral response being amplified thanks to the longitudinal plasmon absorption of Au Nanorods, DSSC efficiency was significantly improved [73].

For their experiments, Guo et al. also employed DSSCs with varying Ag concentrations in an AgNW@SiO₂ core shell. An increase in J_{sc} from 9.69 mA cm⁻² to 11.83 mA cm⁻² led to a rise from 5.45% to 6.26% in DSSC PCE.

Because of light coupling increased at 350 nm and 388 nm by the LSPR of AgNanowire@SiO₂ in the photoanode, the dye molecules' light absorption and photon capture capabilities were greatly improved by integrating Ag NW@SiO₂. Moreover, This led to improved J_{sc} and PCE [74].

Timothy L. Kelly et al. found that nontriangular prisms and nanoplates were investigated for use in DSSCs. Anisotropic Ag NPs, such as Ag nano prisms and nanoplates, exhibit a redshifted extinction in contrast to Ag NPs in the form of spheres with LSPR absorbance at 400 nm.

By varying the aspect ratio, it is possible to modify LSPR's location from the blue-violet to the NIR range. Due to an improvement in light-harvesting efficiency for between 550 to 750 nm, or the red and near-infrared spectrums, the photoanode of DSSCs could be significantly enhanced by using 0.05 weight percent triangular Ag@SiO₂ nano prisms, increasing the PCE by 32% [75].

Hyun-Young Kim et al. Rapid thermal processing created Ag nanoplates with maximal extinction wavelengths of 470, 540, and 620 nm. Three Ag nanoplates were immobilized onto a polymer-coated film (4-vinyl pyridine) to form the panchromatic quasi-monolayer Ag NPs (P4VP). Ag nanoplates with high extinction coefficients at 470, 540, and 620 nm may be prepared quickly by heating. Three Ag nanoplates were immobilized on a poly(4-vinyl pyridine)-coated screen to create the panchromatic quasi-monolayer of Ag NPs (P4VP) [76].

Al-Azawi, Mohammed A., et al. Utilizing them to produce gold-silver nanoparticles required two stages of preparation (Au–Ag alloy NPs). Following the pulsed laser ablation of pure metallic targets in ethanol, mixing, and re-irradiation to create the colloids, average particle sizes of 14.80 and 8.47 nm were obtained for Au and Ag, respectively (volume ratio 4:1). In this investigation, titanium dioxide (TiO₂) was applied to the conducting side of fluorine tin oxide (FTO) glass at a thickness of 11 μm. A porous TiO₂ layer was employed as the photoanode to create dye-sensitized solar cells using N719 dye molecules, both with and without plasmonic-metal nanoparticles (NPs) (DSSCs) [77].

Qi Xu et al. demonstrate studies of using nanoparticles (NPs) of gold-silver alloy in the shape of popcorns to enhance the dye sensitized solar cells' broad-band optical absorption (DSCs). Absorption improved over a wide wavelength range is shown in popcorn-shaped alloy NPs, as shown by simulations and experimental data, because the localized surface plasmons' (LSPs) excitation at various wavelengths, compared to regular plasmonic NPs like nano-spheres. They found that When Popcorn is made with an alloy of gold and silver, 2.38 weight percent NPs are added to DSCs, and the PCE increases from 5.26% to 6.09%. With the addition of layers of scattering on the counter electrode outside, popcorn NPs show a 32% improvement in PCE, owing to the NPs' improved LSP mode excitation, from 5.94% to 7.85% [78].

The researchers Juyoung Yun et al. discovered that increasing the PCE of dye sensitized solar cells may be achieved by enhancing the photoanode's light-harvesting capabilities (DSSCs). Using a chemical deposition and sol-gel process, Au@Ag/TiO₂ HNPs were created.

Au@Ag/TiO₂ HNPs are a combination of Au@Ag NPs and TiO₂ hollow nanoparticles (TiO₂ HNPs). Enhanced light-harvesting was achieved thanks to the Au@Ag CSNPs'; TiO₂ HNPs have a specific surface area that is high (129 m²/g), can scatter light, and are easily oxidized and reduced by electrolytes. In DSSCs, photoanode materials based on TiO₂ HNPs comprising Au@Ag/TiO₂ HNPs (0.2 wt% Au@Ag CSNPs with TiO₂ HNPs) achieved a PCE of $\eta = 9.7\%$, 24% higher than the PCE of typical P25 photoanodes ($\eta = 7.8\%$) [79].

Hua Dong et al. have found increasing the effectiveness of dye sensitized solar cells with the help of Au@Ag NRs (DSSCs). This new plasmonic nanostructure increases light harvesting in DSSCs while lowering charge recombination. Au@Ag NRs' surface plasmon resonance (SPR) effect allows for greater light absorption at the photoanode. Their enhanced ability to absorb red and NIR wavelengths ensures that all of the sun's energy is harnessed. Au@Ag NRs improve charge separation and recombination, further enhancing DSSC light-driven chemical processes. The PCE of the optimized Au@Ag NR modified DSSC is 8.43%, much higher than the pure TiO₂ DSSC (5.91%) [80].

In 2015, Yang Wang et al. discovered that by tailoring the Ag shell thickness, or the light-scattering photoresponse (LSPR) effect, core-ultra thin shell nanoparticles (Au@Ag@SiO₂)

could be manufactured and injected into DSSC to enhance light harvesting and decrease photo carrier recombination. The photoconversion efficiency of an Au@Ag@SiO₂ electrode at 486.72 nm and ten mW/cm² is 23.42% [81].

Sungmo Ahn et al. compiled and assessed the most up-to-date findings on plasmonic nanostructures for OPV and approaches for improving them in 2016. Metal nanoparticles, patterned electrodes, and plasmonic metamaterials all exhibit enhanced optical absorption due to resonant scattering and the strong plasmonic near field. The electrical effects of plasmonic nanostructures, which impact device efficiency, are also investigated. Also, they talk about what comes next in the field of study [82].

Rizky Nanda Puspitasari, in 2017 This research used gold nanoparticles with a core-shell configuration that incorporated SiO₂ isolated from Vulcan's Lapindo mud. This Study employs nanoparticle core-shell structures composed in the form of SiO₂@TiO₂@Au and TiO₂@SiO₂@Au.

It has been found that the direct contact between Au and TiO₂ in the DSSC with TiO₂/SiO₂/TiO₂@TiO₂@Au nanoparticles as photoanodes results in a power conversion efficiency of almost 1.9 times greater than that of the DSSC with only TiO₂ as photoanodes [83].

Bao Wang et al. (2018) created Ag@SiO₂ nanoparticles using Stöber modified technique. Prepare a mesoporous layer of TiO₂ without a hole-carrying layer for perovskite solar cells with a carbon counter electrode (PSCs). Using UV-vis spectroscopy, the maximum absorption peak of Ag NPs was determined to be in the vicinity of 400 nm; The XRD patterns of the produced Ag NPs confirmed their nanocrystal and face-centered cubic structures. As seen in transmission electron microscopy photos, the nucleation size distribution of Ag NPs was centered at 26 nanometers, and their average thickness shell for silica was 14 nanometers. Overshooting the optimal Ag@SiO₂ concentration in the mesoporous layer has no effect on the short-circuit current density or incident photon-to-electron conversion efficiency, as the insulating silica shells inside the TiO₂ network prevent electron transit [84].

Abdollah Neshat and Rasoul Safdari 2019 chemically nanoparticles of gold-silicate (Au@SiO₂) surface plasmon resonance was artificially produced. Au@SiO₂ NPs were

studied to see how that affected the solar cells with dye sensitization's photocurrent density. UV-vis spectroscopy measured the absorption of Au@SiO₂ NPs, and the maximum peak was near 521 nm; FE-SEM images revealed NPs with diameters between 20 and 60 nm. DSSCs performed better when the photo-anode surface was adorned with Au@SiO₂ nanoparticles of the proper size and shape. Light intensity was measured at 100 mW/cm² under an AM 1.5 light source. The anode surface's solar energy-to-electricity conversion efficiencies of 1cm² and 2cm² DSSCs with Au@SiO₂ NPs increased by 20% and 10%, respectively [85].

Ling Weng et al. (2020) utilized PVDF to prepare Ag@SiO₂ core-shell nanoparticles (the chemical method). Near 400 nm. The highest absorption peak for NPs formed. Ag@SiO₂ core-shell nanoparticles were biphasic (cubic+ hexagonal) with a size of an average of 100 nm and a thickness of the shell of approximately 20 nm; core-shell Ag@SiO₂ nanoparticles demonstrated a significant increase in electrical breakdown strength. Similarly, the calculated energy density increases from 0.016777 to 0.044234 J/cm³ [86].

I. Perdana and M. Muldarisnur chemically synthesized Ag-SiO₂ core-shell nanoparticles in 2021. As they are inexpensive to manufacture and effective at converting sunlight into energy, organic solar cells hold great promise. Low efficiency is the primary disadvantage of these solar cells.

At a particle distance of 60 nm, the dual periodicity model increases absorption by 98%. Increased absorption inside the layer, which is directly brought on by LSRP events, improves the performance of organic solar cells [87].

Ag@SiO₂ NPs were created in 2022 by Elmira Alikhaidarova et al. using a chemical process. These NPs were then used to study the photovoltaic performance characteristics of polymer solar cells. Ag@SiO₂ NS was added to the PEDOT: PSS film at the optimum concentration of 108 mol/L, improving the efficiency of the solar cell that has polymer by 60% and incorporating Ag@SiO₂ nanostructure into the PEDOT: PSS film-boosted polymer solar cells by decreasing the electrical resistance of the PEDOT: PSS layer and increasing light harvesting via dispersion. The surface plasmon peak at 213 nm confirmed the synthesis of Ag@SiO₂ nanoparticles. IPCE, time-resolved photoluminescence spectroscopy, and EIS studies clarified the solar cell's mechanism and kinetics [88].

3. THEORETICAL BACKGROUND

3.1. The Dye Sensitized Solar Cells (DSSCs)

DSSCs have attracted huge interest as cutting-edge solar technology due to their high efficiency, low production costs, and environmental friendliness [89-93].

3.2. Solar cells Basic principle

Utilizing photovoltaic technology, solar cells transform sunlight into useful energy, like electricity. As seen in (Figure 3.1), the photovoltaic (PV) effect takes place in the p-n junction to transform light into usable energy. Three fundamental processes—absorption, separation, and migration—can be used to illustrate the photovoltaic effect, the underlying concept of solar cells.

1. A photon is absorbed in the semiconductor's p-type phase, resulting in the formation of a conducting pair (electrons and holes).
2. The excess energy that is above the band gap is wasted as the pair immediately undergoes thermalization with the phonons in the lattice.
3. The electron migrates to the left while the hole migrates to the right due to the potential difference that exists across the interface, creating a voltage between the two terminals [94-96].

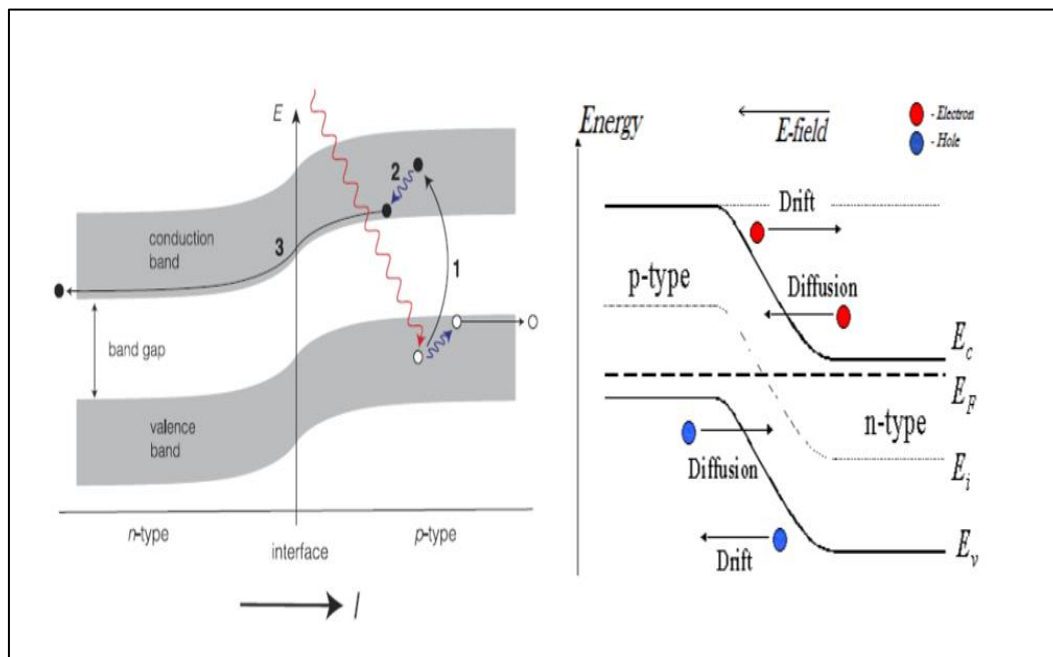


Figure 3.1. An illustration of the photovoltaic effect [95,96].

3.2.1. Performance of photovoltaic solar cells

Typically, the photovoltaic efficiency of solar cells is evaluated in standard test conditions (STC), which involve irradiation of $100\text{mW}/\text{cm}^2$, air with 1.5 of mass (AM), and a cell at 25°C of temperature. (Figure 3.2)depicts the J-V curve that can be obtained by measuring the voltage produced by solar cells when they are biased in the forward direction. Three parameters significantly impact solar cell efficiency: short circuit current (J_{sc}), open-circuit voltage (V_{oc}), and fill factor (FF) [97].

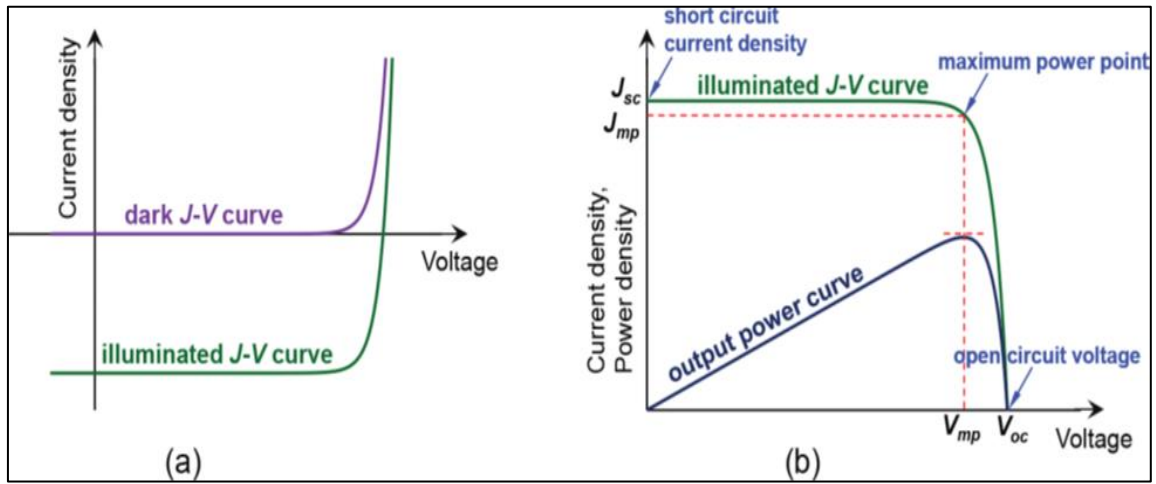


Figure 3.2. Silicon photovoltaic cell (a) in both its dark and illuminated J-V states; (b) An illustration of a J-V curve that is illuminated, together with a voltage-dependent output power density curve that highlights the short-circuit point ($0, J_{sc}$), open-circuit point ($0, V_{oc}$), and maximum power point (P_{max}); (V_{mp}, J_{mp}) [97].

When there is no voltage across the component, a current of J_{sc} will flow through the external circuit. J_{sc} is influenced by the solar cell's area, optical quality, and collection probability, as well as the intensity and spectrum of incident light. When no current flows across an external circuit, that value is known as the voltage open circuit. The value of V_{oc} [98]. It is based on the bandgap of semiconductor materials. The V_{oc} of higher bandgap semiconductor materials is greater, but the J_{sc} is smaller. To calculate the fill factor, FF, we divide the maximum output solar cell power (P_{max}) by its theoretical power output (P_{theo}) using (equation 3.1) [99].

$$P_m = J_{mp} \times V_{mp} \quad , \quad FF = \frac{P_{max}}{P_{in}} = \frac{J_{mp} \times V_{mp}}{J_{sc} \times V_{oc}} \quad , \quad \eta = \frac{P_m}{P_m} \quad (3.1)$$

Like in (Figure 3.3), the FF can also be expressed as the area of a rectangle that lies within a J-V curve [99].

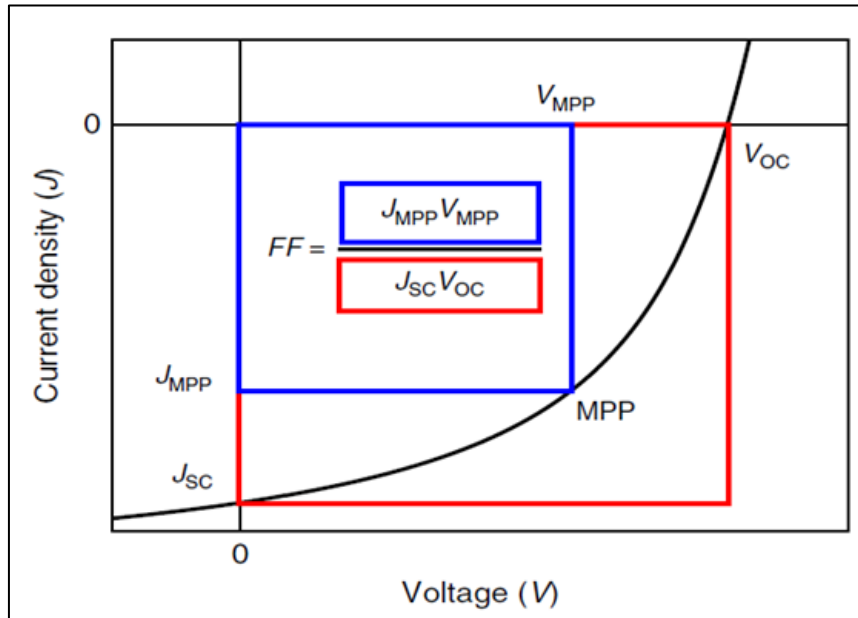


Figure 3.3. The solar cell's J-V characteristic [99].

Both (R_s) resistance series and (R_{sh}) shunt resistance affect the FF. Parameters R_s and R_{sh} affect the efficiency and form of a J-V curve. The R_s are associated with the diffusion and resistance of the electrolyte between the semiconductor and the electrode. There is no change in V_{oc} but a fall in J_{sc} and FF for every unit increase in R_s . At the highest levels of R_s , J_{sc} drops dramatically, leading to resistor behavior, as seen in (Figure 3.4). (a). Due to trapped electron recombination, the shunt resistance (R_{sh}) drops, leading to the formation of a tiny recombination site and consequent current leakage. As the R_{sh} drops, so do the V_{oc} and ff. The resistor's working characteristics are depicted in (Figure 3.4), demonstrating that at the lowest R_{sh} values, V_{oc} drops dramatically (b). Increasing R_s and decreasing R_{sh} reduce FF, reducing P_{max} [99-101].

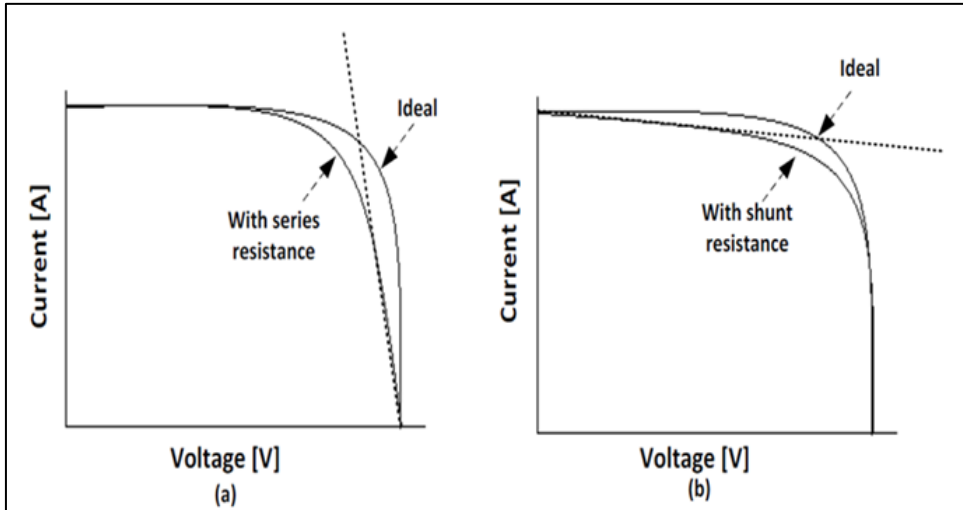


Figure 3.4. The effect of (a) resistance series (R_s) and (b) resistance shunt (R_{sh}) on the shape curve for I-V [101].

3.2.2. Solar cells and their efficiency

Power conversion efficiency is commonly used to measure solar cell performance (PCE). The PCE can be determined with (Eq.32) . Power output (P_{out}) is equal to the product of the power going into the cell (P_{in}) and its voltage (V_{oc}) and current (FF) (P_{in}). The best solar cell performance can be achieved by adjusting these three variables. V_{oc} rises as J_{sc} and FF fall [102-104].

$$PCE = \frac{P_{out}}{P_{in}} = FF \times \frac{V_{oc} \times J_{sc}}{P_{in}} \quad (3.2)$$

Quantum efficiency (QE) measures how efficiently solar cells convert incoming light into usable power. In quantum mechanics, there are two varieties. EQE and IQE refer to external and internal quantum efficiencies, respectively. EQE is a metric for gauging how well a device performs in short-circuit situations at converting incident photons into electric current. (Eq 3.3) . The IQE measures the efficiency with which photons are converted into electric current in a short circuit. (Eq 3.4) [102,104].

$$EQE = \frac{\frac{\text{electrons}}{\text{sec}}}{\frac{\text{photons}}{\text{sec}}} \quad (3.3)$$

$$IQE = \frac{\frac{\text{electrons}}{\text{sec}}}{\frac{\text{photons}}{\text{sec}}} \quad (3.4)$$

Quantum efficiency (QE) is calculated by comparing the efficiency of the current to that of a single photon that has been incident (IPCE). Their IPCE, or incident photon, measures solar cells' efficiency to excited charge carrier ratio. In order to determine this, we divide the photon flux at the excitation wavelength by the photocurrent density in the external circuit when the light source is on, yielding Eq (3.5) [105].

$$IPCE = \frac{1240 (eV.nm) \times J \left(\frac{\mu A}{cm^2} \right)}{\lambda(nm) \times P(\mu W \times cm^2)} \times 100\% \quad (3.5)$$

3.3. Design and construction of a DSSCs

A DSSC consists of the photoanode (WE), the counter electrode (CE), the sensitizer (dye), and the redox mediator (electrolyte; solid hole transporting substance may be substituted for electrolyte) [106,107].

3.3.1. Transparent and conductive substrate of DSSCs

Both layers of a DSSC are normally transparent and conducting. The semiconductor and catalyst are placed onto these sheets, which also act as current collectors. These DSSCs are solar energy generators, functioning as photovoltaic cells. You can see the basic layout of DSSCs and their parts in the diagram depicted in (Figure 3.5) [108].

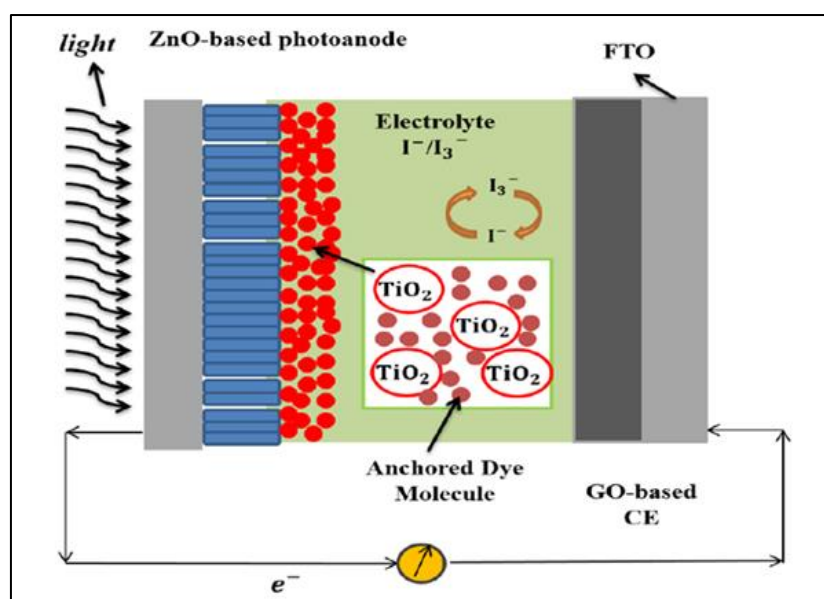


Figure 3.5. Structure and components of DSSCs [108].

3.3.2. Transparent and conductive substrate

Two transparent, conductive sheets are used to construct DSSCs; these sheets serve as current collectors and a substrate over which the semiconductor and catalyst are deposited [109]. A DSSC requires a highly transparent substrate that lets at least 80% of the light from the sun through. DSSC functionality depends on this being set up correctly. In addition, the substrate must provide highly electrically conductive optimal transmission of charge, and losses were low in energy. Fluorine-doped tin oxide (FTO, $\text{SnO}_2\text{:F}$) and indium-doped tin oxide ($\text{SnO}_2\text{:I}$) are the most widely employed substrates (ITO, $\text{In}_2\text{O}_3\text{:Sn}$). As mentioned above, these substrates have the chemicals sprayed onto glass (usually soda-lime glass). FTO films have a visual transmittance of around 75%, while ITO films are well over 80% transparent. As a comparison, the sheet resistance of ITO films is $18\Omega/\text{cm}^2$, while that of FTO is just $8.5/\text{cm}^2$ [110,111].

3.3.3. Working electrode

TiO_2 , ZnO, SnO_2 (n-type), Nb_2O_5 , and NiO are just some of the semiconductor oxides that can be used to prepare the substrates for the working electrode (WE) (p-type) [112]. These oxides exhibit a substantial energy band gap. TiO_2 is the most popular oxide because it is affordable, commonly available, and non-toxic. Even though these semiconductors absorb only a small amount of light, they are coated or immersed in a sensitizer to improve their performance. This pigment is adsorbed onto the TiO_2 surface, forming covalent bonds.

Due to the roughness of the WE layer and the structure's high porosity, many dye molecules bind to the nanocrystalline surface of TiO_2 , thereby significantly enhancing light absorption [113].

3.3.4. The sensitizer of dye

Dyes used in DSSCs act as solar absorbers, and the sensitizers' qualities significantly impact the efficiency with which light is harvested and electricity is converted.

For dye-sensitized solar cells, ideally, a sensitizer would have a strong graft to the oxide surface of the semiconductor, absorb all light below 920 nm, and deliver electrons with a

quantum unity yield into the conduction band [114]. It must have a high enough redox potential to rapidly recharge by absorbing donated electrons from a hole conductor or an electrolyte. It must also be strong enough to withstand at least 10⁸ redox reactions while lighted and about 20 years of exposure to natural light [115]. The goal of the dye is to absorb light and send electrons to the conduction band of a semiconductor. By forming chemical bonds, it sticks to the textured semiconductor surface. Each of these is essential in a photosensitizer [116]:

1. Show excellent visible-light absorption (400 nm to 800nm)
2. Having a high attenuation coefficient and significant adsorption on the surface of the semiconductor
4. It is unaffected by its oxidation state and can lower its oxidation level with an electrolyte
5. Possess the stability necessary to carry out 10⁸ rotations, or twenty years of working
6. Have a greater HOMO than the redox potential of the electrolyte and a higher LUMO than the semiconductor's CB.

Metal-free organic sensitizers, natural sensitizers, and metal complex sensitizers are the three types of photosensitizers [117].

3.3.5. The electrolyte

The electrolyte replaces the dye after introducing electrons into the semiconductor's conduction band. Additionally, it conducts positive charges toward the (CE) counter electrodes. The characteristics of the electrolyte are substantially impacted the stability of DSSCs over their lengthy functioning lifetimes. Therefore, the electrolyte must possess the following property [111,112,116-118]:

- 1- Highly efficient electron diffusion is facilitated by the material's low viscosity and excellent electrical conductivity.
- 2- The nanocrystalline semiconductor has excellent interfacial contact with the CE.
- 3- The dye on the oxidized surface shouldn't deteriorate or desorb at all.
- 4- Light in the visible spectrum must pass through unimpeded.

The electrolytes used in DSSCs can be classified as either solid, liquid, or quasi-solid [119].

Liquid Electrolytes: Depending on the type of solvent employed, liquid electrolytes can be divided into two categories: RTIL (Electrolytes that exist in ionic liquids at ambient temperature) and organic based solvent electrolytes [120].

Organic Electrolytes: The performance of DSSCs is affected by organic electrolyte components, including the solvent, additives, and redox couple. An organic electrolyte's key component is the redox pair. Numerous redox couples, including Br^-/Br^3 , $\text{SCN}/(\text{SCN})_2$, and $\text{SeCN}^-/(\text{SeCN})$ [121], in addition to substituted bipyridyl cobalt (III/II), have been studied. Due to its excellent solubility, rapid dye regeneration, minimal absorption of visible light, adequate redox potential, and incredibly slow recombination kinetics between injected electrons into the semiconductor and triiodide, I_3^-/I^- is a good redox pair [122].

The Ionic Electrolytes: Liquid electrolytes have a high volatility that can lead to a high evaporation rate, although RTIL has successfully been utilized to lower this rate. These organic salts have halide or pseudohalide anions and titles like "pyridinium" or "imidazolium." They are helpful since they can dilute other substances and because they contain iodine [123].

Solid-State Electrolyte: Leakage is a major problem for DSSCs that rely on liquid electrolytes, significantly lowering their durability over time. In order to boost efficiency and dependability, solid-state electrolytes have been created. Rather than a traditional liquid electrolyte, they employ a p-type semiconductor [112].

3.3.6. Counter electrode(CE)

To replenish electrolytes, a counter electrode is utilized. The oxidized electrolyte makes its way to the counter electrode, which is in contact with the external circuit and receives electrons from it. For speed in the reduction reaction, a catalyst is necessary; the high exchange current density of platinum (Pt) makes it a top choice due to 1)excellent catalytic activity and 2) transparency. The CE's effectiveness depends on how well the Pt is deposited on the TCO base [117,119].

3.4. DSSC's Working Principles

As stated previously, DSSC solar cells operate differently than conventional semiconductor solar cells in terms of their essential operating principles. Both absorptions of light and transfer of charge carriers are intertwined processes in semiconductor solar cells [124]. The light must be absorbed, electrons must be injected, carriers must be transported, and finally, collected in order for a dye-sensitized solar cell to work. DSSCs devices generate electricity from incident solar radiation without undergoing any irreversible chemical reaction [3]. Electron and hole charge movement through DSSCs' not-well-defined interfaces is complex. (Figure 3.6) shows kinetic cell mechanisms [125].

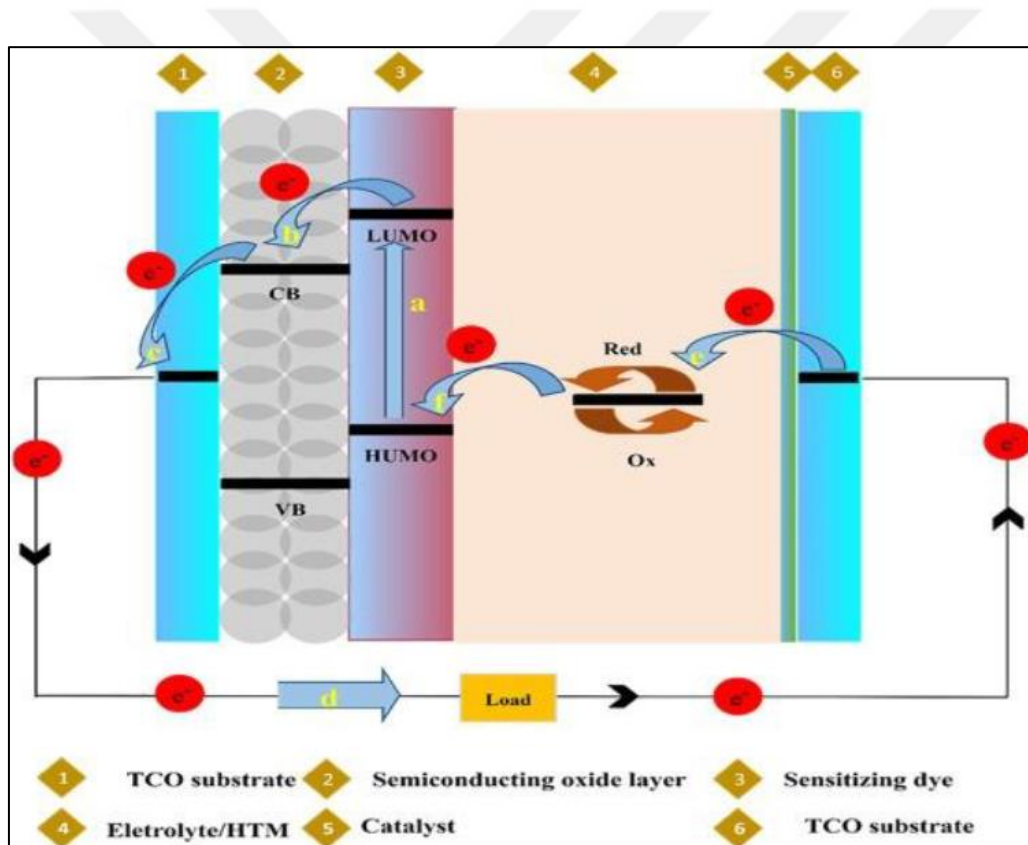
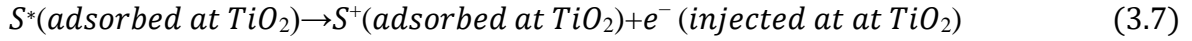


Figure 3.6. A diagram demonstrates how a DSSC operates. Each of the following occurrences takes place: a) photoexcitation, b) injection, c) transport, d) conduction, e) diffusion, and f) regeneration [125].

Interfacial electron transport activities are essential to its functionality. A photon ($h\nu$) is absorbed by the sensitizer or dye (S) and transferred to the semiconductor, anchoring it in its excited state (S^*) when light hits the photoelectrode (Equation 3.6):



Dye's S^* state discharges or injects an electron into TiO_2 's conduction band (CB), creating the oxidative species S^+ (equation 3.7):



The porous semiconductor network of TiO_2 nanoparticles then transfers the electrons to the TCO layer. Electrons in the TCO layer are routed to the counter electrode through an external connection (CE). This transferred electron then diffuses into the electrolyte, which catalyzes the reduction of I_3^- to the I^- (Eq3.8). The renewal of the dye takes place once I^- is created, as illustrated in (Eq 3.9). We have reached the final stage of the cycle.



Recombination is a procedure that happens throughout this process that is inefficient and should be avoided. Electrons injected into TiO_2 's CB can either go to the oxidized dye (equation 3.10) or I_3^- ions very close to the surface.

As it relates to semiconductors (equation 3.11) [126].



Although the exact method by which the dye cation is reduced is still up for question (Eq 3.9) appears to take place through a chain of events [125].



The extent in (Equation 3.12) is fast, and (Equation 3.13) is restrictive. The mechanism is entirely speculative from here on out, but many potential routes have been presented. (Eq

3.13) states that the interaction of her second iodide ion (I^-) with the $[I : S^+]$ complex is necessary for the regeneration reaction. A thiocyanate (SCN) ligand in the dye is necessary for this reaction to occur. The nature of the intermediate complex is a mystery if this ligand is absent. Upon reacting with the second iodide, the diiodide I_2^- detaches from the dye molecule. Iodides and triodes can be synthesized from this diiodide radical (equation 3.14) [126].



The driving force is provided by the dissimilarity between the redox potentials of pair in the electrolyte and the level of quasi-Fermi. Injection (Equation 3.6) and regeneration (Equation 3.9) processes (ahead reactions) must have a higher kinetic favorability than recombination processes (backward reactions) for optimal efficiency (reverse reactions). In (Figure 3.7), timelines and processes are presented. Photoelectron recombination is a slower process than dye renewal, which makes DSSC practical.

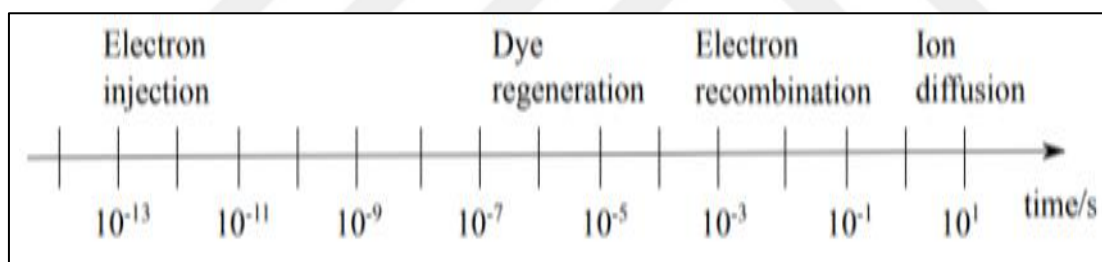


Figure 3.7. Timescales of various processes in DSSC [126]

The absorption of light by sensitizers is another crucial phase in the DSSC functioning mechanism. As a result of the dye's absorption of sunlight, electrons are excited from the level of (HOMO), the highest occupied molecular orbital going to (LOMO), the level of the lowest unoccupied molecular orbital. The relative position between these dye orbitals and the semiconductor energy bands, which facilitates electron transport, is an essential factor [124].

The device's overall performance can be assessed using the fill factor (FF) and cell efficiency (η). As illustrated in (eq 3.15) and (eq 3.16) [109].

$$FF = \frac{V_{max} \times J_{max}}{V_{oc} \times J_{sc}} \quad (3.15)$$

$$\eta = \frac{V_{oc} \times J_{sc} \times FF}{P_{in}} \times 100\% \quad (3.16)$$

The maximum current and voltage readings on the curve of J-V occur when the power output is at its highest. J_{sc} , V_{oc} , and incident light power indicate the short-circuit current density (mA/cm^2) in electrical systems (P_{in}) [127].

The electron Fermi level in the TiO_2 layer and electrolyte redox potential is responsible for the photovoltage (V_{oc}).

Equally important to photocurrent is incident light harvest efficiency (LHE), electron injection efficiency, and collecting efficiency (J_{sc}). Normal conditions of lighting (AM 1.5, $100 \text{ mW}/\text{cm}^2$) are used for DSSC tests. Parameters like V_{oc} , J_{sc} , and FF can be optimized in typical conditions to boost device performance [128].

3.4.1. Plasmonic dye-sensitized solar cell (PDSSC)

Because of its cheap manufacturing cost and excellent conversion efficiency, the PDSSC has gained appeal. As indicated in the first chapter, several attempts have been made to optimize the parameters and performance of the gadget.

3.4.2. Plasmonic metal nanoparticles

When the incident light activates them, the metallic nanoparticles (NPs) are affected, and this is what we observe in a large number of applications that have benefited from the use of these nanomaterials, such as solar cells and gas sensors [129].

The brilliant color of noble metal NPs results from LSPR or collective oscillation of conduction band electrons. The LSPR in nanoparticles of noble metals significantly boosts light absorption, such as strong light scattering, allowing subwavelength antennas to absorb more light and generate plasmon-polaritons from incident light.

In addition, the electromagnetic field close to metal nanoparticles can be substantially amplified [130].

Studies of gold nanoparticles (NPs) were first brought to scientific attention thanks to Michael Faraday's work with colloidal gold solutions. Due to their outstanding SPR optical capabilities, Au and Ag NPs are the most often utilized noble metal nanoparticles for initiating plasmonic events [131].

Au NPs are widely used in nanosphere applications because of their stability in air and LSPR wavelength of more than 500 nm. On the other hand, Ag nanoparticles have a strong efficiency scattering and an LSPR wavelength range of 400-500 nm [132].

Modifying the LSPR of plasmonic NPs of metal is possible by altering size and shape. Unlike spherical NPs, anisotropic NPs like nanoplates, nanorods, nanostars, and nanocubes, increased surface area, more excellent absorption and extinction rates, and the increase of electromagnetic fields at the edges and corners [133].

Additionally, as shown in (Figure 3.8), the NPs that anisotropic has a wide absorption band that includes light region (NIR) near-infrared, in contrast to the spherical Au or Ag NPs, which typically exhibit a distinct absorption zone at around 400 or 500 nm [134].

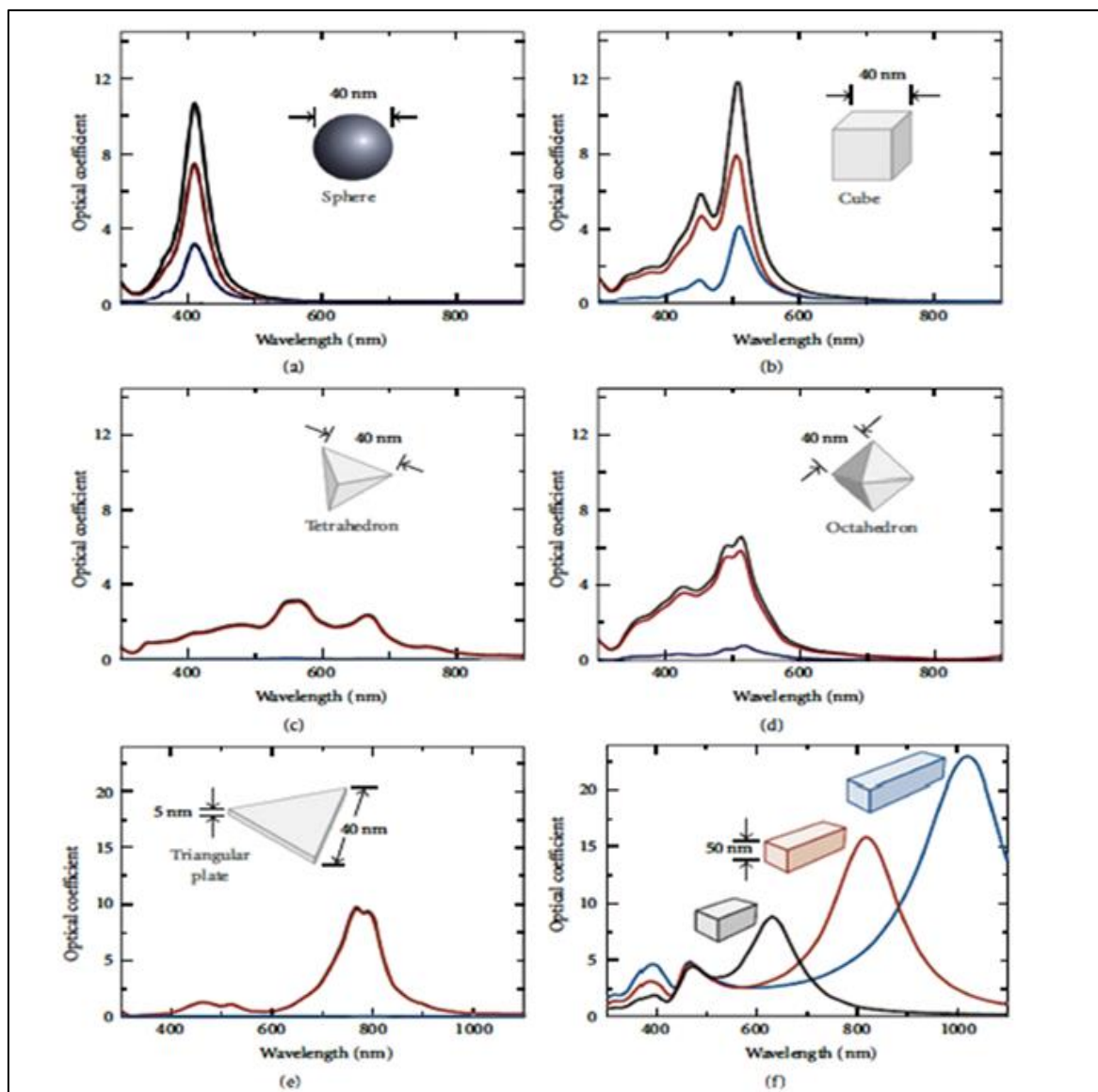


Figure 3.8. Shows estimated the extinction (black), absorption (red), and scattering (blue) spectra for a) spherical, b) cuboid, c) tetrahedral, d) octahedral, and e) triangular plate-shaped Ag nanoparticles. Black, red, and f) red extinction spectra of rectangular bars with 2, 3, and 4 aspect ratios (blue) [134]

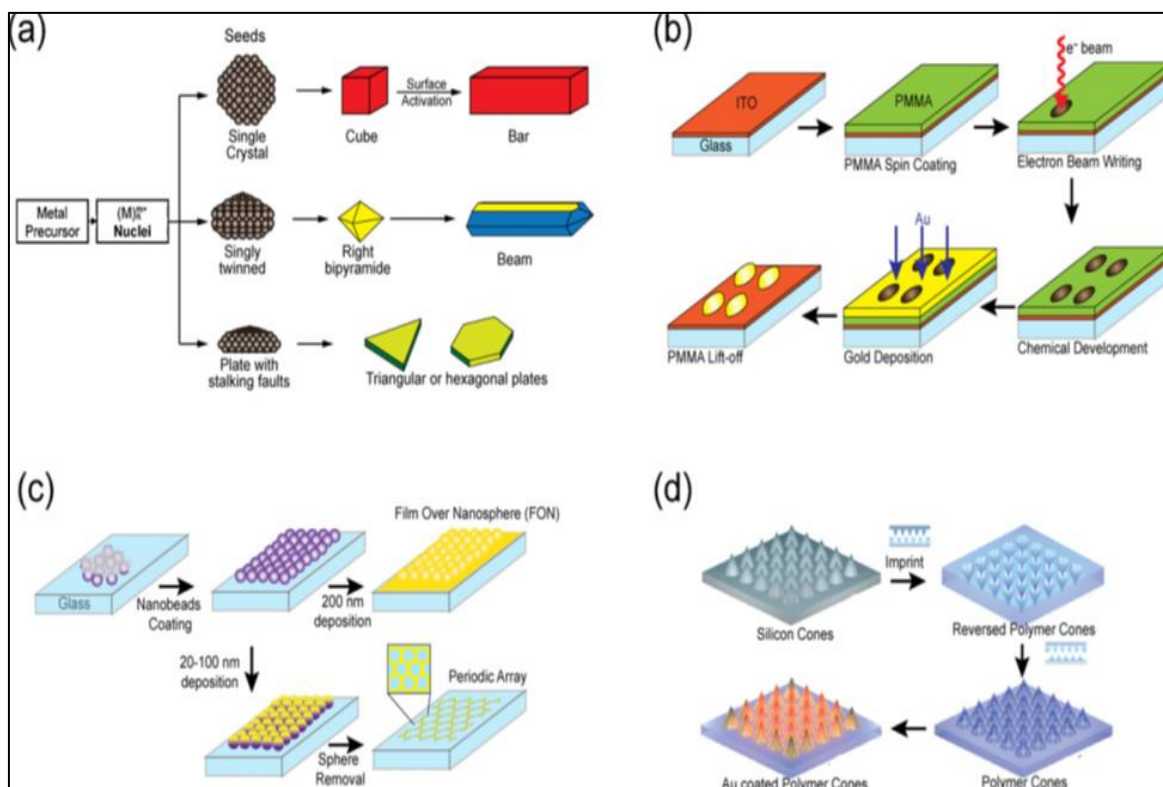


Figure 3.9. Different methods exist for fabricating substrates. a) The chemical reduction mechanism mediated by water-soaked seeds. (b) The basic idea behind electron beam technology. (c) method of lithography using nanospheres. (d) A schematic showed how 3D gold-coated nanocones are created using nanoimprint lithography in the nanofabrication process [134]

3.4.3. Methods of metal nanoparticle synthesis

Many techniques are utilized to manufacture metallic nanoparticles, and they can be broadly categorized as either "bottom-up" or "top-down."

The results are displayed in (Figure 3.10) [135]. The raw material used to prepare the nanoparticles is the primary difference between the two strategies. In contrast to bottom-up approaches, which begin with individual atoms or molecules, top-down approaches begin with a larger quantity of material and then employ a combination of physical, chemical, and mechanical processes to further refine the particle size down to the nanometer range (Figure 3.11) [136].

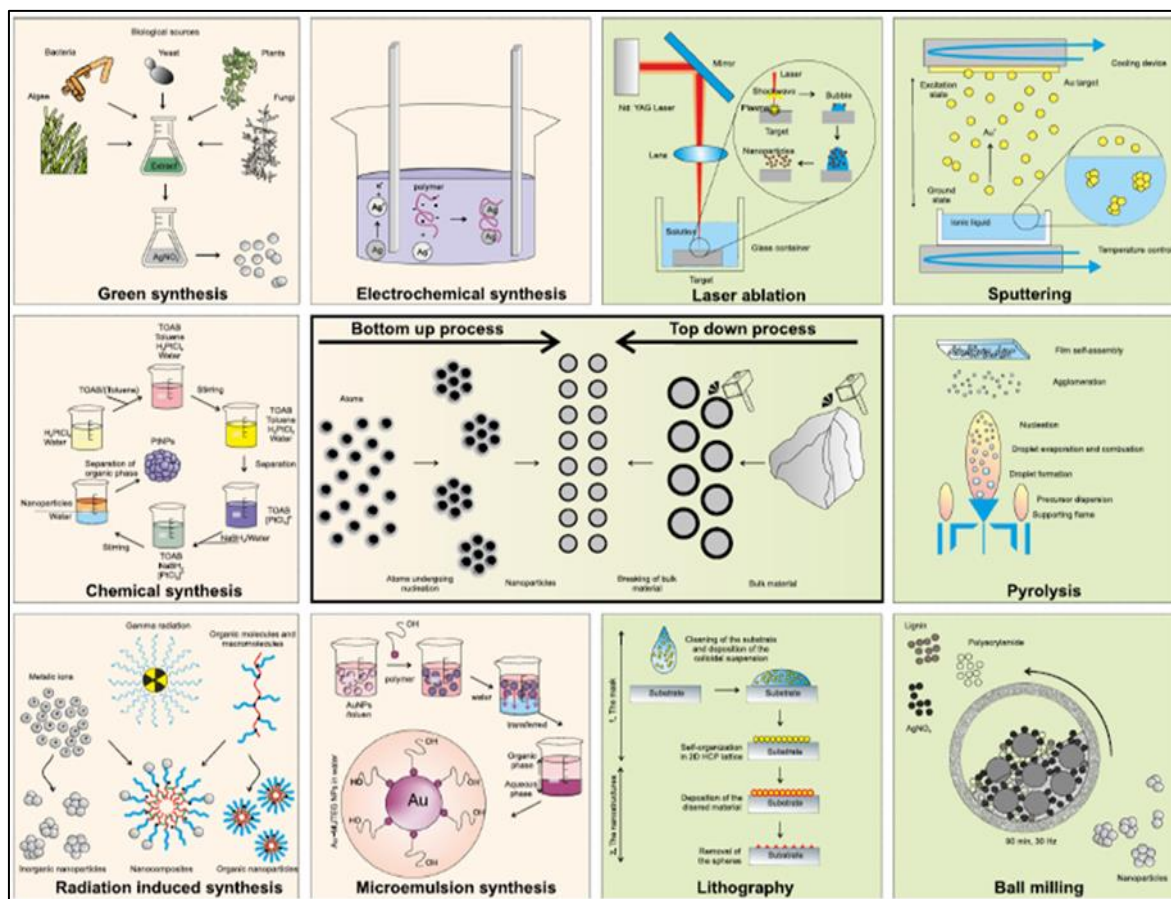


Figure 3.10. Top-down (shown in the photographs with a green backdrop) and bottom-up (not shown) perspectives are depicted schematically (images with pale yellow background) methods for creating nanoparticles [135]

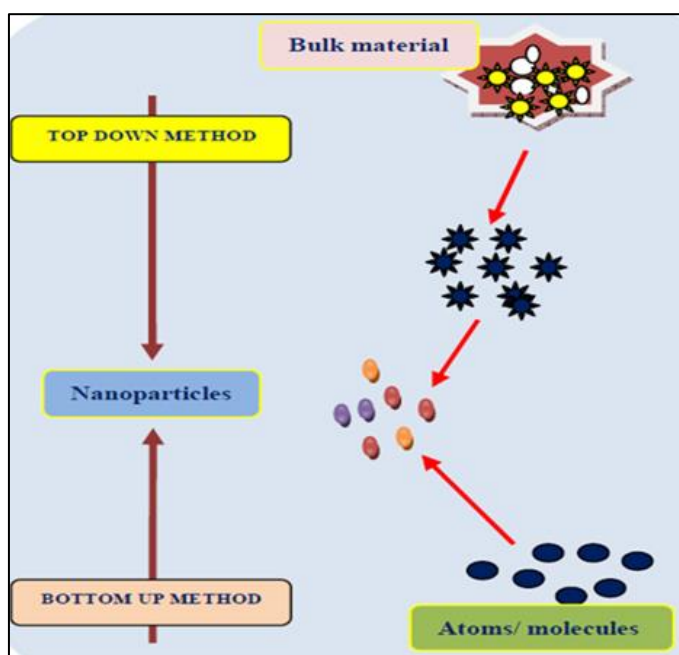


Figure 3.11. Brief summary of bottom-up and top-down techniques [136].

Top-Down technique: the material in this technique is shrunk down to nanoparticle size. Several physical and chemical methods are used to reduce the size of the starting material to create nanoparticles; this process breaks down the material into tiny particles called nanoparticles [137,138].

The use of laser ablation was fundamental to our research. Nanoparticles can be synthesized using laser ablation by directing a powerful beam of laser onto the material. In the laser ablation process, nanoparticles are created when material of the source or precursor is vaporized because of intense laser irradiation. Laser ablation for creating nanoparticles from a noble metal can be considered environmentally friendly because no stabilizing agents or other chemicals are required; metal nanoparticles are just one of the many nanomaterials that can be made using this technique [139].

The materials most commonly used to create nanoparticles are carbon, ceramics, and oxide composites [140-142].

Using the pulsed laser ablation technique in liquids to produce solutions of monodisperse colloidal nanoparticles devoid of ligands and surfactants is a novel and intriguing technique. As depicted in (Figure 3.12), nanoparticle attributes such as average size and fluency can be changed to affect dispersion, wavelength, and addition of laser salt [143].

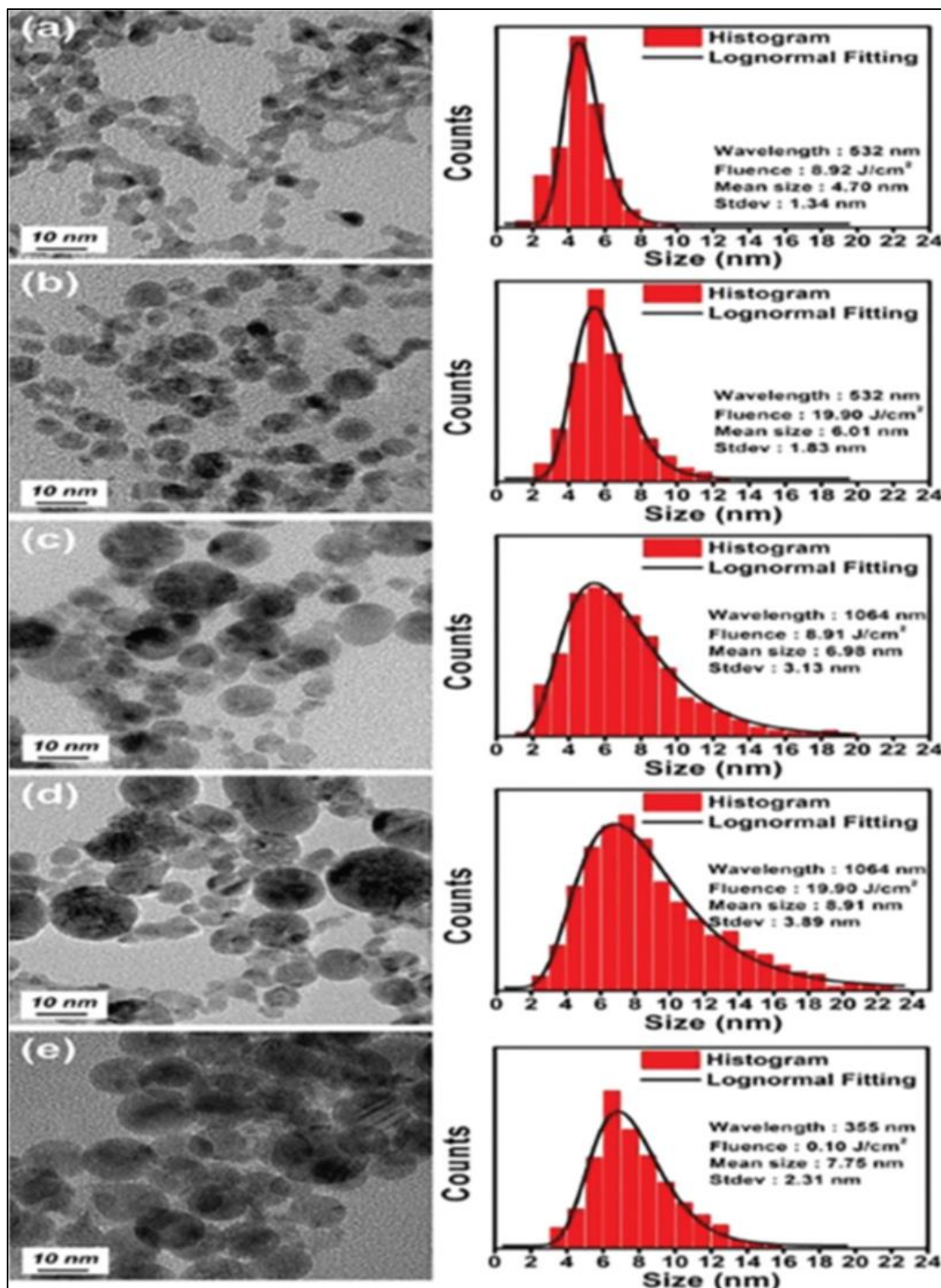


Figure 3.12. TEM pictures, average and standard deviations of Pd sizes (Palladium) Laser ablation in water at (a) 532 nm, $8.92 J/cm^2$, (b) 532 nm, and $19.90 J/cm^2$, (c) 1064 nm, $8.92 J/cm^2$, (d) 1064 nm, $19.90 J/cm^2$, and (e) 355 nm, $0.10 J/cm^2$ produced nanoparticles of different sizes and shapes [143].

Bottom-up technique: This alternative method is more cost-effective. The term "bottom-up approach" refers to the method of building molecule by molecule, materials atom by atom, or cluster by cluster. As illustrated in (figure 3.13), several of these technologies are still in the research phase or are only beginning to be applied to the commercial production of nano powders.

Light nanoparticles can be made using various well-documented bottom-up methods, including the reverse-micelle route, template-assisted sol-gel, electrodeposition, colloidal precipitation, hydrothermal synthesis, and the organometallic chemical route [144].

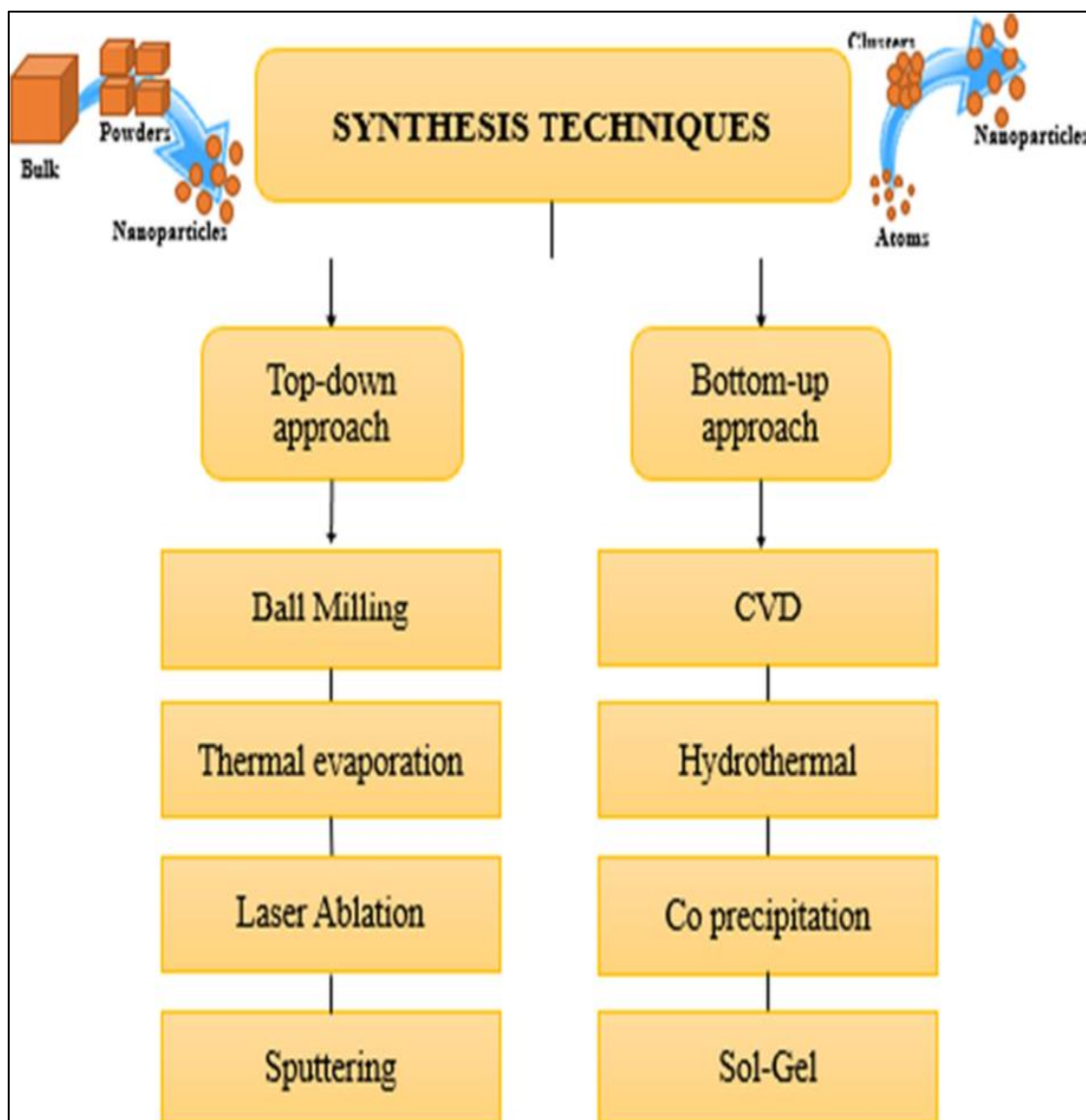


Figure 3.13. Shows that nanostructures can be created using either bottom-up or top-down manufacturing processes [144]

3.5. The Mechanisms of Laser Liquid Ablation

3.5.1. The mechanisms of Laser ablation using bulk Metal targets in liquid

When laser pulse radiation impacts the surface of a bulk metal, plasma, gas phase, or metal, minute quantities of liquids are generated as the principal outputs, which subsequently interact with the surrounding solution to form nanoparticles. Among the three possible products, lasers with high energy density and short pulse widths, gas phase, and plasma can be formed [145].

Tiny amounts of liquid are the principal byproduct of pulse laser radiation striking the surface of a bulk metal, plasma, gas phase, or metal, and these liquids eventually combine with the surrounding solution to form nanoparticles. When Lasers having a pulse width of several nanoseconds and a power density of 10^8 to 10^{10} W/cm² are one type that can produce a gas phase or plasma. Nanodroplets, however, were discovered to be the major product when low-power density lasers (such as millisecond lasers) were utilized [146].

3.5.2. Mechanism of Thermal Evaporation

The theory of laser ablation is based on the melting, evaporation, and subsequent solidification of metallic substances. Essential for comprehending the results of laser ablation on bonding [147]. In (Fig.3.14), we see how the laser beam travels from the emission source to the surface of the metallic substance, where the material absorbs the laser pulses' energy during the laser ablation process [148].

The metal is then heated until it melts and vaporizes. The vaporized material condenses into a plasma plume near the laser pulse's leading edge, where it stays for the length of the pulse. The rapidity with which the plasma plume is generated results in a very high internal pressure (rebound pressure) [149].

It can collect metal from the laser beam's periphery without disrupting the beam's center. When the molten metal is thrown, it falls back to the surface and re-solidifies, leaving a coating of debris [149].

The laser formed a crater so the molten metal could not be splashed out by the rebound force. A small amount of vaporized metal is bound to rise to the surface from within the molten metal, and tiny cracks might form as the metal cools and solidifies [150].

The structure and morphology of the metallic adherend surface after laser ablation also affect adhesive-bonded connections' strength and corrosion resistance. Laser ablation alters the constitution and morphology of metallic adherend surfaces [149].

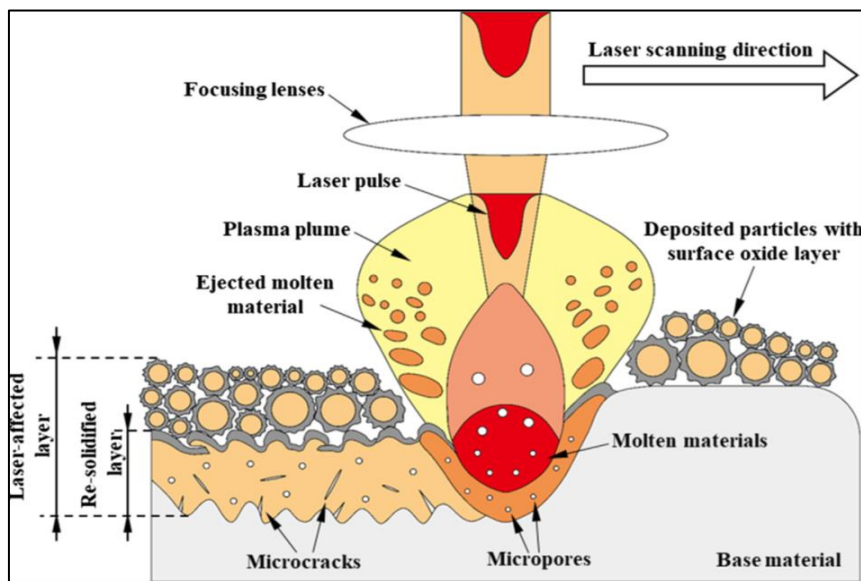


Figure 3.14. Laser ablation's interaction effects [150].

3.5.3. Mechanism of explosive ejection

The initial metal droplet is formed when pulse laser radiation strikes the surface of bulk metal, melting the area around the laser spot. The high-pressure vapor shatters the original millimeter-sized metal droplet, resulting in the explosive ejection of countless smaller metal nanodroplets (Figure 3.15 a). Afterward, the metal nanodroplets affect the surrounding fluid via their surfaces (Figure 3.15 b). Each type of nanoparticle is produced by a unique combination of laser settings, target material, and solvent, with the latter two influencing the shape and size of the product. Different nanostructures can be created in the Pb/S system, as shown in (Figure 3.15c) [151].

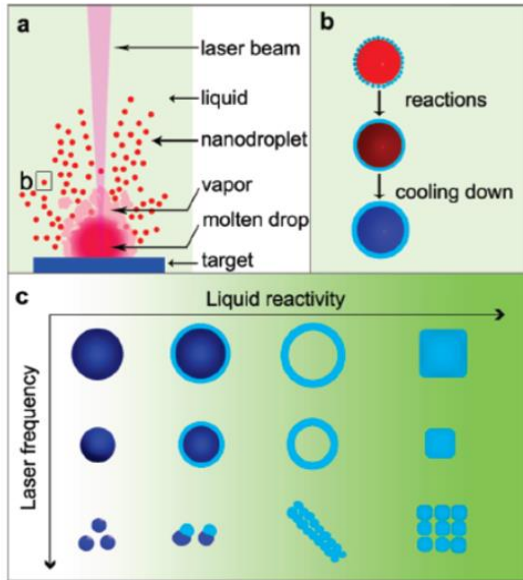


Figure.3.15. Diagrammatic depictions of nanodroplet ejection and nanostructure production [151].

3.5.4. Physical and chemical changing processing over time in LAL. For t less than zero: Pulse infiltration in the solution

The laser beam has to go through a layer of solution on top of the target. The pulse laser should only send its power to the target and not to the liquid around it. Between $t = 0$ s and τ_{pulse} : absorption of the laser pulse, solution breakdown must be avoided.

As a result, the high photon density of both nonlinear processes and linear absorption is observed when the pulse laser's energy strikes the bulk metal's surface.

Depending on the material's skin depth, the laser electromagnetic wave's amplitude at the target surface decreases to $1/e$ of its initial value.

Nonlinear optical effects have been seen as a laser intensity function, corresponding to laser fluence divided by τ_{pulse} time. The ablated material is disconnected from $t=10^{-12}$ s - 10^{-10} s.

After laser absorption and direct photoionization, the regionally induced electron-ion collisions and space-charge separation fields initiate the separation of matter from the surface of the target within 10^{-12} seconds.

The separation is also maintained by heating the lattice, which takes many picoseconds. Plasma plume growth and extinction between $t = 10^{-10}$ s and 10^{-7} s. After a laser pulse, the mechanics of laser ablation in gas or solution are remarkably similar in the first few picoseconds. However, a significant difference is observed around $t = 10^{-10}$ – 10^{-9} s because the solution buffer severely limits the plasma plume to the crater area.

The plasma plume typically dissipates within 10^{-8} to 10^{-7} seconds. On a timescale of 10^{-7} – 10^{-6} s, the energy released to the surroundings solution by the plasma plume causes a cavitation bubble, which extends to 10^{-4} seconds.

For $t > 10^{-4}$ seconds, nanomaterials develop slowly and aggregate. When the cavitation bubble bursts, it sends out a shockwave, and nanomaterials and surrounding solutions enter a physical and chemically stable state. Nanostructures undergo modest alterations due to the condensation of ablated atoms and molecule clusters in liquid [151,152].

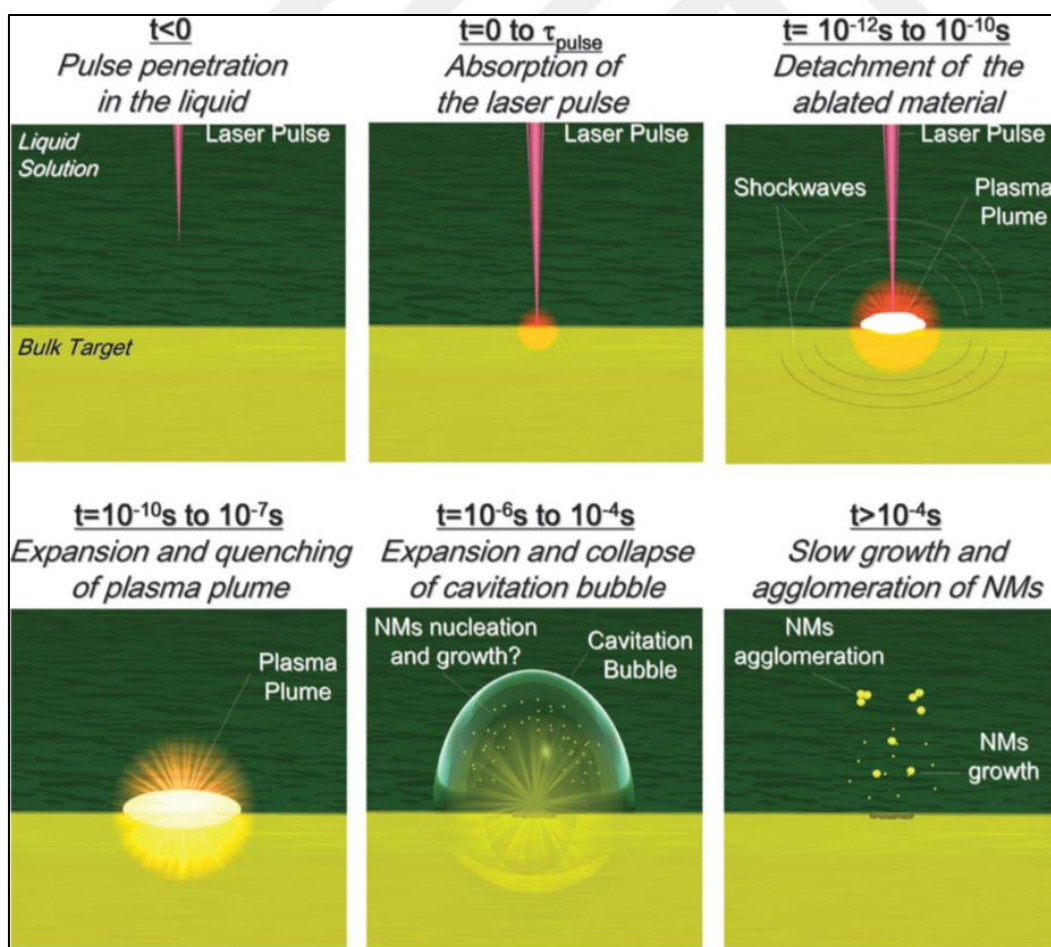


Figure 3.16. LaL timeline sketch with ns pulse ablation [152].

3.6. Laser Ablation in Liquid-Formed Nanomaterials Applications

3.6.1. Noble Metal NPs functionalized for bio applications

Bioconjugate nanoparticles are garnering attention as a promising new class of bioanalytical and biomedical instruments. Colloidal aggregates between biomolecules and gold nanoparticles can be created using laser ablation. That occurs at higher biomolecule-to-nanoparticle ratios (40-70 nm) [153].

3.6.2. Semiconductor NPs for applications in luminescence

Toluene molecules were used as a carbon precursor, and laser ablation was utilized to produce hollow carbon shells and carbon spheres resembling fullerene. Scientists in optics are curious about the strong and excitation wavelength-dependent light emission of carbon shells resembling graphene [154].

3.6.3. Applications for Surface Enhanced Raman Scattering (SERS) Detection Using NP Thin – Films

The Surface enhanced Raman spectroscopy (SERS) experiments conducted by Besner and Meunier showed that gold-silver nanoalloys, which obtain a much better anti-oxidant compared to pure Ag and a much larger and narrower SPR compared to pure Au, are likely to have the highest degree of agreement in terms of steady chemical state and plasmonic response [155].

3.6.4. Nano fertilizers for Increasing Seed Germination and Growth

When using nano-fertilizers, plant growth efficiency, soil quality, and the yield of high-quality fruits and grains all increase considerably. The widespread use of synthetic chemical fertilizers, which may be harmful to individuals and the environment and may be expensive for farmers, makes macro-micronutrient management a complex problem on a global scale [156].

3.7. Nanoparticle characterization

Characterization of nanomaterials is essential for learning about their properties and potential uses.

3.7.1. X-Ray Diffraction (XRD) characterization techniques

The unit cell size, bond angles, chemical content, and crystallographic structure of natural and synthetic materials can all be determined using X-ray diffraction (XRD), a method of non-destructive analysis [157]. Constructive x-ray interference with the desired crystalline sample forms the basis of XRD. A CRT's x-rays are focused, collimated, and filtered before being shone on the specimen. Bragg's rule, which connects wavelength to diffraction angle and lattice spacing, describes the ensuing interaction that results in constructive interference (Figure 3.17) and shows a diagram of XRD working equipment [158].

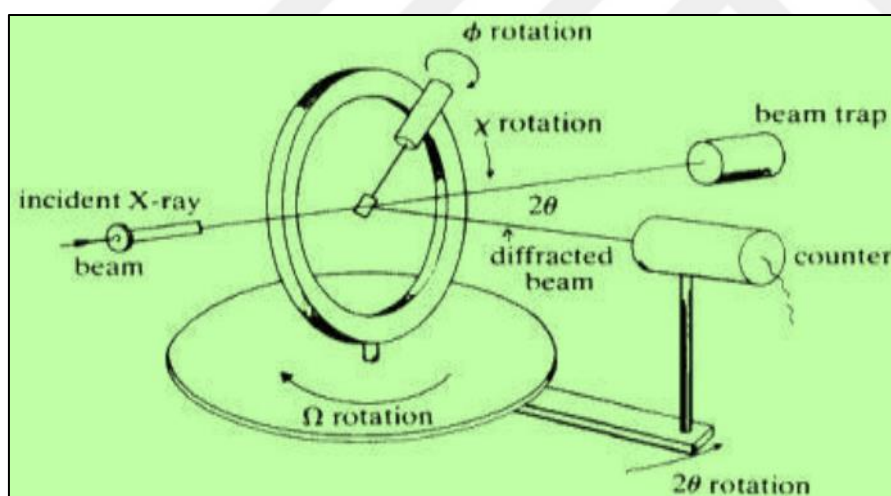


Figure 3.17. A Diffract Meter Schematic Diagram with Four Circles [158]

Powder (XRD) diffraction is the fastest method of analysis that can reveal data such as the unit cell size and atomic spacing, making it helpful in determining the phase of crystalline materials. By applying Bragg's Law that $n\lambda = 2d \sin\theta$, monochromatic photons incident on the sample will experience constructive interference. By scanning a crystalline sample through a precise configuration of two angles, we may calculate the lattice spacing by using this equation, which creates a link between the electromagnetic radiation wavelength, diffraction angle, and lattice spacing [159].

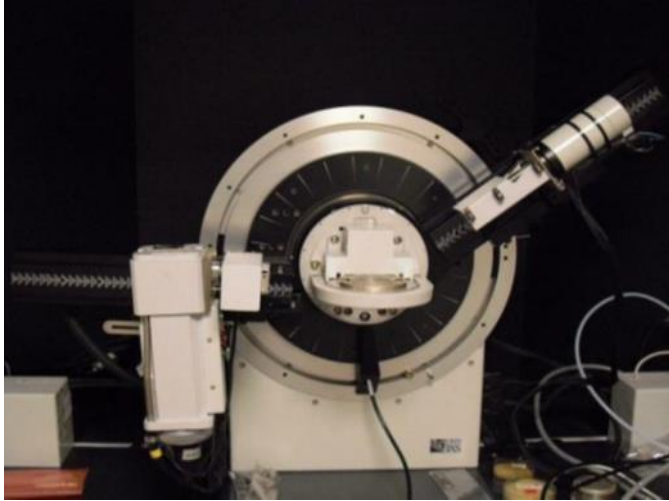


Figure 3.18. Instruments for X-Ray Diffraction [158].

3.7.2. Calculation of crystal grains' size

The terms "particle size" and "grain size" are used when the dimensions of individual crystals are less than about 100 nm; this is because a particle crystalline powder sample, in general, contains several fine units termed "crystallites," which can be considered as a single crystal, as shown in (Figure 3.19).

When discussing a factor that contributes to diffraction peak broadening in XRD analysis, "the size of a crystal" refers to the "size of crystallites" [160]. The XRD peak profile obtained from a powder specimen with less than 5 nm will indeed vary from that of an identical specimen with crystallite dimensions in the normal range of 500–10000 nm. However, peak broadening in the measured XRD has been seen if the crystallite size of the specimen decreases to below 100 nm.

Because of restrictions on the possible atomic locations inside the periodic zone, only a small subset of elements can generate the same XRD peak profile [161].

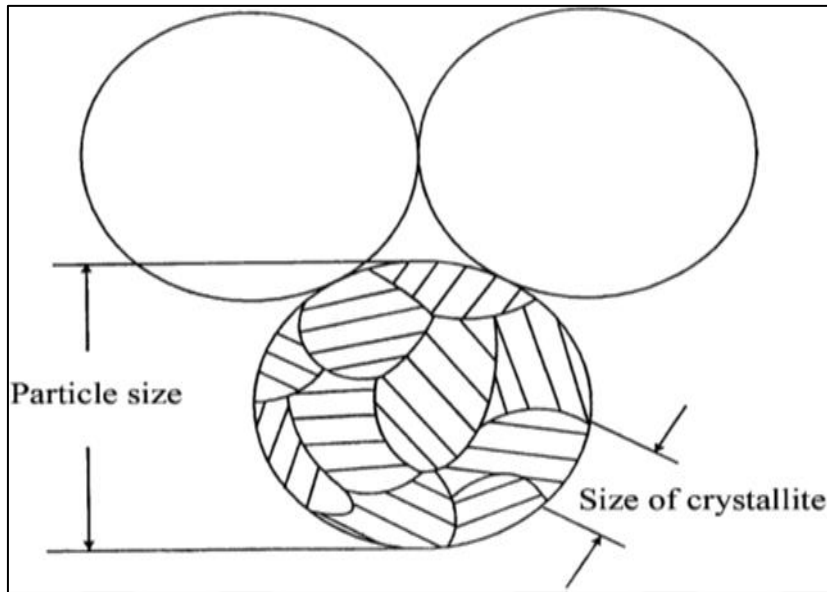


Figure 3.19. A crystalline powder example's grain size and crystallite distribution are depicted in this schematic illustration [161].

According to Bragg's formula:

$$n\lambda = 2d \sin \Theta \quad (3.17)$$

Here, Θ represents the angle of the incidence ray and the scattering surface, d represents the distance between crystal layers, n represents integer, and λ represents wavelength of XRD [162].

$$d = \frac{a}{\sqrt{h^2 + k^2 + l^2}} \quad (3.18)$$

Calculating the distance between crystal planes using Bragg's equation gives d , where a is the lattice constant, and hkl is the mirror surface [162].

When the material is plastically deformed, the lattice planes bend, and the distance between any single set varies from grain to grain, resulting in peak broadening. A Scherrer constant K_S can be introduced into the Scherrer equation to account for the influence of form if the grains' form is described by a single form parameter D [163].

$$D = \frac{K\lambda}{\beta \cos \theta} \dots \quad (3.19)$$

Where D represents the grain size of the crystal, λ is the X-wavelength (0.1541 nm), and θ is the diffraction angle. The range of the Scherrer constant K is 0.62 to 2.08. K is usually had a value equal to 0.89, which is related to the reflection and crystal forms. It is crucial to recall that when K is assumed to be 0.89, its value is expressed as a radian. β is the value of the FWHM, which must also be expressed in radians [164]. The formula was used to determine the dislocation density or the number of dislocation lines per unit volume of crystalline materials (δ) [165]:

$$\delta = \frac{1}{D^2} \quad (3.20)$$

Where D is the crystal size. To calculate microstrain in the film, we used the equation

$$D = \frac{k\lambda}{\beta \cos\theta} \quad (3.21)$$

D represents crystal size, shape factor k , X-ray incident wavelength λ , β represents the (FWHM), full peak width at half maximum and measured in radians, and θ represents Bragg angle [166].

The contribution of the microstrain to the line broadening of the diffraction peak is defined by Stokes and Wilson equation [166].

$$\beta = \varepsilon \tan\theta \quad (3.22)$$

where ε is the microstrain.

3.8. Optical Characterization Techniques

3.8.1. The UV-Visible spectroscopy

This technique compares the amount of visible light absorbed or transmitted by a sample to that of a standard or blank sample. This characteristic is affected by the sample's makeup, which may reveal details about the sample and its concentration [167]. In addition to varying from other surrounding regions in wavelength, energy, and excitation type, this radiation's spectrum ranges from 190 to 800 nm. Attenuation is brought about through reflection, scattering, absorption, and interference. Nevertheless, it is possible to precisely quantify the attenuation by recording the light source's absorption. Up to a certain point, when light is shone on a sample, the amount it absorbs depends on the analyte's concentration and the distance of the light source from the sample [168].

Using a UV/VIS spectrophotometer, one can determine the concentration of a sample solution that is contained within a cuvette by comparing the light's intensity through the simple both before and after it has been passed through the cuvette.

A UV/VIS spectrophotometer consists primarily of a monochromator, sample holder, light source, and an appropriate detector, as shown in (Figure 3.20). Nanostructures' optical properties are major to study from a technical and practical standpoint because they provide information on the efficiency of electronic transitions, the installation of energy packages, and the features that affect how light interacts with the material [169].

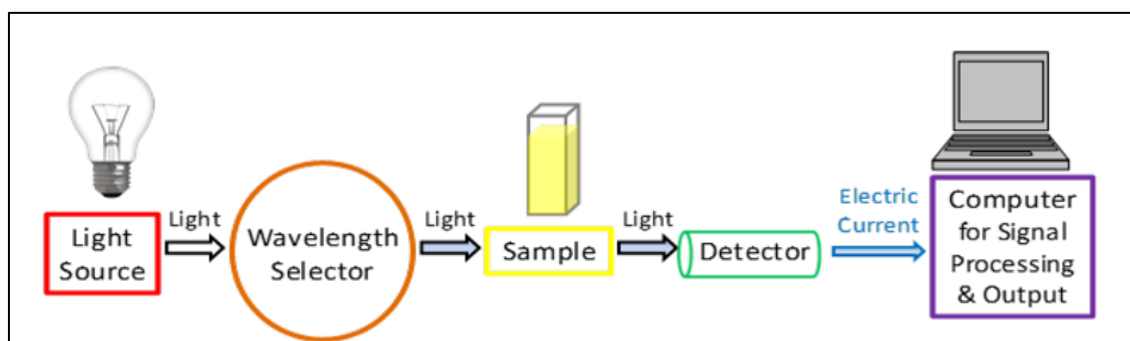


Figure 3.20. Schematic of UV-Vis spectrophotometer's main components [169].

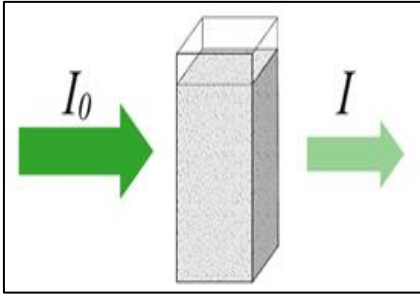


Figure 3.21. Transmitt [169].

$$T = \frac{I}{I_0} \quad (3.23)$$

The term "transmittance," represented by the letter T, is the ratio of the two intensities "I" and "I₀," and its unit is percent [170].

UV/VIS spectroscopy primarily, but not exclusively, measures transmittance. Absorption A is a supplementary UV/VIS result. It is the inverse logarithm of transmittance [170].

$$A = -\log(T) \quad (3.24)$$

The optical energy separation was found to be dependent on the absorption coefficient. Such a formula was used to determine the absorption coefficient [171].

$$\alpha = \frac{2.303}{t} \ln\left(\frac{1}{T}\right) \quad (3.25)$$

The unit defines the coefficient of absorption (cm⁻¹). Eg calculated using the transition between the valence and conduction bands [172].

$$ahv = B(hv - E_g)^{1/2} \quad (3.26)$$

When B is a constant, the photon energy is denoted by hv, and n is ½ for the indirect and 2 for the direct band gap.

3.8.2. Photoluminescence (PL) spectroscopy characterization techniques

Photoluminescence spectroscopy, more usually abbreviated as PL, happens when any substance-induced emits photons to emit photons of light energy.

It is a method for evaluating materials that do not entail physical contact or destruction. Photoluminescence has the potential to yield two distinct outcomes when applied to fluorescence spectroscopy: fluorescence and phosphorescence.

In order to record photoluminescence spectra, the emitted light intensity is measured as a function of either the excitation or emission wavelength.

To acquire an excitation spectrum, one must observe emission at a predefined wavelength while simultaneously adjusting the excitation wavelength [173].

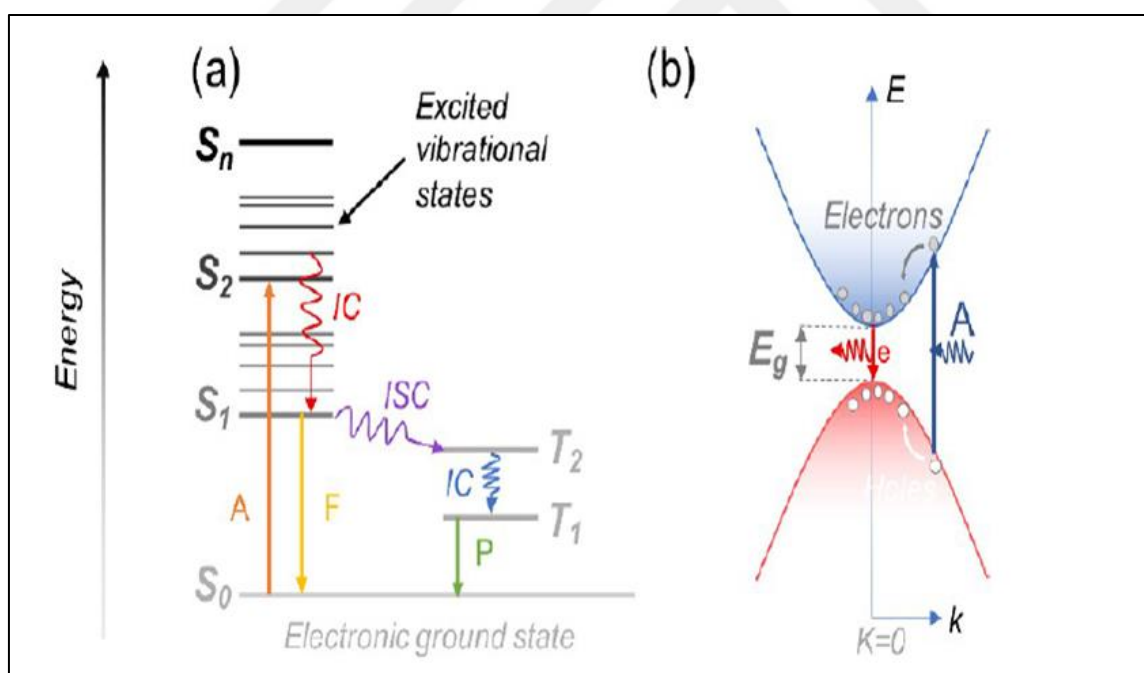


Figure 3.22. Displayed Organic (a) and inorganic (b) materials: PL reactions (direct bandgap). Some of the abbreviations used are internal conversion (IC), phosphorescence (P), absorption (A), fluorescence (F), intersystem crossover (ISC), emission (e), and bandgap (E_g). The "kinetic energy" of electrons or holes is represented by the letters "E" and "k," moment vector, respectively [173]

We use Planck's equation to determine the energy bandgap from the photoluminescence

$$E_g = \frac{1240}{\lambda_{nm}} \quad (3.27)$$

Where E_g denotes the energy gap (eV), and the wavelength is characterized by λ (nm) [174].

3.8.3. Transmission electron microscopy (TEM)

A sample is passed through an electron beam, which causes the particles in the sample to react with the electrons. The electrons that have passed through the sample are magnified and focused with an objective lens to produce an image.

In (Figure 3.23) depicts the core components of a TEM. Diffraction happens when an electron beam hits a sample. The diffraction strength will shift depending on the plane's relative position to the electron beam.

The electron beam is substantially diffracted at some off-axis angles and transmitted at others. Thanks to its ergonomic design, the specimen can be slanted to achieve optimal diffraction circumstances.

To generate a contrasting image, "light field" refers to the electrons that remain unscattered after being scattered away. Produce a dark field image; deflected electrons might be used [175].

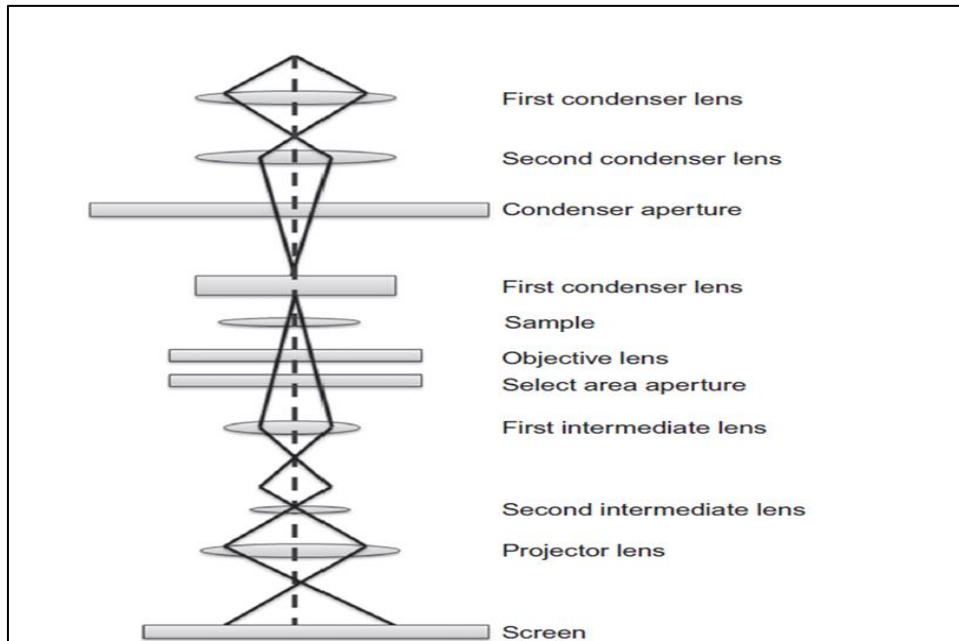


Figure 3.23. Essential Parts of the TEM [175]

3.9. Solar Simulator

When measuring the features of DSSCs, a stable light source similar to sunshine is required. A solar cell simulator is a light source that produces sunlight-like lighting and can be used to study the properties of DSSCs in laboratory settings. The current density-voltage (J-V) characteristics of DSSCs are examined utilizing an electrometer under AM 1.5 lighting (100 mW cm^{-2}) from a solar simulator (1 kW xenon with AM 1.5 filter) and (KEITHLEY 2400) [176].



4. EXPERIMENTAL PROCEDURE

The flowchart for experimental works, including laser ablation, is shown in Figure (4.1).

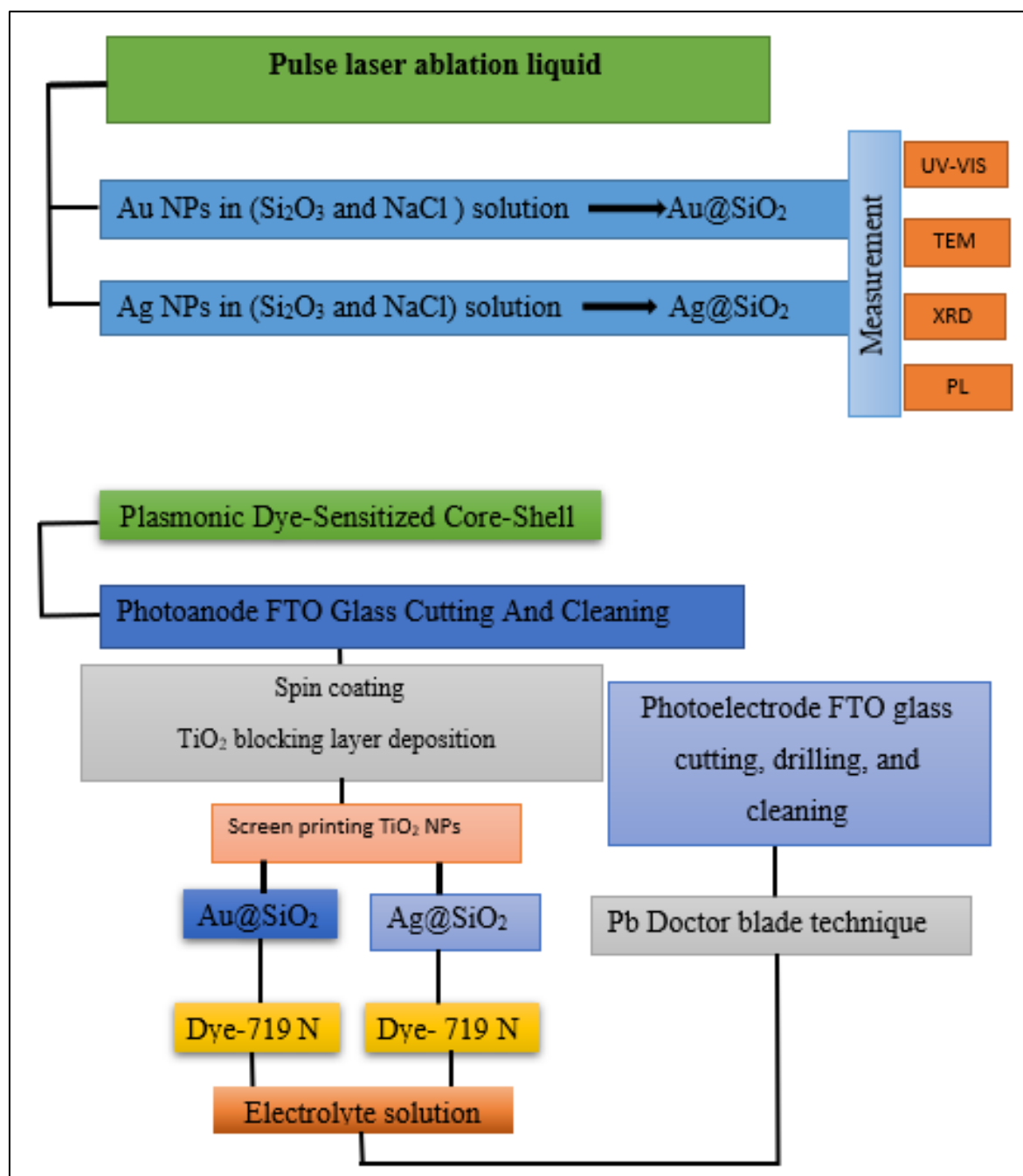


Figure 4.1. Flowchart of the experiment Works

4.1. Preparation of Metal@core-shell (Au@SiO₂ and Ag@SiO₂) Nanoparticles

4.1.1. The technique for pulse laser ablation in liquid

The experimental set-up for laser ablation of a metal target submerged in a solution of silicon dioxide is shown in Figure (4.2); the metal target was fastened to the bottom of a glass container. Nd: YAG (world health care) Laser fundamental wavelengths 1064 nm (pulse width: 7ns) were conducted to ablate a metal target. The focusing lens controlled the spot of the laser beam diameter.

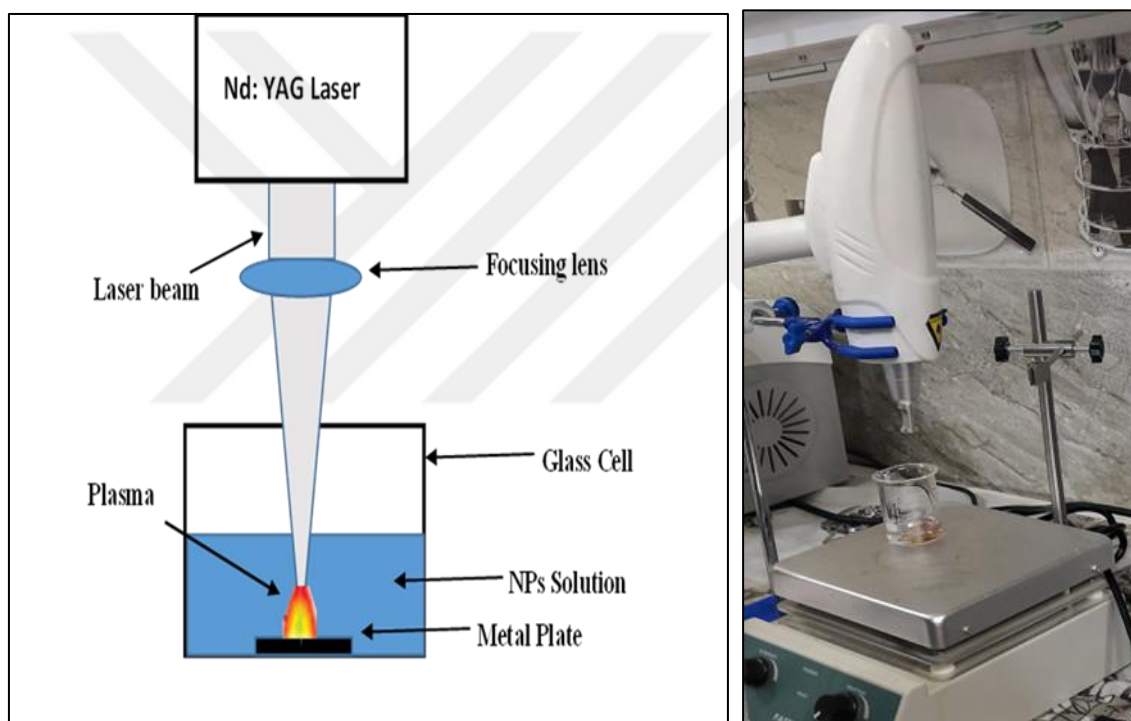


Figure 4.2. Shows PLAL system setup for the experimental

The laser interaction with the metal target produces a cracking sound and optical emissions during laser irradiation. Figure (4.3) is an optical emission image of a laser-irradiated spot on a gold target in our lab.



Figure 4.3. Optical emission from the laser interaction with the Au target

4.2. Materials

4.2.1. Materials for Laser Ablation Technique.

Target material

For noble metal nanoparticles synthesis, a proper amount (5 g) of gold and silver was cut from ounces (purity 999.9 %) to prepare target plates, a drawing machine was used to get 1mm thickness, and after that, the foil was cut to dimensions suitable for glass container size. A noble foil was washed in (acetone, ethanol, and deionized water for 10 minutes) for each solution with a 50 W ultrasonic cleaner. The cleaning process was repeated for each run. Figure (4.4) show images of a gold ounce and plate after drawing.



Figure 4.4. Gold target ounce from PAMP and plate target after drawing by draw machine

Deionized water

To avoid the impurities in tap water that affect the purity of suspensions, we used deionized water (DI); the DI water was purchased from the Iraqi Company for Water Treatment – Baghdad. They prepared high-purity water through a multistage process with an ion exchange method to remove cations and anions.

SiO₂ solution

A 0.0021 gm weight of sodium silicate (Na₂SiO₃ AVONCHEM with purity 99.5%) was taken (we used a sensitive weight scale in the applied physics department laboratory of technology university in Baghdad).

A 0.0058 gm weight of sodium chloride (NaCl, AVONCHEM with purity 99.5%) was taken (we used a sensitive weight scale in the applied physics department laboratory of technology university in Baghdad).

4.3. Dye-sensitized solar cell materials (DSSC)

4.3.1. TiO₂ paste

In order to create the DSSCs, Dyesol Ltd. of Australia provided DSL 18NR-T Transparent Titania pastes.

4.3.2. Dye type N719

The chemical formula for N719 Industry Standard Dye, M.W. = 1188.55, is C₅₈H₈₆N₈O₈RuS₂, and it was obtained from Dyesol Ltd. in Australia. The dye solution was produced in a 0.25 mM solution with absolute ethanol and kept in a sealed plastic box in a dark area.

4.2.3. Platine paste

The platinum precursor-containing PT-1 Screen printable paste was bought from Dyesol Ltd. in Australia.

4.2.4. (FTO) coated glass with fluorine-doped tin oxide

TEC8 Glass (100 x 100 x 3.2 mm), Soda-Lime Glass FTO (fluorine-doped tin oxide) is the conducting layer, and sheet resistance is 8/sq. Soda-lime glass is suitable for visible light and DSSC applications because of its chemical and physical characteristics.

4.2.5. Thermoplastic sealant

We bought Low-Temperature Thermoplastic Sealant MS004610 30 μm Surlyn from Dyesol Ltd in Australia (Sealing Temperature: 110-130°C, Melting Point: 93°C, Freeze Point: 61°C).

4.4. Experimental Procedure to Prepare Core-Shell Nanostructure

4.4.1. LAL Experimental Procedure

Gold core-shell SiO_2 , Silver core-shell SiO_2 prepared by using Nd: YAG laser (world health care) with fundamental wavelength 1064 nm (pulse duration ten ns, fluence 50 J/cm^2 , 100 J/cm^2 , 150 J/cm^2 , 500 pulses each time) to ablate Au, Ag targets which have been placed on the bottom of Pyrex glass vessel containing 20ml of prepared solution of (NaSiO_2) and colored sodium (NaCl).

Firstly: A 0.0021 gm weight of sodium silicate (Na_3SiO_2 from Sigma Aldrich) was taken (using a sensitive weight scale in the applied physics department laboratory of technology university in Baghdad).

Moreover, it dissolved in 100 ml of distilled water; the mixture was mixed in an electric mixer using a magnet bar for five minutes. Then, Micropipette took 0.02 ml of the solution, and we diluted the solution with 50 ml of distilled water to obtain a solution with a molar concentration of 0.04 μM .

Secondly: A 0.0058 gm weight of sodium chloride (NaCl , AVONCHEM with purity 99.5%) was taken (we used a sensitive weight scale in the applied physics department laboratory of technology university in Baghdad) and dissolved in 100 ml of distilled water.

An electric mixer was used to combine the materials using a magnet bar for five minutes, then 0.02 ml of the solution was taken using a micropipette and diluted with 50 ml of distilled water to obtain a molar concentration of 0.04 μM .

Thirdly: mix the two solutions for five minutes, using the Micropipette on the electric mixing device, and get a new solution. Shown in figure (4.2). The fluency of the laser beam is 50,100 and 150 J/cm^2 for Au and Ag targets; respectively, the fluence has been controlled by varying the laser energy, and the distance between the focusing lens and target surface was 10 cm; the space can be adjusted by moving the laser probe toward and backward the target by using a device holder.

A cracking sound, optical emissions, and a dense cloud colloid (which slowly became more apparent with a reduction in scattering) were noticed, indicating the success of the ablation process, figure (4.5).

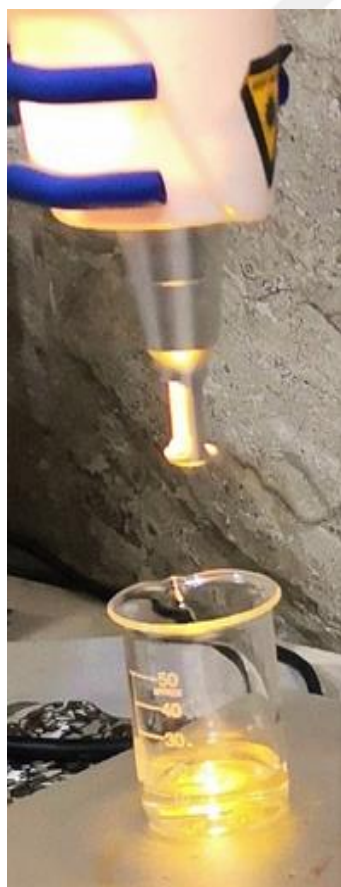


Figure 4.5. Illustrate the Au plate when pulsed by laser with fluence 50 J/cm^2

The change in the solution color indicates the formation of nanoparticles, the color change to red with the gold NPs and yellow with the silver NPs, solution. The nanoparticle solutions were stored in sealed Plastic tubes to make optical measurements later. As shown in figure (4.6).

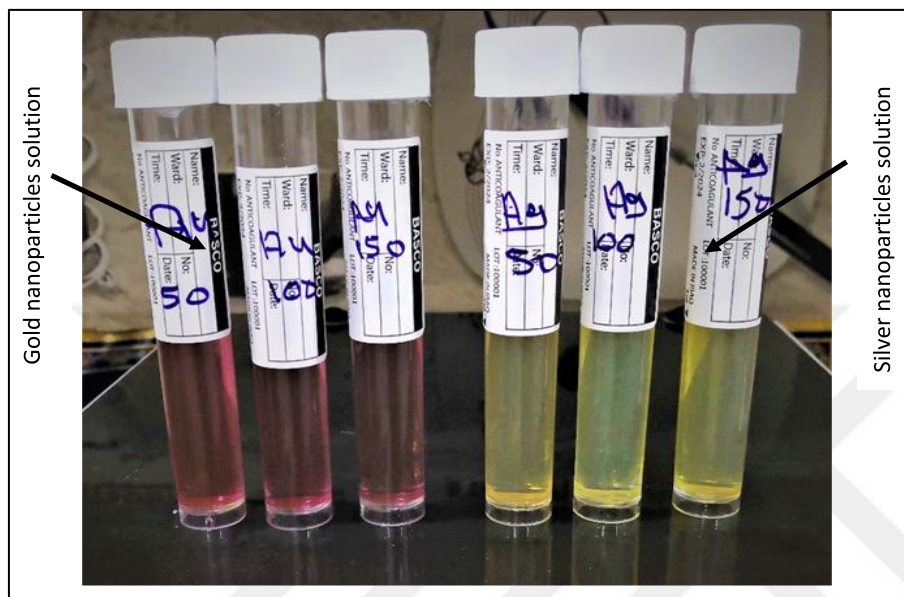


Figure 4.6. Nanoparticle solution

Next, the prepared nanoparticles were put in a centrifuge device (ARMAGHANTEP IRANIAN) to isolate the nanoparticles from the solution at a rate of 5000 rpm for five minutes. Moreover, clean them with distilled water to get rid of sodium chloride to obtain Au@SiO₂ and Ag@SiO₂ core-shell nanoparticles. Shown in Figure (4.7).



Figure 4.7. Centrifuge process

4.4.2. Film deposition

Figures (4.8) illustrate the schematic diagram of the method for preparation for Au@SiO₂ and Ag@SiO₂ films, respectively. The solution containing the nanoparticles was placed in a liquid handling system (micropipette device), an electric heater was also prepared, and the temperature was set at 100 degrees to evaporate the solution and keep the nanoparticles deposited on the slide.

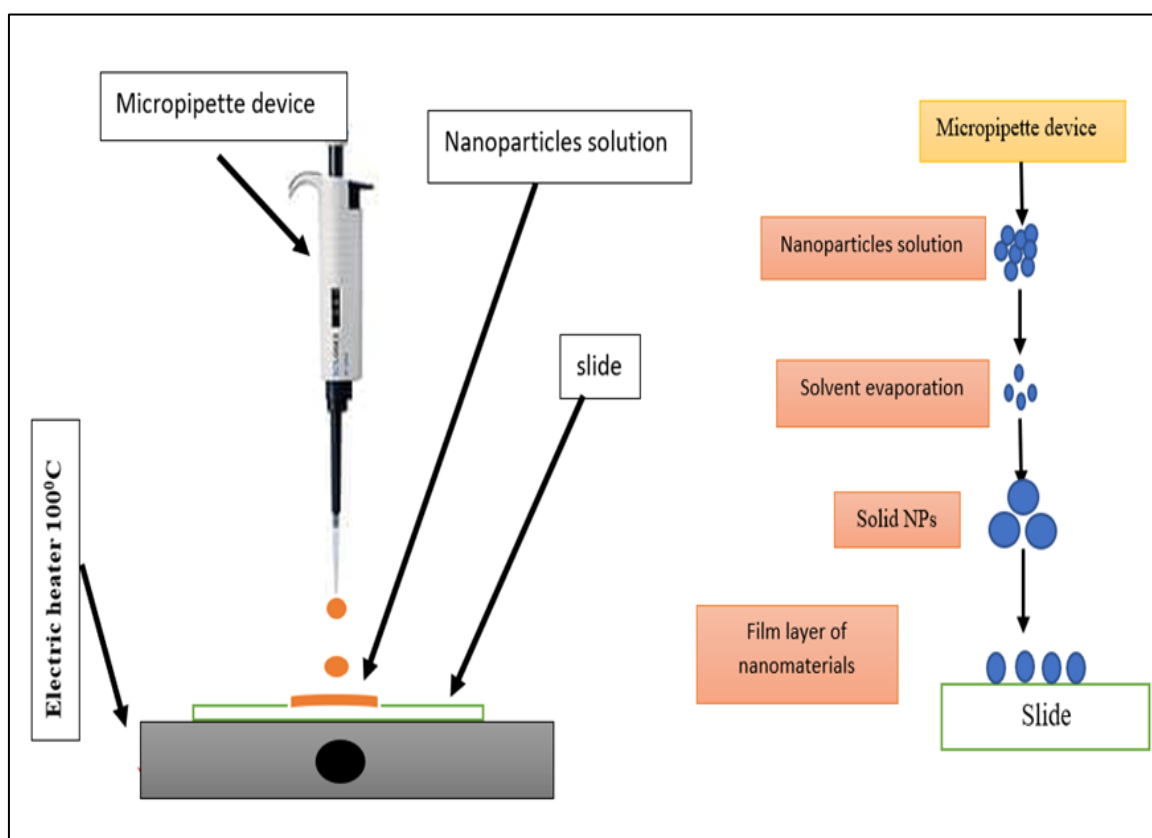


Figure 4.8. Diagram of the method for preparation for Au@SiO₂ and Ag@SiO₂ films, respectively

4.4.3. The screen-printing technique

Since the DSSC required thick film ($\approx 10 \mu\text{m}$) for photoanode, we used screen printing (45T). T refers to how many Threads per centimeter, not the size of the holes with a contact type of technique. Film positive was designed and put on the screen covered by light-sensitive emulsion and exposed in a high-lumen exposure unit.

Light-exposed areas harden while the protected areas by positive film remain soft and are removed by washing. A woven mesh was microscopically examined, and the result revealed that it is a Plain type, as shown in Figure (4.9).

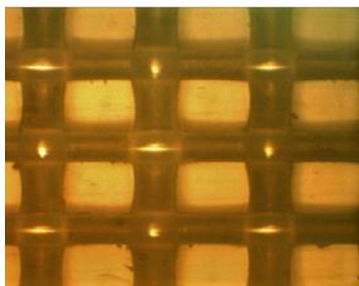


Figure 4.9. Optical microscope image of 45T

Figure 4.10 shows an image of the screens' final product (45T for TiO_2 paste) with designed geometric forms.

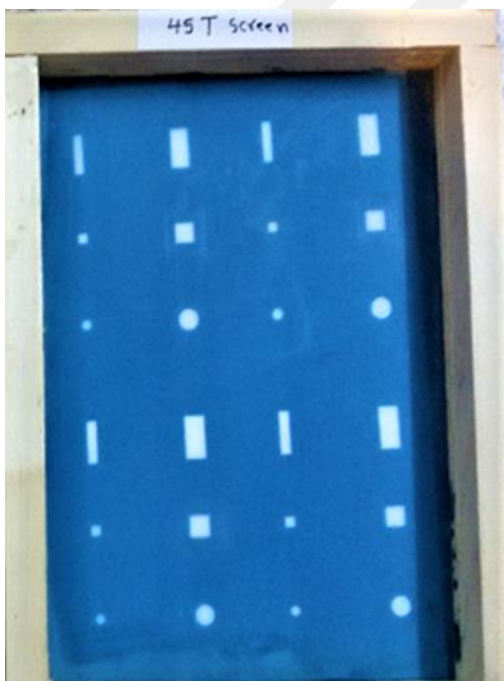


Figure 4.10. Screens (20 x 30 cm) with wood frames and 45T

The white geometric area is a non-exposed emulsion that allows TiO_2 paste to pass through and onto the FTO glass substrate.

TiO₂ paste is poured onto the screen and pulled across the geometric forms with a squeegee. Open areas in the design allow TiO₂ paste to pass through the screen onto substrates. Figure (4.11) shows images of TiO₂ films deposited by screen printing.

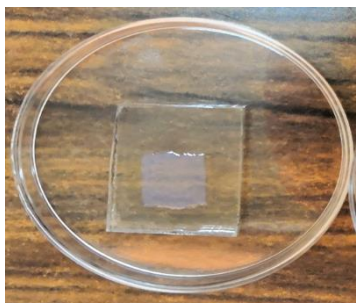


Figure 4.11. TiO₂ film deposited by 45T screen printing

4.5. Dye-Sensitized Solar Cell (DSSC) Preparation

Figure (4.12) shows the flow chart of Dye sensitized solar cell preparation. FTO glass plates (10 x 10 cm) were brought from Dyesol and used in the experiments. The glass plates were cut into 2.5 x 2 cm pieces with a glass cutter. The FTO glass was cleaned in an ultrasonic bath for ten minutes in acetone, and after these ten minutes in deionized water before using the FTO was dried with cigarette paper (Al-Sham co.). The method for depositing TiO₂ compact (blocking layer) was used filming on FTO substrates. The spin coating method was applied. By gently incorporating solution A into solution B while vigorously stirring, a TiO₂ precursor solution for the spin-coating process was created. In this experiment, solution A contains deionized water, 0.15 mL 20 wt.% nitric acid and 20 mL ethanol, while solution B contains titanium (IV) butoxide in a 25 mL ethanol solution. For the deposit of TiO₂ thin films on FTO substrates, the spin-coating conditions were 3000 RPM for 30 seconds. Aerosol spray-pyrolysis (Spray pyrolysis (SP) is a process in which a solution is sprayed onto a hot surface. The components react to generate a chemical compound, and a thin layer is deposited. The deposition of TiO₂ compact films was put in the oven at temperatures of 320 °C, 450 °C, and 500 °C on pristine FTO substrates., shown in Figure 4.13.

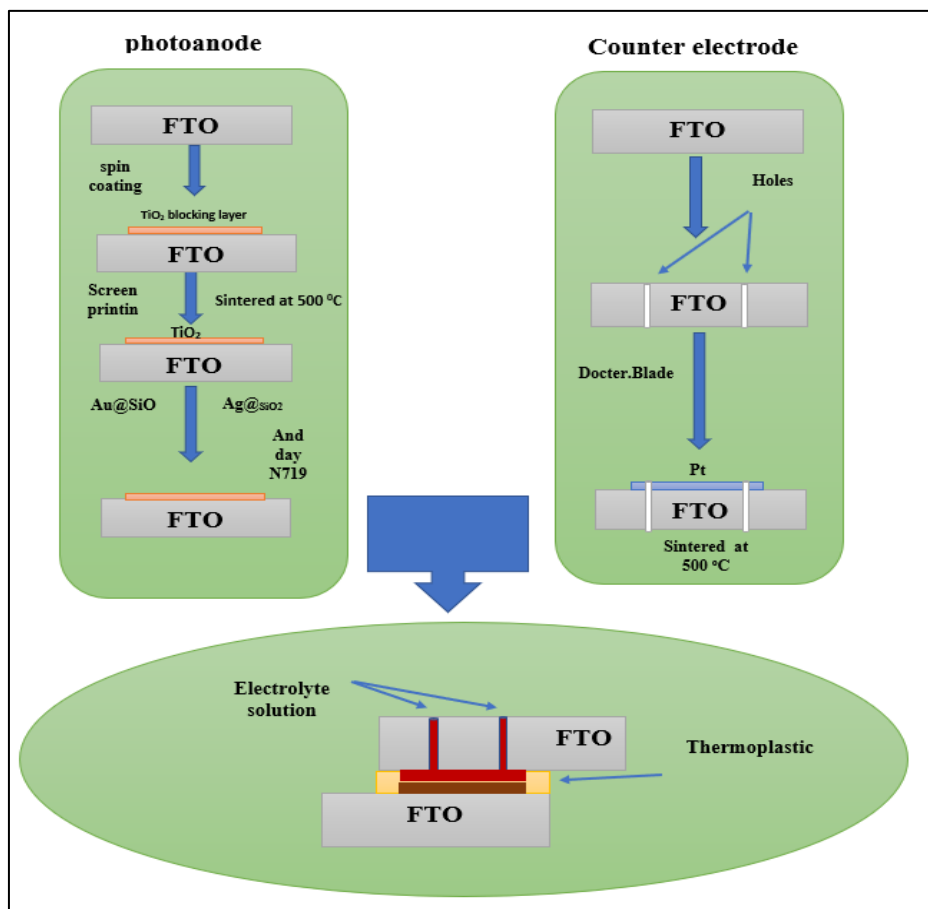


Figure 4.12. Flow chart of Dye sensitized solar cell preparation.

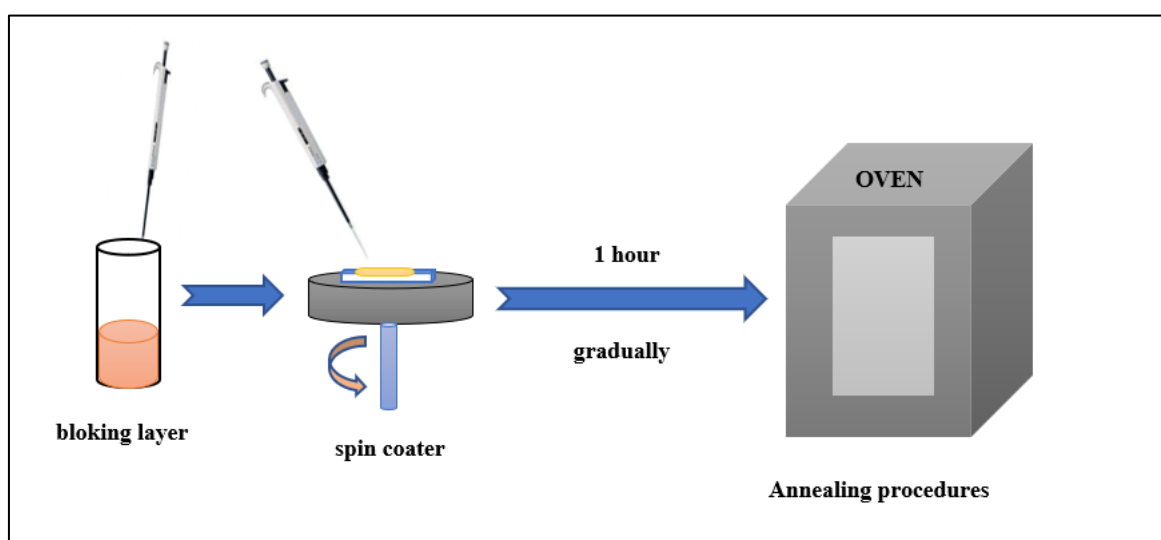


Figure 4.13. Coating the blocking TiO_2 Layer

Photoanode TiO_2 Nanocrystalline film ($10\text{ }\mu\text{m}$) was screen printed (45T) onto a glass FTO substrate, and thickness was measured using a (GUO GEN) Digital Micrometer that has $1\text{ }\mu\text{m}$

resolution. TiO_2 film was kept for 10 minutes at room temperature to reduce mechanical tension within the layer of TiO_2 . For Ag@SiO_2 and Au@SiO_2 nanoparticles, the films were deposited using a liquid handling system (micropipette device), an electric heater was also prepared, and the temperature was set at 100 degrees to evaporate the solution and keep the nanoparticles stable (as mentioned earlier).

The dried Au@SiO_2 and Ag@SiO_2 films were sintered at 500 degrees Celsius to burn the organic components of the TiO_2 paste and increase the mechanical contact between the Ag@SiO_2 and Au@SiO_2 nanoparticles. After the TiO_2 and core-shell nanoparticles films had cooled to room temperature, they were immersed in a dye solution (N719, 0.25 mM) in a sealed box and stored in a dark place for 24 hours. FTO-glass plates were cut into 2.5 x 2 cm pieces for the counter electrode. Two holes were drilled into each piece using a 1mm drill in opposition corners of 1 x 1 cm square, and the drilling was done from the glass side to the FTO-glass side direction, as shown in figure (3.14). After the hole was drilled, the FTO glass was cleaned in an ultrasonic bath for 20 min (10 min deionized water, 10 min ethanol).

After washing, the platinum film was deposited on 1 x 1 cm squares of FTO glass using the doctor blade technique, as illustrated in Figure (4.15), and maintained at room temperature for 10 minutes to cool.



Figure 4.14. FTO-glass plates were cut into 2.5 x 2 cm pieces with two holes drilled into each piece

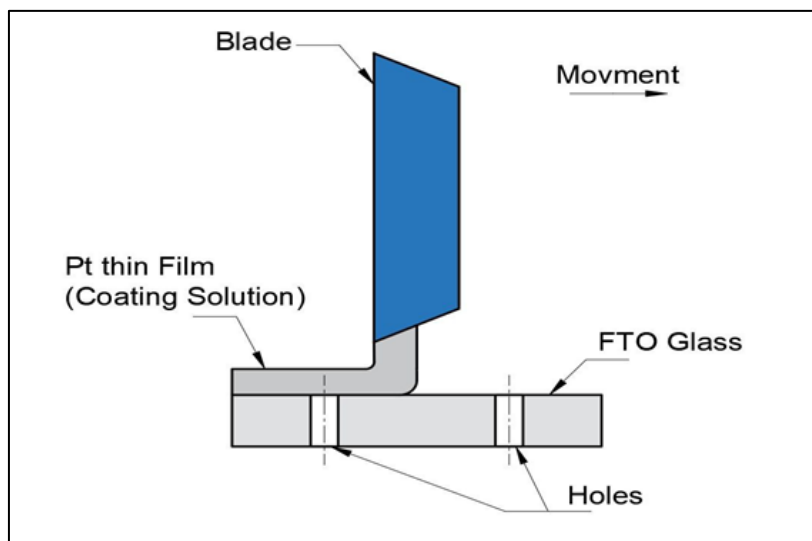


Figure 4.15. Doctor blade technique

Next, the platinum film was put in an oven at 500 °C, and after, we let it down to room temperature. Photoanode and counter electrode were next sealed using Thermoplastic Sealant (MS004610 30 μm Surlyn). Figure (4.16 a) shows how the gasket was put. Pressing the Thermoplastic Sealant gasket between the front and counter electrode for 15 minutes at 2.4 kN and 100 °C using a hot plate and 1 kilogram of iron metal with a 2 x 2 cm base yielded excellent results. Finally, a Pipette (10-100 l) is used to fill the counter electrode with electrolyte (EL-UHSE, Dyesol). After everything was finished, transparent adhesive tape was used to seal the hole in the counter electrode. Figure (4.16 b) displays the DSSc after it had been finished and was prepared for characterization.

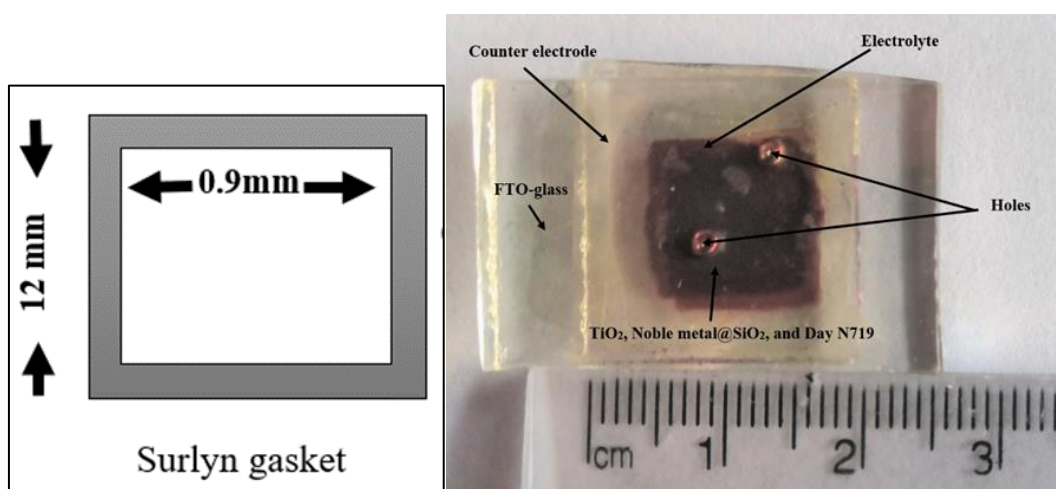


Figure 4.16. (a) Design of thermoplastic seal, and (b) a photograph of a dye sensitized solar Cell

4.6. Device and Sample Characterization

The final result from preparation (Laser ablation) and deposition processes was analyzed using multiple analysis tools to acquire a good view of nanostructures' structure, morphology, and optical properties. Additionally, the photovoltaic devices (PDSSCs) prepared from these products have been characterized to obtain the Solar cells parameters. The tools have been used to sample characterization listed below with brief descriptions.

4.6.1. Spectrophotometer

The UV-Visible Spectrophotometer UV-1900i UV-VIS Spectrophotometer from Shimadzu, with a wavelength range of (190 nm - 1100 nm) and the wavelength scan occurs at a rate of 3000 to 2 nm/min, 29000 nm/min when survey scanning, was used to measure the optical extinction spectra of the Au@SiO₂ and Ag@SiO₂ core-shell, nanoparticle solutions. All measurements were at room temperature. The data was sent from the Spectrophotometer to the desktop computer via an RS-232 cable.

4.6.2. Photoluminescence (PL)

The PL spectra were measured with Cary Eclipse Fluorescence Spectrophotometer (in the Daypetronic co., Iran) with a Xenon flash lamp (80 Hz). Au@SiO₂ and Ag@SiO₂ nanoparticles solutions have been characterized to distinguish the emission spectra when excited by a certain wavelength.

4.6.3 Optical Microscope

The optical microscope has been employed to examine the surface of the screen-printing method.

4.6.4. The analysis of X-ray diffraction (XRD)

X-ray diffraction (Shimadzu X-Ray Diffractometer XRD 6000 utilizing the Cu K α line 0.15419 nm) was used to characterize the Au@SiO₂ and Ag@SiO₂ films formed on a glass

substrate by a deposition method. The examination of samples was done in the laboratories of the University of Technology and the Photonic laboratory of Gazi University.

4.6.5. Transmission electron microscopy (TEM)

Transmission electron microscope (The Zeiss Leo 912 OMEGA is a 120 kV transmission electron microscope, along with its in-column OMEGA-energy filtering system and Koehler Illumination system for high picture contrast., in Daypetronic co., Iran) used to explore the shape and size of nanoparticles produced by laser ablation technique. These samples include Au@SiO₂ and Ag@SiO₂ core-shell.

4.7. The Dye-Sensitized Solar Cells (DSSCs) Characterization

In order to characterize DSSCs, many crucial parameters are used. These characteristics are all derived from the I-V curve: short-circuit current (I_{sc}), open-circuit voltage (V_{oc}), fill factor (FF), and efficiency (η). A typical laboratory method to characterize the current-voltage characteristics parameter analyzer for solar cells with a measurement port called a source measurement unit (SMU). To measure the current-voltage characteristics of a solar cell, an SMU is typically passed through various voltage limit levels, and the corresponding current is measured. Keithley's 2400 Series Source Meter instrument was used to test the three DSSCs in the photonic laboratory of Gazi university.



5. RESULTS AND DISCUSSIONS

In this chapter we review and discuss the results.

5.1. XRD analysis results

5.1.1. XRD analysis results for Ag@SiO₂ Nanoparticles prepared by Laser Ablation Technique

The crystallinity of the products and their chemical makeup can be determined by using powder XRD analysis, as shown in figure (5.1). According to the Crystallography open database (COD) 9006286, the powder XRD pattern of SiO₂ demonstrates a high and broad presence of the reflection peak at 28.5272 degrees, which indicates that SiO₂ has an amorphous structure. The reflection peak at 38.1891°, 44.3895° for 50 mJ, 38.1747°, 44.3638 for 100mJ, 38.1591°, and 44.3570° for 150mJ caused by crystal planes (111), (200). All the reflected Peaks (111) and (200) point out the FCC phase of silver nanoparticles (Crystallography open database (COD) 9012431). The peak broadening in the XRD pattern, without any doubt, indicates that small nanocrystals (Ag NPs) exist in the samples.

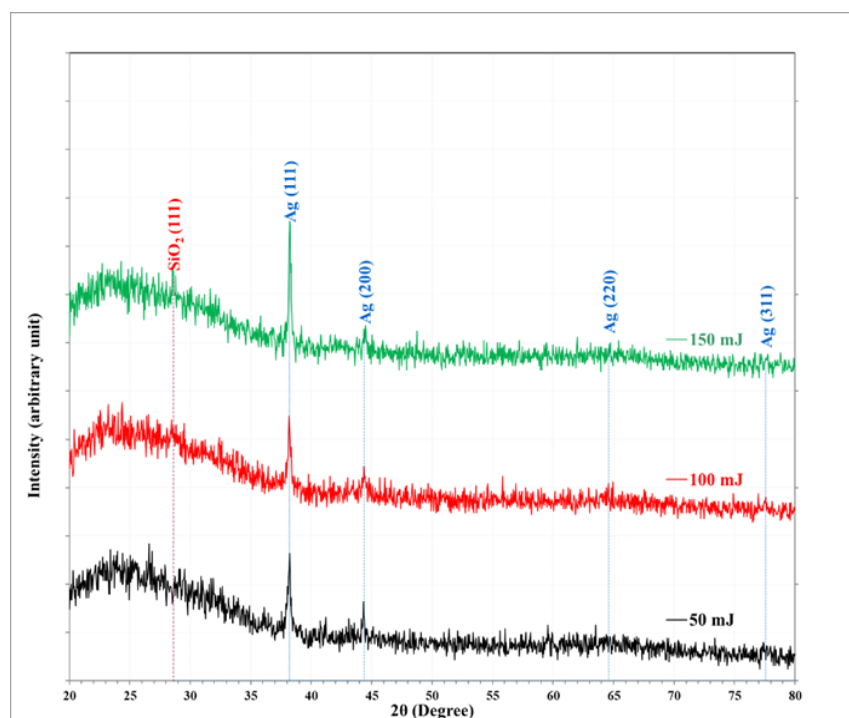


Figure 5.1. XRD pattern of nanoparticles Ag@SiO₂ core shell prepared using laser ablation technique (— 50 mJ, — 100 mJ, and — 150 mJ)

The lattice constants $a=b=c=4.0785\text{\AA}$, 4.0800\AA , and 4.0816\AA for laser energies of 50, 100, and 150 mJ were calculated from the XRD data using Bragg's equation (3.18). It appears that the SiO₂ shell's successful coating of the Ag NPs' surface is what is responsible for the decrease in the intensity of the reflection planes of Ag. It appears that the SiO₂ shell's effective coating of the Ag NPs' surface is what causes the decrease in the intensity of the reflection planes of Ag. Additionally, judging by the appearance of strong diffraction peaks, the crystallinity of Ag NPs is not impacted by the SiO₂ covering. The interplanar spacing (d_{hkl}) obtained from XRD results is compared with the COD data card (Crystallography open database (COD) 9012431) and matching (h k l) planes; table (5.1) summarizes the XRD results.

Table 5.1. Summarizes the results of the XRD measurement for Ag@SiO₂.

Laser energy (mJ)	2 θ (Deg.)	FWHM (Deg.)	d_{hkl} Exp.(\AA)	D (nm)	d_{hkl} Std.(\AA)	Phase	hkl
50	38.1891	0.4470	2.3547	18.8	2.3543	Cub. Ag	(111)
	44.3895	0.4813	2.0391	17.8	2.0389	Cub. Ag	(200)
100	38.1747	0.3438	2.3556	24.5	2.3543	Cub. Ag	(111)
	44.3638	0.3439	2.0403	24.9	2.0389	Cub. Ag	(200)
150	28.5272	0.4470	3.1264	18.3	2.3543	Orth.SiO ₂	(111)
	38.1591	0.2407	2.3565	34.9	2.3543	Cub. Ag	(111)
	44.3570	0.3094	2.0406	27.7	2.0389	Cub. Ag	(200)

The crystallite size of silver nanoparticles was estimated with the help of the Scherrer formula equation (3.19). The contribution of the microstrain to the line broadening of the diffraction peak is defined by Stokes and Wilson equation (3.22) [166]. Table (5.2) shows the results of some XRD calculations for the (111) plane.

Table 5.2. Summarizes the results of some XRD calculations for the (111) plane of Ag@SiO₂.

Laser energy (mJ)	a (\AA)	C.S (nm)	microstrain
50	4.0785	18.8	0.0018
100	4.0800	24.5	0.0014
150	4.0816	34.9	0.0010

The crystallite size as a function of laser energy for Ag@SiO₂ NPs shown in Figure (5.2) shows that when the laser energy increases, the crystallite size increases [177].

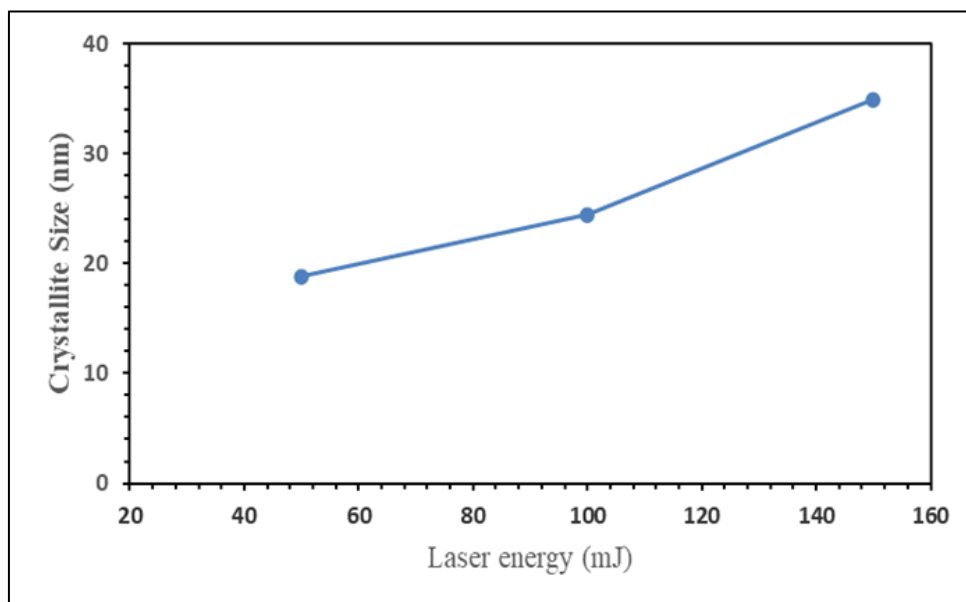


Figure 5.2. Crystallite size verse laser energy for Ag@SiO₂ NPs

5.1.2. XRD analysis results for Au@SiO₂ Nanoparticles prepared by Laser Ablation Technique

Crystallinity and chemical content of the products are determined by powder XRD analysis, as shown in Figure (5.3).

The powder XRD pattern of SiO₂ is broad and strong, Reflection peak at 28.5307° indicating the amorphous structure of SiO₂ according to Crystallography open database (COD) 9006286.

The reflection peak at 38.2347° for 50 mJ, 38.2664° for 100mJ, and 38.2030° for 150mJ caused by crystal planes (111). All the reflected Peaks (111) point out the FCC phase of gold nanoparticles (Crystallography open database (COD) 9012953).

The peak broadening in the XRD pattern, without any doubt, indicates that small nanocrystals (Au NPs) exist in the samples.

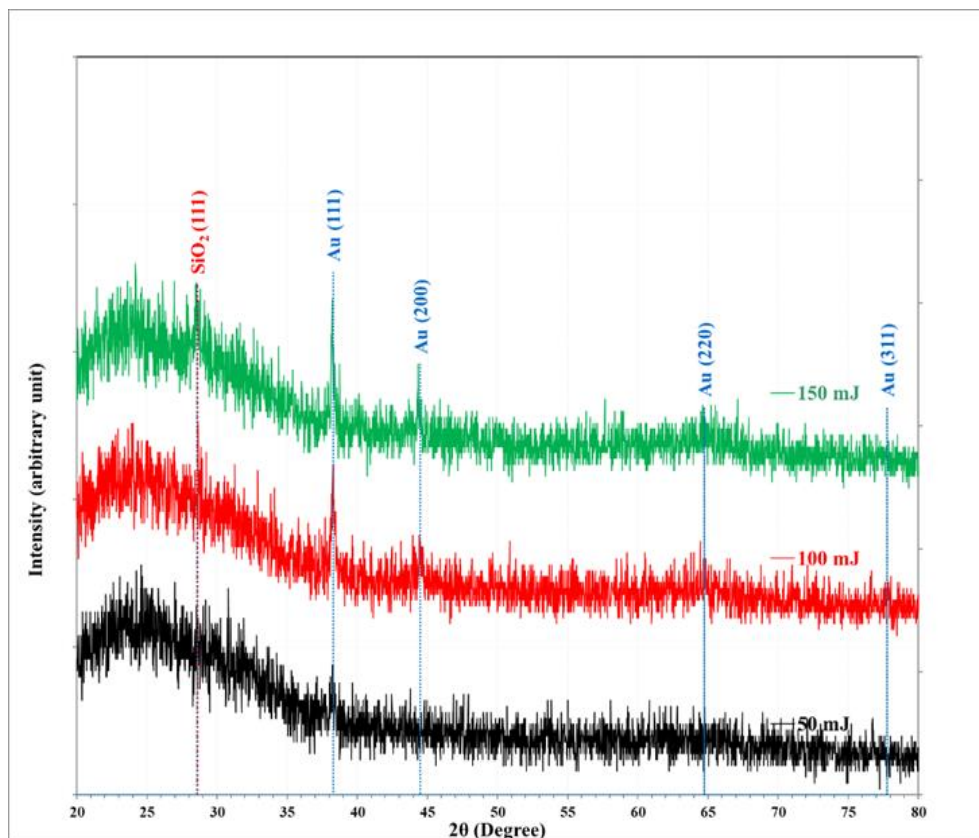


Figure 5.3. XRD pattern of Au@SiO₂ core-shell nanoparticles prepared by laser ablation technique (— 50 mJ, — 100 mJ, and — 150 mJ)

The interplanar spacing (d_{hkl}) obtained from XRD results is compared with the COD data card (Crystallography open database (COD) 9012953 for Au and 9006286 for SiO₂) and matching (h k l) planes; table (5.3) showing XRD results.

Table 5.3. Results for XRD measurement for Au@SiO₂.

Laser energy (mJ)	2θ (Deg.)	FWHM (Deg.)	d_{hkl} Exp.(Å)	D (nm)	d_{hkl} Std.(Å)	Phase	hkl
50	38.2347	0.6660	2.3520	12.6	2.3543	Cub. Au	(111)
100	38.2664	0.3800	2.3502	22.1	2.3543	Cub. Au	(111)
	44.5137	0.4430	2.0337	19.4	2.0389	Cub. Au	(200)
150	28.5307	0.5074	3.1261	16.2	2.3543	Orth.SiO ₂	(111)
	38.2030	0.3100	2.3539	27.1	2.3543	Cub. Au	(111)
	44.3552	0.2537	2.0406	33.8	2.0389	Cub. Au	(200)

The crystallite size of silver nanoparticles was estimated with the help of the Scherrer formula equation (3.19). The contribution of the microstrain to the line broadening of the diffraction peak is defined by Stokes and Wilson equation (3.22) [166].

Table 5.4. Shows the results of some XRD calculations for the (111) plane of Au@SiO₂

Laser energy (mJ)	a (Å)	D (nm)	Microstrain
50	4.07384	12.6	0.0027
100	4.07059	22.1	0.0016
150	4.07709	27.1	0.0013

The crystallite size as a function of laser energy for Au@SiO₂ NPs shown in Figure (5.4) is apparent that when the laser energy increases, the crystallite size increase [178,179].

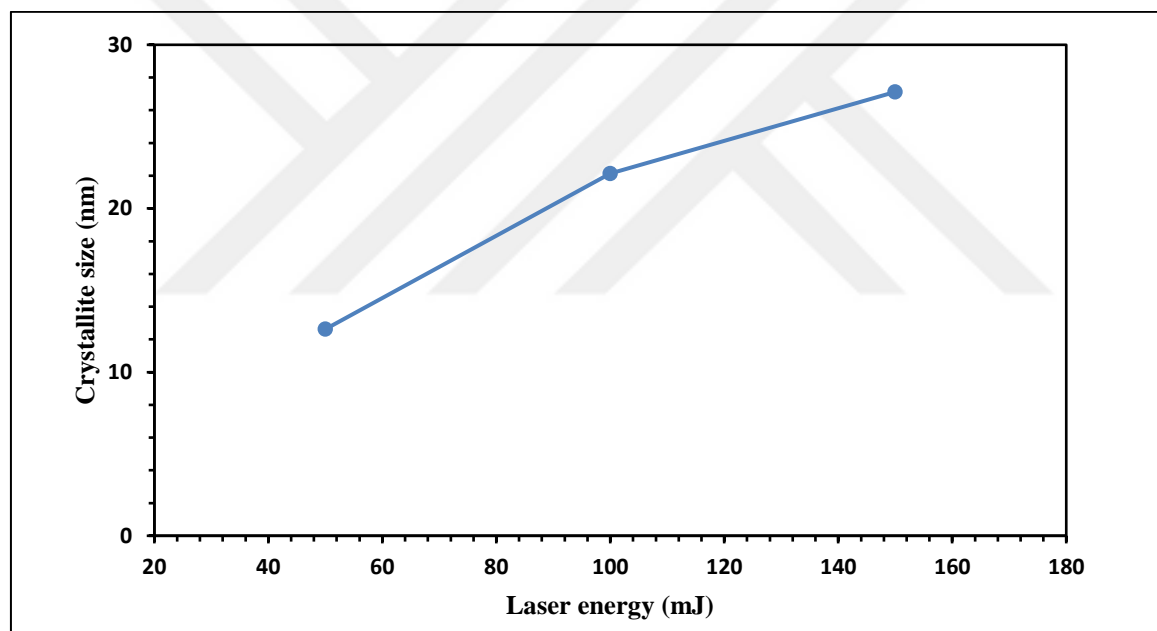


Figure 5.4. Crystallite size versus laser energy for Au@SiO₂ NPs

Through the results of the XRD for gold and silver, we noticed that when we increased the laser pulse energy, the crystal size for the nanoparticle increased, and these results agree with the results of previous researchers [180].

5.2. Optical Properties Results

5.2.1. Optical properties of Ag@SiO₂ nanoparticles

Absorption spectra of Ag@SiO₂ nanoparticles samples generated by pulsed laser ablation at varying pulse laser energy are displayed in Figure (5.5). Depending on the size of the particle, shape, aggregation state, and surrounding dielectric medium of the SPR cause a red or blue shift in the optical absorption spectra of metal nanoparticles [179,181]. The visible light absorption band is typical nanoparticles of Ag. The degree of nanoparticle aggregation influences the plasmon peak and full width at half maximum. By increasing the pulse laser ablation energy from 50 to 150 mJ, we see a change in the SPR wavelength toward a more extended wavelength area (Fig. 5.5), indicative of a larger particle size. It is also clear from the absorption spectra that the peak broadens increases as the pulse laser intensity increases [179,181,182].

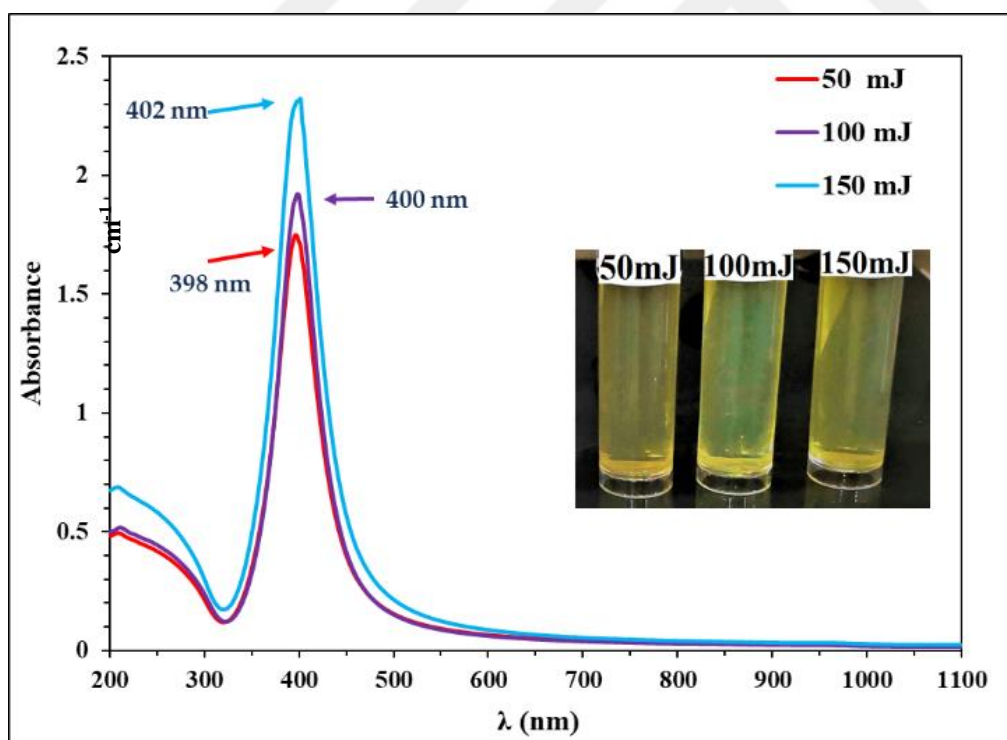


Figure 5.5. Absorbance relates to the wavelength of Ag@SiO₂ core-shell nanoparticles for different laser energies. The inset shows the images of Ag@SiO₂ samples

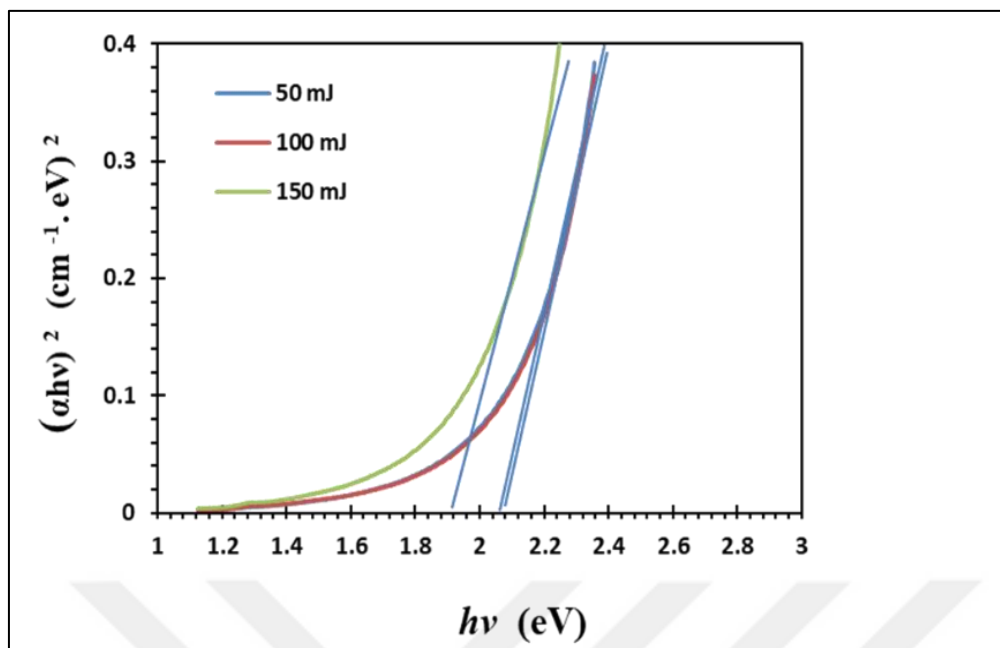


Figure 5.6. Optical energy bandgap for Ag@SiO₂ nanoparticles core-shell prepared at different laser energies.

The plot of $(\alpha h\nu)^2$ against $h\nu$ for Ag@SiO₂ core-shell NPs can be seen in Figure 4. In this figure, h refers to the constant of Planck's, α refers to the coefficient of absorption, and ν refers to the incident light frequency. The energy gap of Ag@SiO₂ core shell NPs has been determined by extending the linear section of $(\alpha h\nu)^2$ to intersect with the $h\nu$ -axis.

It was done to determine the energy gap. When calculating the optical energy gap of the NPs, a well-known relation for direct transition (Eq 3.26) is used. The value of E_g was calculated using the extrapolation approach, and it was found to be 1.94, 2.06, 2.08 eV for laser energies of 50, 100, and 150 mJ, respectively [183-185].

Time-resolved PL spectra and PL excitation measurements are also taken to analyze the PL spectra of better NPs of the Ag@SiO₂ core shell. Ag's visible luminescence is caused by the excitation of electrons from occupied d bands into states above the Fermi level.

An energy loss results from the process of Subsequencelectron-phenomenon and hole-phonon scattering, and then an electron from an occupied sp band combines with a hole to produce photoluminescence [186,187]. Figure (5.7) depicts the luminescence spectra of the core-shell Ag@SiO₂ with various pulse laser energies. With increased laser energy, it has been seen that PL increases.

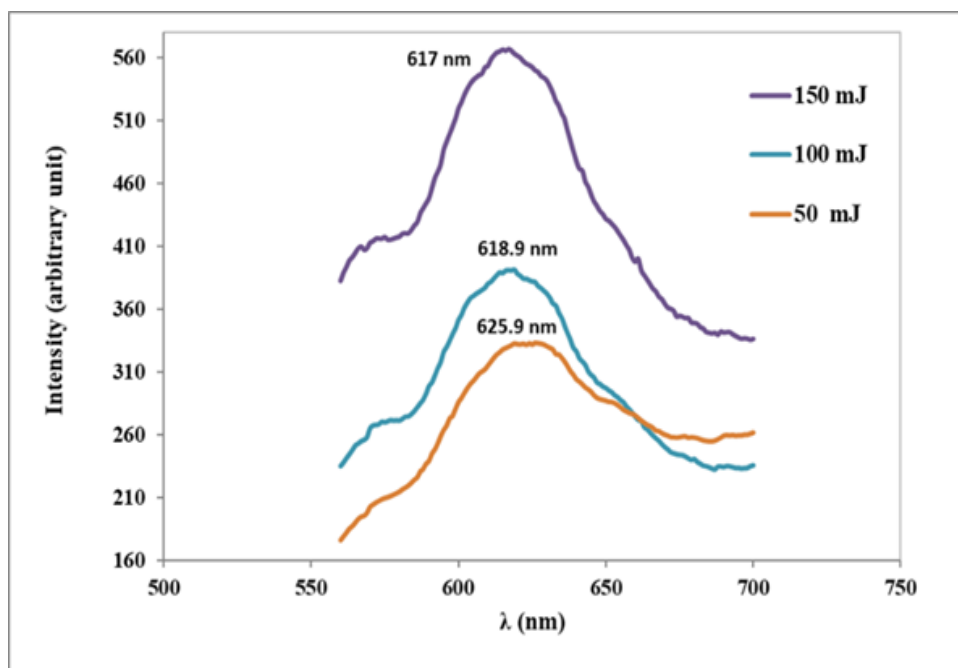


Figure 5.7. The photoluminescence (PL) spectra of Ag@SiO₂ core-shell NPs at various laser Powers

We use Planck's equation (3.27) to determine the energy bandgap from photoluminescence spectra of Ag@SiO₂ core-shell NPs.

The comparison between energy gap values calculated from UV-vis and PL measurements was tabulated in table (5.5). The optical power gap computed from the two measures is close in value.

Table 5.5. Summarizes the results of the energy gap values estimated from the UV-Vis and PL measurements

Laser energy (mJ)	Eg, from UV-Vis (eV)	Eg, from PL (eV)
50	2.06	1.98
100	2.08	2
150	1.94	2

5.2.2. Optical characterization for Au@SiO₂ nanoparticles

Absorption spectra of Au@SiO₂ nanoparticles samples generated by pulsed laser ablation at varying pulse laser energy are displayed in Figure 5.8. Depending on the insulating medium,

ambient, state of aggregation, shape, and particle size, the SPR causes a red or blue shift for the absorption optical spectra of metal nanoparticles [188].

The visible light absorption band is typical for Au nanoparticles. The degree of nanoparticle aggregation influences the plasmon peak and full width at half maximum. By increasing the pulse laser ablation energy from 50 to 150 mJ, we see a change in the SPR wavelength toward a more extended wavelength area Fig(5.8), indicative of a larger particle size. It is also clear from the absorption spectra that the peak broadens increases as the pulse laser intensity increases [188,189].

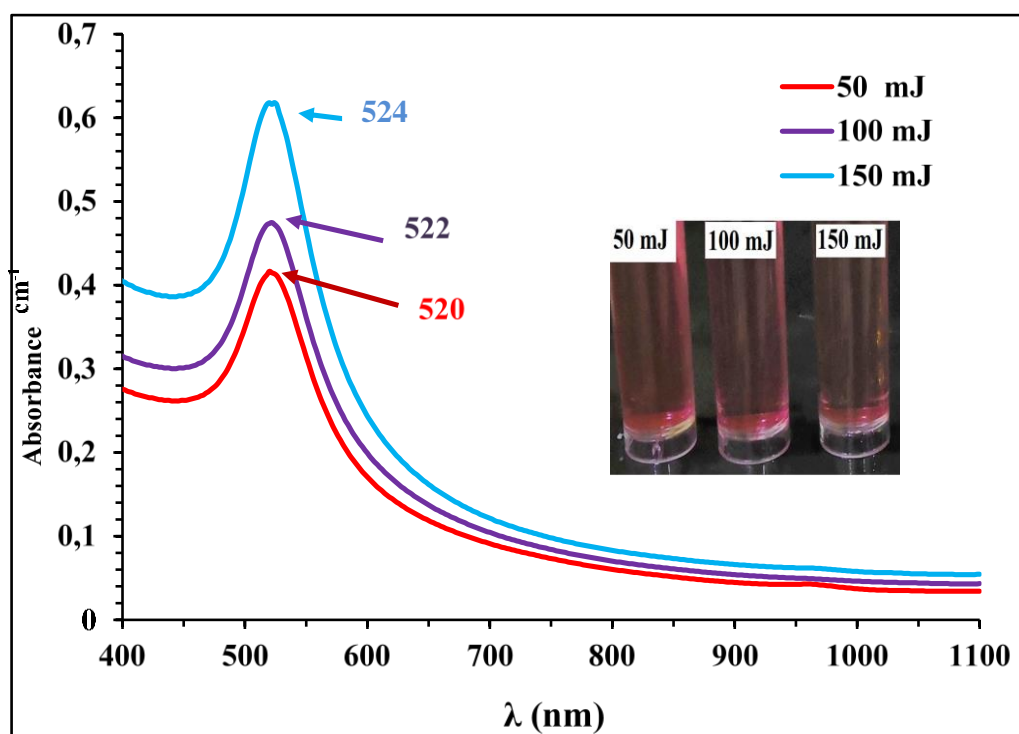


Figure 5.8. Absorbance relates to the wavelength of Au@SiO₂ core-shell nanoparticles for different laser energies. The inset shows the images of Au@SiO₂ samples

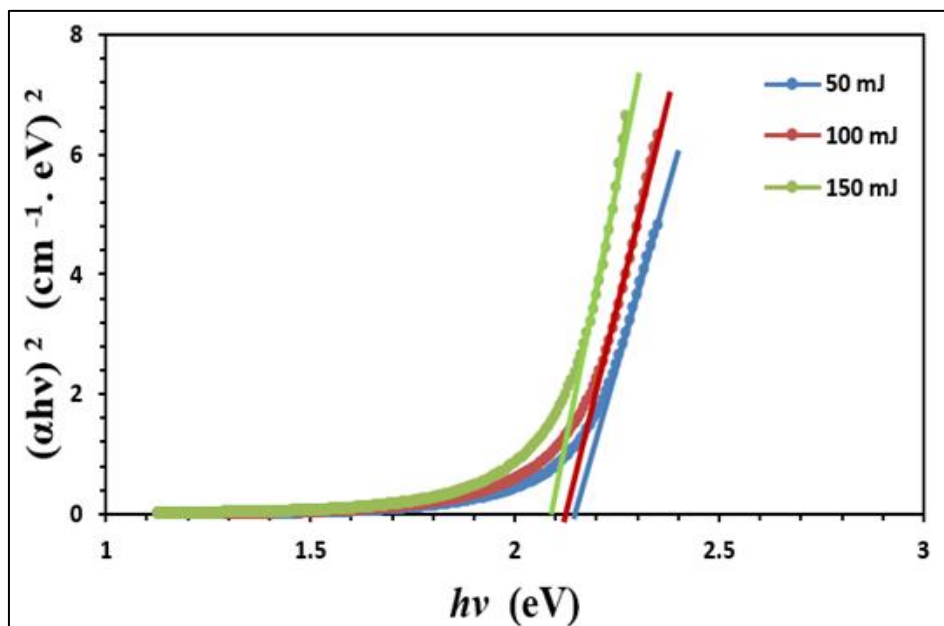


Figure 5.9. Optical energy bandgap for Au@SiO₂ nanoparticles core-shell prepared at different laser energies.

Figure (5.9) depicts the plot of $(\alpha h\nu)^2$ versus $h\nu$ for Au@SiO₂ core-shell NPs. In this diagram, h refers to Planck constant, α refers to the coefficient of absorption, and ν refers to the frequency of incident light. We determined the energy gap of Au@SiO₂ core-shell NPs by extending the linear section of $(\alpha h\nu)^2$ to intersect with the $h\nu$ axis. The objective was to determine the energy gap. In order to calculate the optical energy gap of the NPs, a well-known relation for direct transition (equation 3.26) is applied. Using the extrapolation method, the value of E_g was determined to be 2.09, 2.11, and 2.13 eV for laser energies of 50, 100, and 150 mJ, respectively [190-193].

Time-resolved PL spectra and PL excitation measurements are also taken to analyze the PL spectra of Au@SiO₂ core-shell better NPs. Au's visible luminescence is caused by the excitation of electrons from occupied d-band states into levels above the Fermi level.

An energy loss is caused by the sequential electron phenomenon and hole-phonon scattering, and photoluminescence is then produced when an electron from an occupied sp band interacts with a hole.

Figure (5.10) depicts the luminescence spectra of the core-shell Au@SiO₂ with various pulse laser energies. With increased laser energy, it has been seen that PL increases.

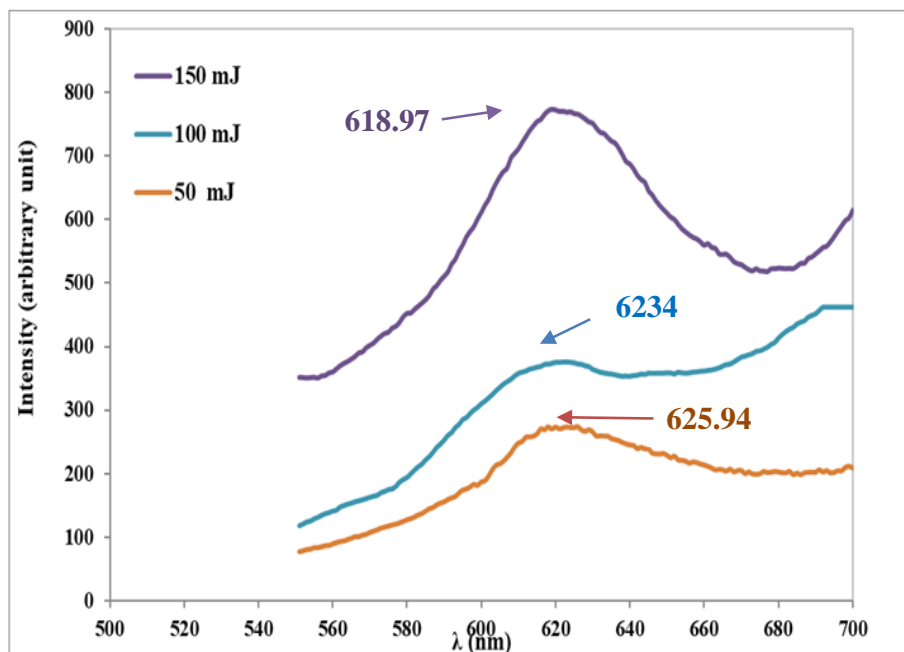


Figure 5.10. The photoluminescence (PL) spectra of Au@SiO₂ core-shell NPs at various laser powers

We use Planck's equation (3.27), which tells us the energy bandgap of Au@SiO₂ core-shell NPs, to find the energy bandgap. Table (5.6) compares UV-vis and PL band gap values. The optical band gap that was calculated is close.

Table 5.6. Results of the energy gap values estimated from the UV-Vis and PL measurements

Laser energy (mJ)	E _g from UV-Vis (eV)	E _g from PL(eV)
50	2.13	1.98
100	2.11	1.99
150	2.09	2.0

We note from the results that the energy gap in Ag@SiO₂ and Au@SiO₂ decreases with the energy increases due to the increase in nanoparticles size, and this is what we will notice in the results of TEM pictures in part 5.3, and This agrees with the results of previous researchers [194].

5.3. Transmission Electron Microscope (TEM)

5.3.1. TEM for Ag@SiO₂

Figure (5.11) shows the TEM image Ag@SiO₂ prepared with laser ablation with (100.000 kX) magnification, the energy of the laser beam is varied from 50 to 150 mJ and the solution thickness above the silver target is (0.8 cm). The image shows that Ag@SiO₂ core-shell nanoparticles form a sphere, and the size distribution of these particles can be seen in the size distribution chart.

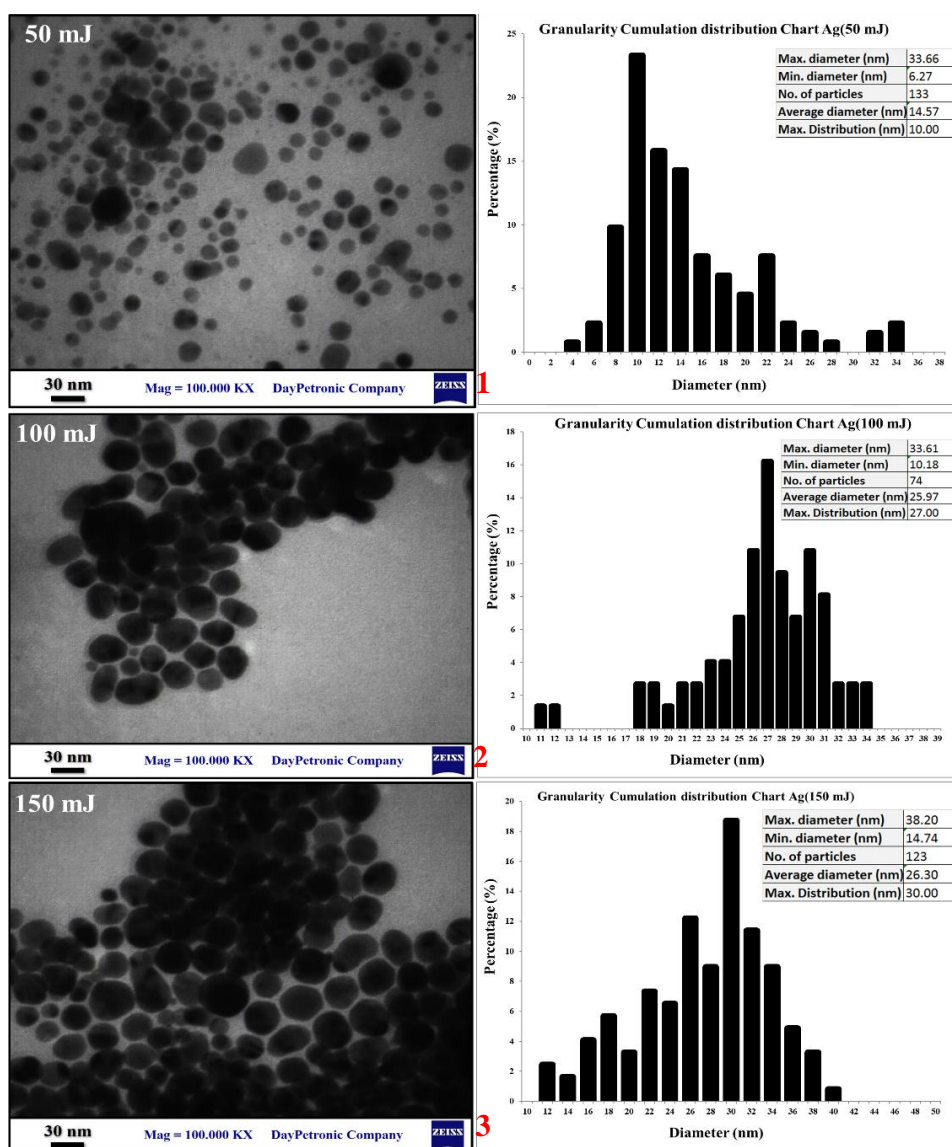


Figure 5.11. Transmission electron micrograph (TEM) and size distribution chart of laser-ablated Ag@SiO₂ core-shell NPs synthesis at (1) 50, (2)100, and (3)150 mJ

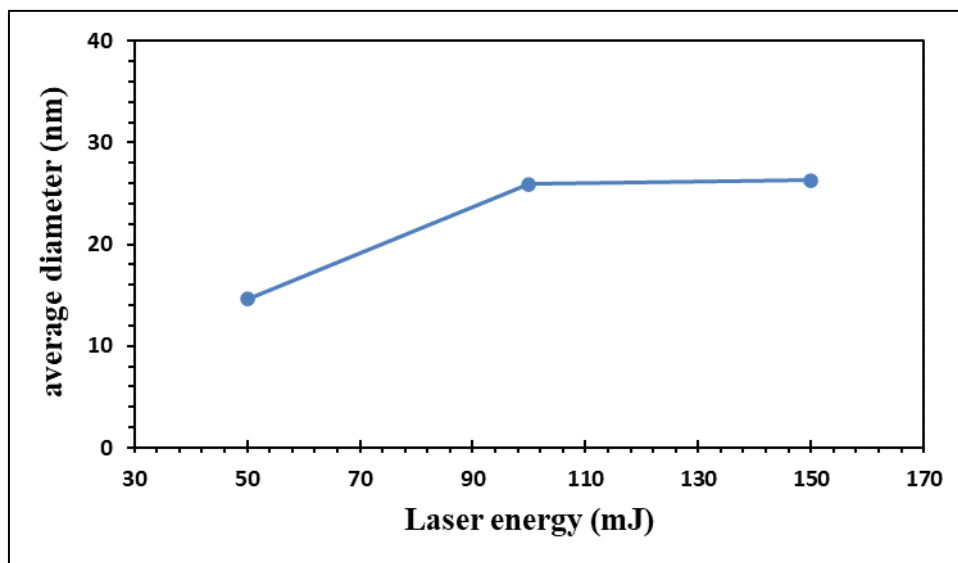


Figure 5.12. Average diameter against laser energy for Ag@SiO₂

As shown in Figure (5.12), when the pulse laser energy was raised from 50 to 100 mJ, the average particle size rose significantly more than when the energy of laser increased (100 to 150 mJ) [195].

The transmission electron micrograph (TEM) picture of several Ag@SiO₂ can be shown in Figure (5.13). The 5 nm SiO₂ shell can be seen clearly around the silver NP core in this image.

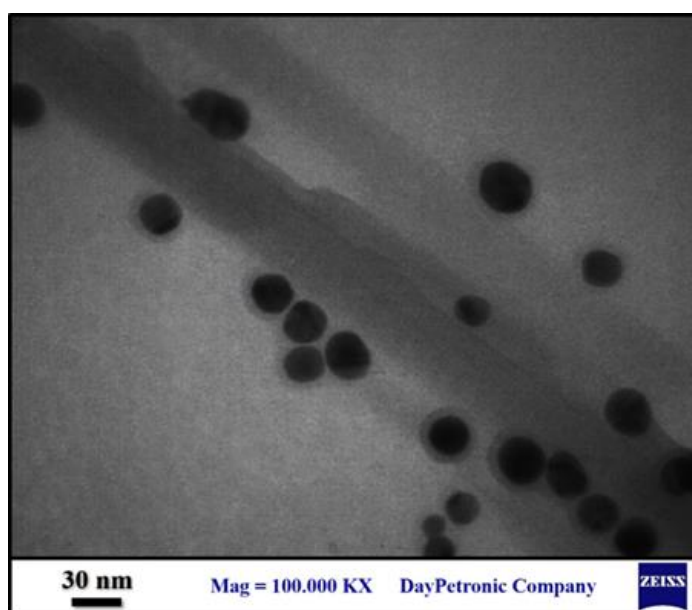


Figure 5.13. TEM picture of Ag@SiO₂, which distinctly shows the presence of SiO₂ Nano Shell

5.3.2. TEM for Au@SiO₂

Figure (5.14) demonstrates the TEM image of Au@SiO₂ prepared by laser ablation at a magnification of 1,000,000 kX, where the laser beam energy varies from 50 to 150 mJ, and the solution thickness above the silver target is (0.8 cm). The image depicts Au@SiO₂ core-shell nanoparticles as spherical particles, and the size distribution of these particles can be seen in the size distribution chart.

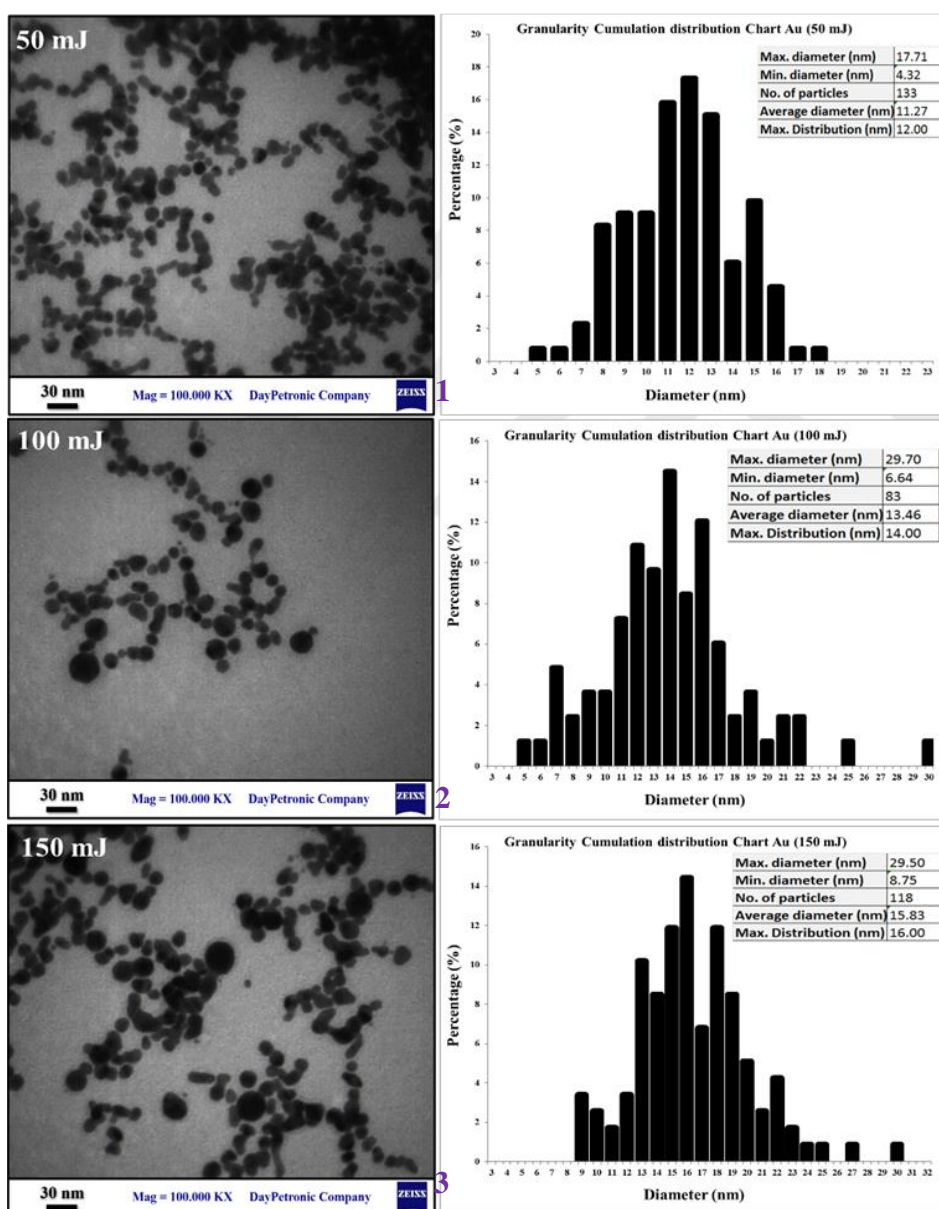


Figure 5.14. Transmission electron micrograph (TEM) and size distribution chart of laser-ablated Au@SiO₂ core-shell nanoparticles synthesis at 50, 100, and 150 mJ

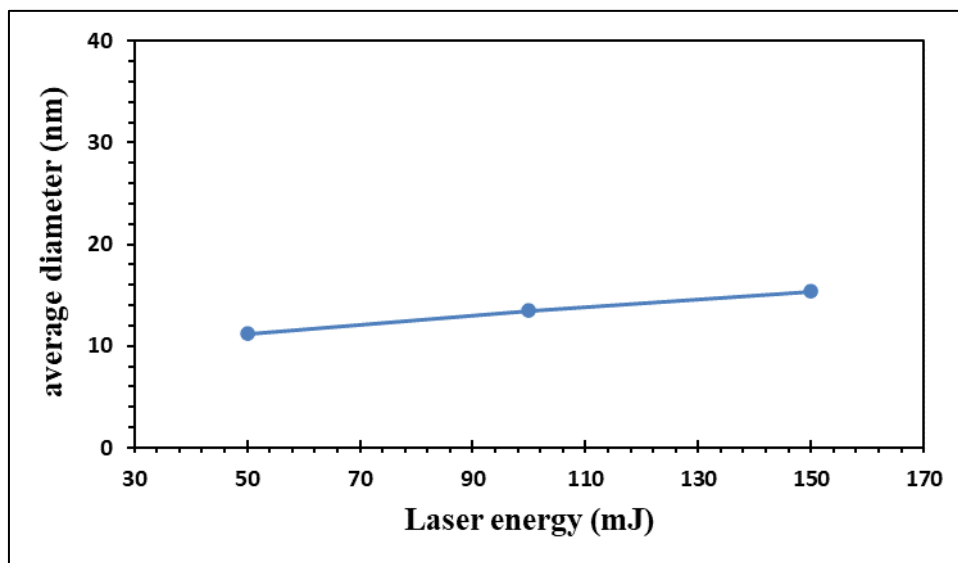


Figure 5.15. Average diameter against laser energy for Au@SiO₂

Figure (5.15) shows that when the pulse laser energy was raised from 50 to 100 mJ, the average particle size rose a little more than when the laser energy was raised from 100 to 150 mJ [196].

Figure 5.14 shows a transmission electron micrograph (TEM) picture of several Au@SiO₂. The 6.1 nm SiO₂ shell can be seen clearly around the silver NP core in this picture.

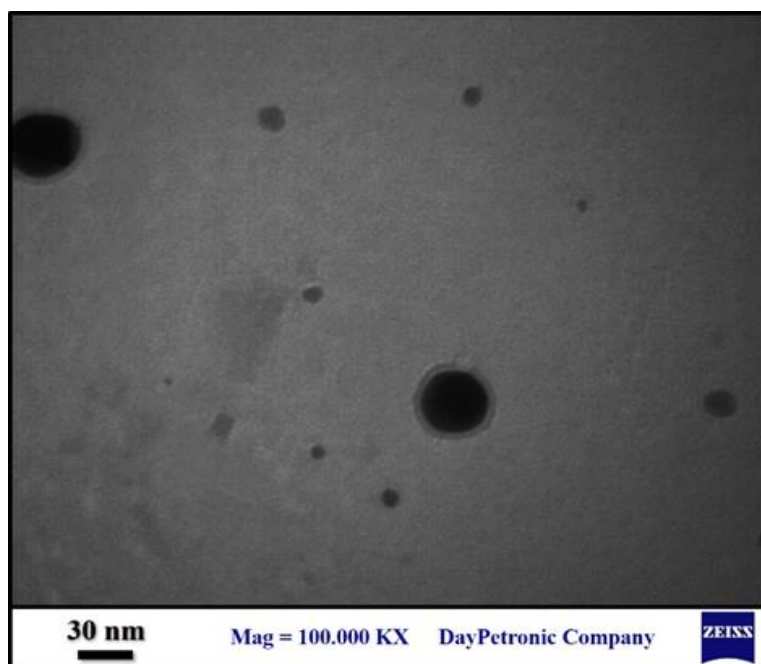


Figure 5.14. TEM picture of Au@SiO₂, which distinctly shows the presence of SiO₂ Nano shell

5.4. Plasmon Dye-Sensitized Solar Cell (PDSSC) Results

characteristics of current-voltage (I-V) for the fabricated dye synthesized solar cell (DSSC) compared with that loaded cells with the Ag@SiO₂ and Au@SiO₂ NPs, at dark and under illumination conditions (light intensity=100 mW/cm²) were shown in Figure (5.15). It can be seen that the open circuit voltage value increased when used both types of nanoparticles were, and the short circuit current increased, especially with the use of gold nanoparticles. The improvement in dye loading and the advantageous injection of hot electrons caused by the surface plasmon resonance (SPR) effect may be responsible for the increase in photocurrent [197].

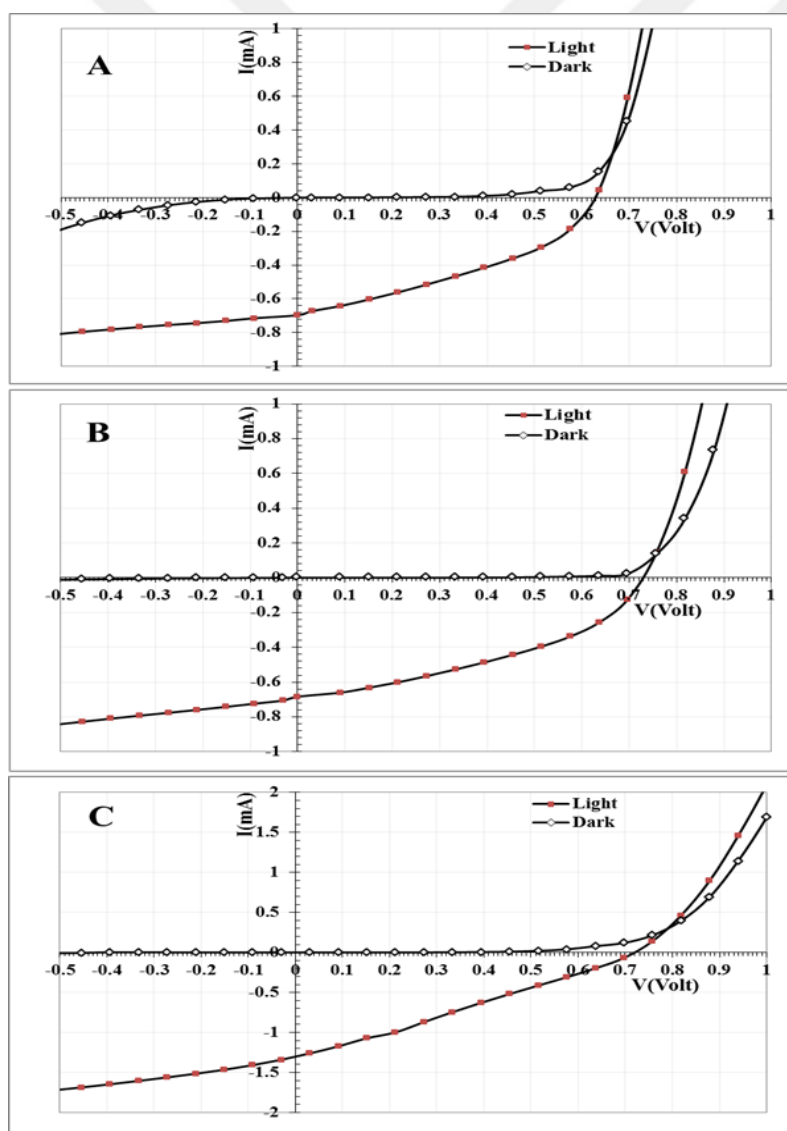


Figure 5.15. (A) I-V characteristics at dark and under illumination for the fabricated DSSC, (B) DSSC loaded with the Ag@SiO₂, (c) Au@SiO₂ loaded

The shunt and series resistance of the prepared solar cells were determined by inverting the slope of the I-V curve under illumination at its cross with the Y-axis and X-axis, respectively.

The maximum power point was determined by plotting the power against voltage (P-V), as shown in Figure (5.16). The maximum points for the DSSC, and that loaded with the Ag@SiO₂ and with Au@SiO₂ NPs, were 0.164, 0.203, and 0.249 mW at 0.394, 0.515, and 0.334 V, respectively.

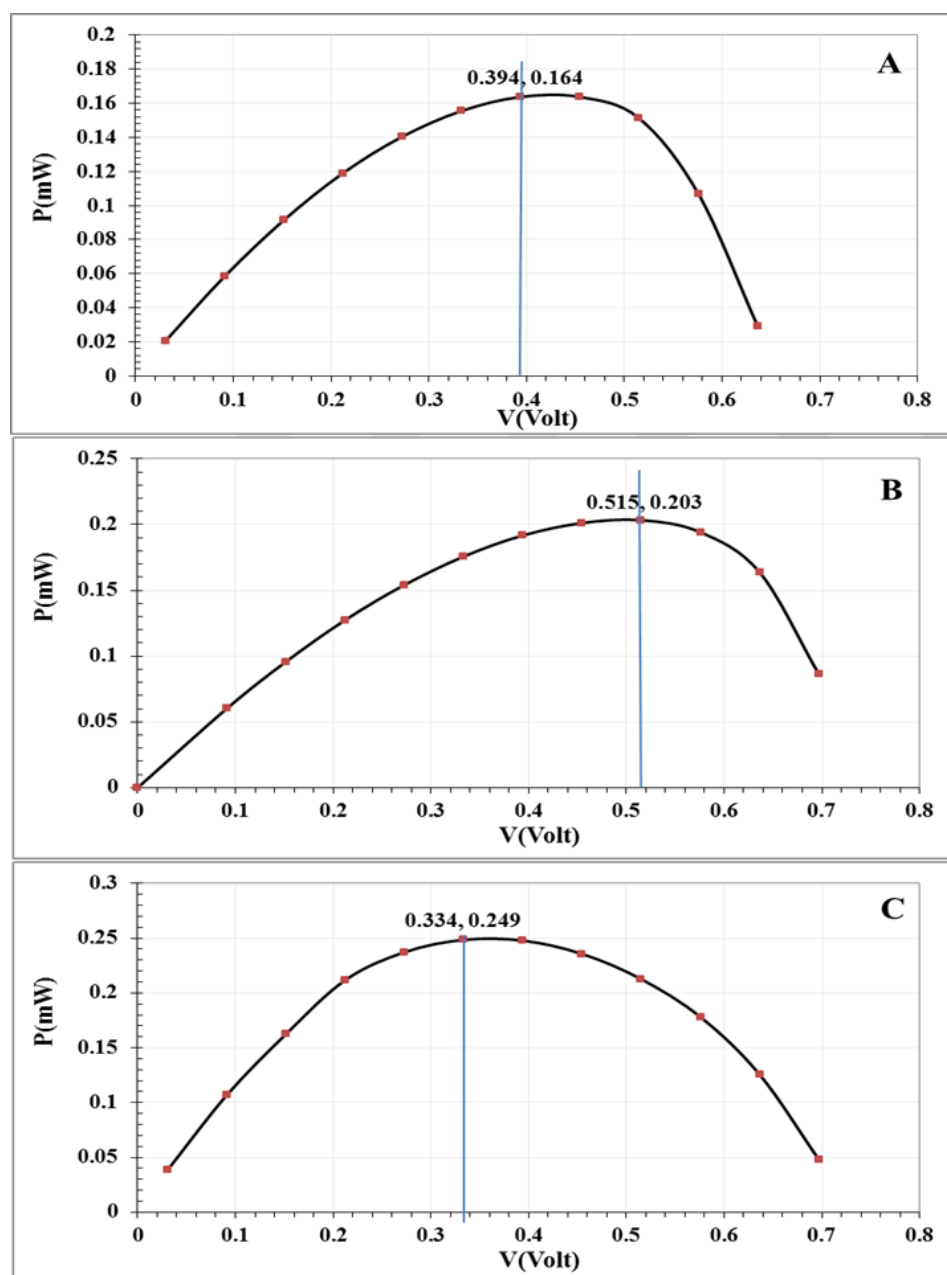


Figure 5.16. P-V characteristics under illumination for the fabricated DSSC (A), DSSC loaded with Ag@SiO₂ (B) and with Au@SiO₂ (c).

The fill factor (FF) and maximum conversion efficiency (η_{\max}) of the fabricated DSSC are calculated by equation (3.1).

When I_m , V_m , I_{sc} , and V_{oc} show the current and voltage at their highest possible levels when power is maximum, short current circuit, and open circuit voltage. The P_m is the maximum power, and the P_{in} is the input power from the solar radiation (the light intensity multiplies the effective area). Figure (5.17) shows the variation of the logarithm of the absolute value of current with V .

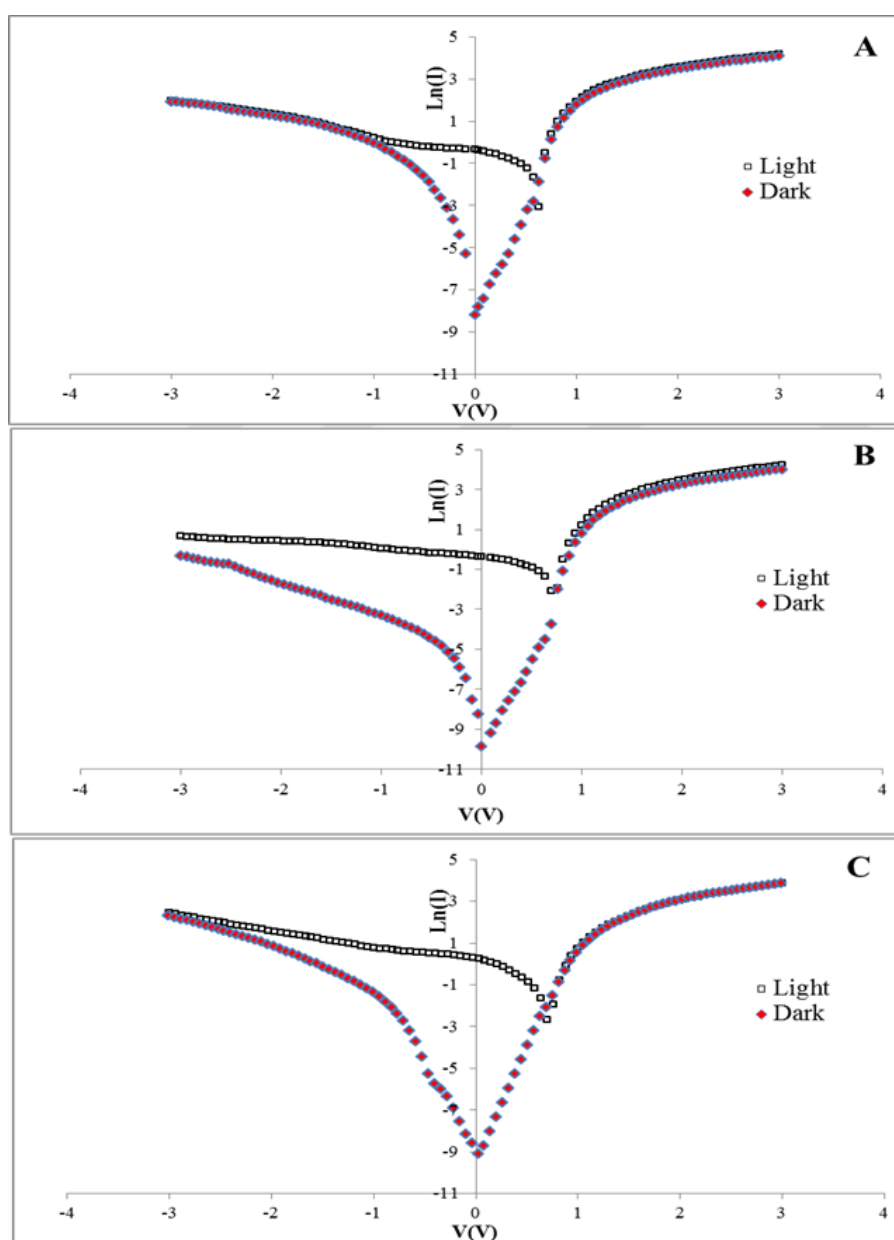


Figure 5.17. $\ln(I)$ versus V at dark and under illumination for the fabricated DSSC (A), DSSC loaded with Ag@SiO_2 (B) and with Au@SiO_2 (C)

Figure (5.18) displays the linear parts for $\ln(I)$ versus V of forward current at the dark condition for the three solar cells within the two regions. The slope of the first region was employed to determine the non-ideality factor (β).

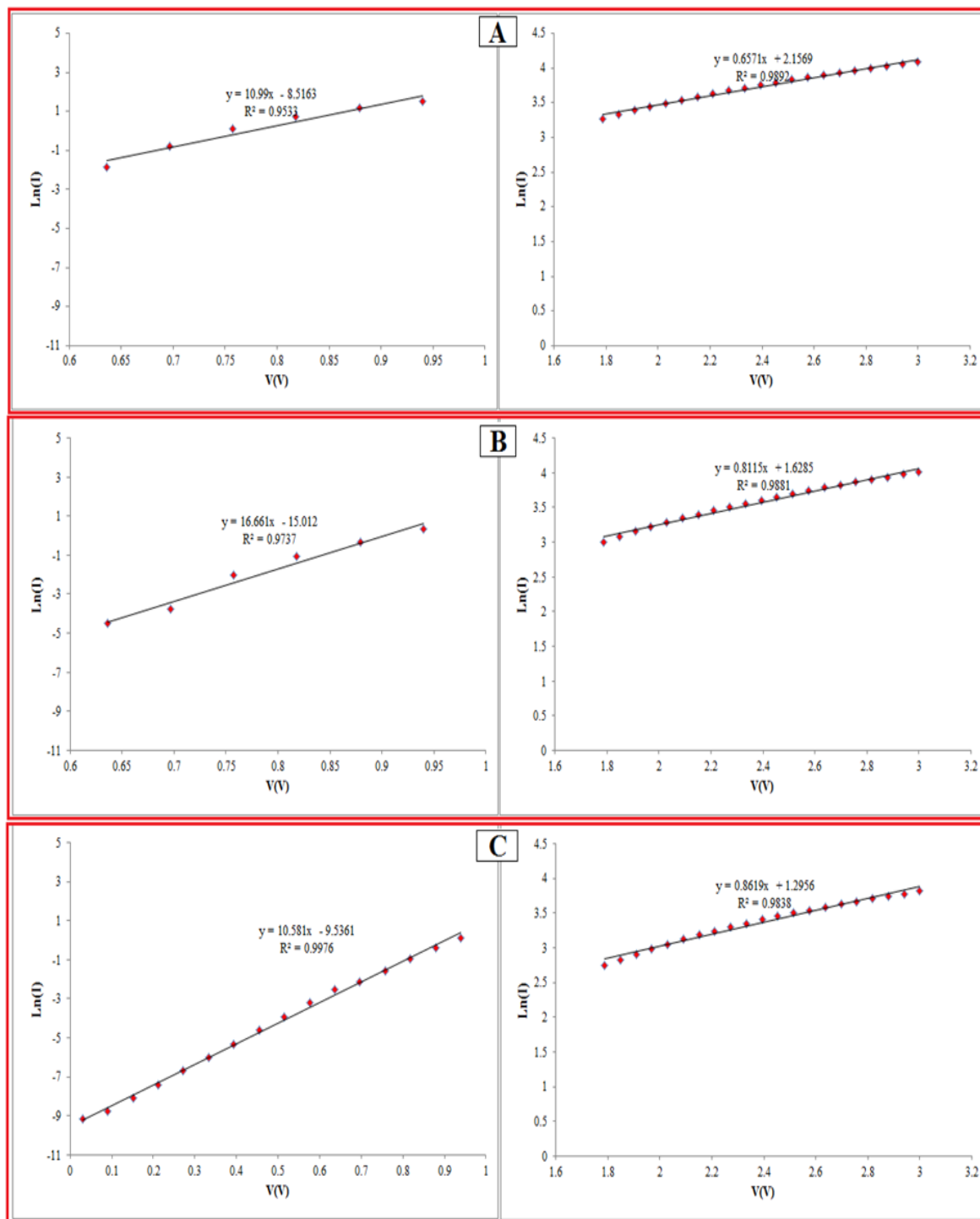


Figure 5.18. $\ln(I)$ versus V for the dark condition at the two regions for the fabricated DSSC (A), DSSC loaded with Ag@SiO₂ (B) and with Au@SiO₂ (C)

Table (5.7) provides a summary of the photovoltaic parameters for these cells, including open-circuit voltage (V_{oc}), short-circuit current (J_{sc}), fill factor (FF), solar efficiency (η), non-ideality factor (β), shunt resistance (R_{sh}), and series resistance (R_s). All samples exhibit a photovoltaic effect. The controlled DSSC with no metal NPs showed an efficiency of 0.18%, and it increased up to 0.23% with the incorporation of the $Ag@SiO_2$ and to 0.27% with the $Au@SiO_2$ NPs (b). Such an increase is attributed to enhancing the sample absorbance by the device as a result of the scattering effect of the nanoparticles at plasmonic wavelength [198,199], the plasmon peak located nearly at the maximum of the solar spectrum. Despite the low efficiency of the synthesized cells, it is considered a good result compared to previous research due to its low cost. However, we found that by adding the nanoparticles, the near field around the nanoparticles would improve light harvesting [200]. The incorporation of the NPs can also facilitate charge separation in photoanode. The accumulated charge into the NPs cause more negative for the Fermi level of metal/semiconductor. So, open-circuit voltage clearly rises from 0.63 mV in control DSSC to 0.74 and 0.73 mV with $Ag@SiO_2$ and $Au@SiO_2$ NPs due to Fermi-level shift [201].

Table 5.7. The characteristics parameters for the fabricated DSSC loaded with the $Ag@SiO_2$ and $Au@SiO_2$

<i>Parameter</i>	<i>Control</i>	<i>with $Ag@SiO_2$</i>	<i>with $Au@SiO_2$</i>
I_{sc} (mA)	0.68	0.70	1.30
V_{oc} (V)	0.63	0.74	0.73
I_m (mA)	0.42	0.39	0.75
V_m (v)	0.39	0.52	0.33
$F.F$	0.39	0.39	0.26
$\eta\%$	0.18	0.23	0.27
R_{sh} (Ω)	2300.8	2711.0	769.9
R_s (Ω)	187.0	197.4	266.5
β	3.64	2.40	3.78

5.5. Conclusion

To meet the increasing demand for energy with renewable and clean sources of the rising long-term climate deterioration. Solar cells as a viable renewable energy source are the efficiency and cost improvements to these components. The dye solar cell (DSSC) is one of the most cost-effective devices for creating electrons from solar photovoltaic energy and has

a lower production cost than competing technologies. Despite its low efficiency, it is still under development to reach high efficiency using several methods.

In this thesis

1. We have successfully prepared Au@SiO₂ and Ag@SiO₂ core-shell nanostructures using a clean physical preparation method.
2. We found that the noble metal NPs' particle size increases when the pulsed laser energy increases.
3. It also noted from the results obtained that the thickness of the silicon oxide shell does not change with increased pulsed laser energy.
4. The optical energy gap (E_g) values of core shell NPs obtained from the UV-Vis and PL measurements were very close.
5. From the XRD results, we notice an increase in crystallite size at a certain diffraction angle with an increase in laser fluence, confirmed by transmission electron microscopy images.
6. We have successfully fabricated Plasmonic DSSCs and compared them with regular DSSC, and we found an increase in solar cell efficiency after loaded Plasmonic NPs.
7. the solar cell efficiency enhanced by a Gold-Silica core-shell is more than that enhanced by a Silver-Silica core-shell due to the position surface Plasmon resonance of core-shell nanoparticles.

This is real and scientific because the dye works better in the visible range of five hundred nanometers, which is one of the optical properties of nano-gold.



REFERENCE

1. Europe, S. (2020). *Global market outlook for solar power/2020–2024*. Solar Power Europe, Brussels.
2. Tollefson, J. (2022). What the war in Ukraine means for energy, climate and food. *Nature*, 604(7905), 232-233.
3. Sharma, K., Sharma, V. and Sharma, S. S. (2018). Dye-sensitized solar cells: fundamentals and current status. *Nanoscale Research Letters*, 13(1), 1-46.
4. Veith-Wolf, B. A., Schäfer, S., Brendel, R. and Schmidt, J. (2018). Reassessment of intrinsic lifetime limit in n-type crystalline silicon and implication on maximum solar cell efficiency. *Solar Energy Materials and Solar Cells*, 186, 194-199.
5. Hayat, M. B., Ali, D., Monyake, K. C., Alagha, L. and Ahmed, N. (2019). Solar energy—A look into power generation, challenges, and a solar-powered future. *International Journal of Energy Research*, 43(3), 1049-1067.
6. Husain, A. A., Hasan, W. Z. W., Shafie, S., Hamidon, M. N. and Pandey, S. S. (2018). A review of transparent solar photovoltaic technologies. *Renewable And Sustainable Energy Reviews*, 94, 779-791.
7. Singh, B. P., Goyal, S. K. and Kumar, P. (2021). Solar PV cell materials and technologies: Analyzing the recent developments. *Materials Today: Proceedings*, 43, 2843-2849.
8. Tawalare, P. K. (2021). Optimizing photovoltaic conversion of solar energy. *AIP Advances*, 11(10), 100701.
9. Ibn-Mohammed, T., Koh, S. C. L., Reaney, I. M., Acquaye, A., Schileo, G., Mustapha, K. B. and Greenough, R. (2017). Perovskite solar cells: An integrated hybrid lifecycle assessment and review in comparison with other photovoltaic technologies. *Renewable and Sustainable Energy Reviews*, 80, 1321-1344.
10. Vasiliev, M., Nur-E.-Alam, M. and Alameh, K. (2019). Recent developments in solar energy-harvesting technologies for building integration and distributed energy generation. *Energies*, 12(6), 1080.
11. Internet: National Renewable Energy Laboratory. (2020). Best research-cell efficiency chart. Web: <https://www.nrel.gov/pv/cell-efficiency.html>, Erişim tarihi: 05.06.2022.
12. Gul, M., Kotak, Y. and Muneer, T. (2016). Review on recent trend of solar photovoltaic technology. *Energy Exploration & Exploitation*, 34(4), 485-526.
13. Sharma, S., Jain, K. K. and Sharma, A. (2015). Solar cells: in research and applications—a review. *Materials Sciences and Applications*, 6(12), 1145.

14. Vigil-Galán, O., Courel, M., Andrade-Arvizu, J. A., Sánchez, Y., Espíndola-Rodríguez, M., Saucedo, E. and Titsworth, M. (2015). Route towards low cost-high efficiency second generation solar cells: current status and perspectives. *Journal of Materials Science: Materials in Electronics*, 26(8), 5562-5573.
15. Moon, M., Alam, M., Rahman, M., Hossain, J. and Ismail, A. B. M. (2019). Comparative study of the second generation a-Si: H, CdTe, and CIGS thin-film solar cells. *In Advanced Materials Research* 102-111. Zurich: Trans Tech Publications Ltd.
16. Mrinalini, M., Islavath, N., Prasanthkumar, S. and Giribabu, L. (2019). Stipulating low production cost solar cells all set to retail...!. *The Chemical Record*, 19(2-3), 661-674.
17. Liu, J., Yao, M. and Shen, L. (2019). Third generation photovoltaic cells based on photonic crystals. *Journal of Materials Chemistry C*, 7(11), 3121-3145.
18. Parisi, M. L., Maranghi, S., Vesce, L., Sinicropi, A., Di Carlo, A. and Basosi, R. (2020). Prospective life cycle assessment of third-generation photovoltaics at the pre-industrial scale: A long-term scenario approach. *Renewable and Sustainable Energy Reviews*, 121, 109703.
19. Buitrago, E., Novello, A. M. and Meyer, T. (2020). Third-generation solar cells: toxicity and risk of exposure. *Helvetica Chimica Acta*, 103(9), e2000074.
20. Taya, S. A., El-Agez, T. M., El-Ghamri, H. S. and Abdel-Latif, M. S. (2013). Dye-sensitized solar cells using fresh and dried natural dyes. *International Journal of Materials Science and Applications*, 2(2), 37-42.
21. Nwanya, A. C., Ezema, F. I. and Ejikeme, P. M. (2011). Dyed sensitized solar cells: A technically and economically alternative concept to pn junction photovoltaic devices. *International Journal of Physical Sciences*, 6(22), 5190-5201.
22. O'regan, B. and Grätzel, M. (1991). A low-cost, high-efficiency solar cell based on dye-sensitized colloidal TiO₂ films. *Nature*, 353(6346), 737-740.
23. Internet: Sen, A., Putra, M. H., Biswas, A. K., Behera, A. K. B. and Gross, A. (2022). A Brief History of and Insight in the Choice of Sensitizers/Dyes for Dye Sensitized Solar Cells. Web: <https://chemrxiv.org/engage/api-gateway/chemrxiv/assets/orp/resource/item/62a21e04bb751904a5487692/original/a-brief-history-of-and-insight-in-the-choice-of-sensitizers-dyes-for-dye-sensitized-solar-cells.pdf>, son Erişim tarihi: 06.04.2022.
24. Bella, F., Gerbaldi, C., Barolo, C. and Grätzel, M. (2015). Aqueous dye-sensitized solar cells. *Chemical Society Reviews*, 44(11), 3431-3473.
25. Wang, P., Yang, L., Wu, H., Cao, Y., Zhang, J., Xu, N., Chen, S., Decoppet, J.D., Zakeeruddin, S.M. and Grätzel, M. (2018). Stable and efficient organic dye-sensitized solar cell based on ionic liquid electrolyte. *Joule*, 2(10), 2145-2153.
26. Peddapuram, A., Cheema, H., Adams, R. E., Schmehl, R. H. and Delcamp, J. H. (2017). A stable panchromatic green dual acceptor, dual donor organic dye for dye-sensitized solar cells. *The Journal of Physical Chemistry C*, 121(16), 8770-8780.

27. Kunzmann, A., Valero, S., Sepúlveda, Á. E., Rico-Santacruz, M., Lalinde, E., Berenguer, J. R., Maritnez, J.G., Guldi, D.M., Serrano, E. and Costa, R. D. (2018). Hybrid dye-titania nanoparticles for superior low-temperature dye-sensitized solar cells. *Advanced Energy Materials*, 8(12), 1702583.
28. Karim, N. A., Mehmood, U., Zahid, H. F. and Asif, T. (2019). Nanostructured photoanode and counter electrode materials for efficient dye-sensitized solar cells (DSSCs). *Solar Energy*, 185, 165-188.
29. Anbarasan, P. M., Priyadharsini, C. I., Sathiyapriya, R., Hariharan, V., Parabakaran, K. and Aroulmoji, V. (2019). Development of TiO₂ nanomaterials and dyes selection (using DFT) for DSSC applications—a stepwise review. *International journal of advanced Science and Engineering*, 6(02), 1326-1350.
30. Gong, J., Sumathy, K., Qiao, Q. and Zhou, Z. (2017). Review on dye-sensitized solar cells (DSSCs): Advanced techniques and research trends. *Renewable and Sustainable Energy Reviews*, 68, 234-246.
31. Li, F., Bashir, S. and Liu, J. L. (2018). *Nanostructured materials for next-generation energy storage and conversion*. New York: Springer.
32. An, P., Kim, J. H., Shin, M., Kim, S., Cho, S., Park, C., Kim, G., Lee, H.W., Choi, J., Ahn, C. and Song, M. (2022). Efficient and stable fiber dye-sensitized solar cells based on solid-state Li-TFSI electrolytes with 4-Oxo-TEMPO derivatives. *Nanomaterials*, 12(13), 2309.
33. Ali, A., El-Mellouhi, F., Mitra, A. and Aïssa, B. (2022). Research progress of plasmonic nanostructure-enhanced photovoltaic solar cells. *Nanomaterials*, 12(5), 788.
34. Krajczewski, J., Kołataj, K. and Kudelski, A. (2017). Plasmonic nanoparticles in chemical analysis. *RSC Advances*, 7(28), 17559-17576.
35. Al-Amri, M. D., El-Gomati, M. and Zubairy, M. S. (2016). *Optics in our time*. New York: Springer Nature.
36. Dombi, P., Pápa, Z., Vogelsang, J., Yalunin, S. V., Sivis, M., Herink, G., Schafer, S., Gross, P., Ropers, C. and Lienau, C. (2020). Strong-field nano-optics. *Reviews of Modern Physics*, 92(2), 025003.
37. Smirnov, V., Stephan, S., Westphal, M., Emmrich, D., Beyer, A., Gölzhäuser, A., Lienau, C. and Silies, M. (2021). Transmitting surface plasmon polaritons across nanometer-sized gaps by optical near-field coupling. *ACS Photonics*, 8(3), 832-840.
38. Kostina, N., Petrov, M., Ivinskaya, A., Sukhov, S., Bogdanov, A., Toftul, I., Vesperinas, M.N., Ginzburg, P. and Shalin, A. (2019). Optical binding via surface plasmon polariton interference. *Physical Review B*, 99(12), 125416.
39. Linic, S., Christopher, P. and Ingram, D. B. (2011). Plasmonic-metal nanostructures for efficient conversion of solar to chemical energy. *Nature Materials*, 10(12), 911-921.

40. Jatschka, J., Dathe, A., Csáki, A., Fritzsche, W. and Stranik, O. (2016). Propagating and localized surface plasmon resonance sensing—A critical comparison based on measurements and theory. *Sensing and Bio-Sensing Research*, 7, 62-70.
41. Wilson, A. J. and Willets, K. A. (2016). Molecular plasmonics. *Annual Review of Analytical Chemistry*, 9, 27-43.
42. Rodriguez, R. D., Sheremet, E., Nesterov, M., Moras, S., Rahaman, M., Weiss, T., Hietschold, M. and Zahn, D. R. (2018). Aluminum and copper nanostructures for surface-enhanced Raman spectroscopy: A one-to-one comparison to silver and gold. *Sensors and Actuators B: Chemical*, 262, 922-927.
43. Jana, J., Ganguly, M. and Pal, T. (2016). Enlightening surface plasmon resonance effect of metal nanoparticles for practical spectroscopic application. *RSC Advances*, 6(89), 86174-86211.
44. Rizal, C., Pisana, S. and Hrvoic, I. (2018). Improved magneto-optic surface plasmon resonance biosensors. *Photonics* 5(3), 15-20.
45. Petridis, C., Savva, K., Kymakis, E. and Stratakis, E. (2017). Laser generated nanoparticles based photovoltaics. *Journal of Colloid and Interface Science*, 489, 28-37.
46. Agrawal, A., Cho, S. H., Zandi, O., Ghosh, S., Johns, R. W. and Milliron, D. J. (2018). Localized surface plasmon resonance in semiconductor nanocrystals. *Chemical Reviews*, 118(6), 3121-3207.
47. Gan, X., Lei, D., Ye, R., Zhao, H. and Wong, K. Y. (2021). Transition metal dichalcogenide-based mixed-dimensional heterostructures for visible-light-driven photocatalysis: Dimensionality and interface engineering. *Nano Research*, 14(6), 2003-2022.
48. Olaimat, M. M., Yousefi, L. and Ramahi, O. M. (2021). Using plasmonics and nanoparticles to enhance the efficiency of solar cells: review of latest technologies. *JOSA B*, 38(2), 638-651.
49. Liang, Z., Sun, J., Jiang, Y., Jiang, L. and Chen, X. (2014). Plasmonic enhanced optoelectronic devices. *Plasmonics*, 9(4), 859-866.
50. Morawiec, S., Mendes, M. J., Priolo, F. and Crupi, I. (2019). Plasmonic nanostructures for light trapping in thin-film solar cells. *Materials Science in Semiconductor Processing*, 92, 10-18.
51. Medici, S., Peana, M., Nurchi, V. M., Lachowicz, J. I., Crisponi, G. and Zoroddu, M. A. (2015). Noble metals in medicine: Latest advances. *Coordination Chemistry Reviews*, 284, 329-350.
52. Azharuddin, M., Zhu, G. H., Das, D., Ozgur, E., Uzun, L., Turner, A. P. and Patra, H. K. (2019). A repertoire of biomedical applications of noble metal nanoparticles. *Chemical Communications*, 55(49), 6964-6996.

53. Doria, G., Conde, J., Veigas, B., Giestas, L., Almeida, C., Assunção, M., Rosa, J. and Baptista, P. V. (2012). Noble metal nanoparticles for biosensing applications. *Sensors*, 12(2), 1657-1687.
54. Jiang, N., Zhuo, X. and Wang, J. (2017). Active plasmonics: principles, structures, and applications. *Chemical Reviews*, 118(6), 3054-3099.
55. Hsu, S. W., Rodarte, A. L., Som, M., Arya, G. and Tao, A. R. (2018). Colloidal plasmonic nanocomposites: from fabrication to optical function. *Chemical Reviews*, 118(6), 3100-3120.
56. Willets, K. A. and Van Duyne, R. P. (2007). Localized surface plasmon resonance spectroscopy and sensing. *Annual Review of Physical Chemistry*, 58(1), 267-297.
57. Wang, D., Guan, J., Hu, J., Bourgeois, M. R. and Odom, T. W. (2019). Manipulating light-matter interactions in plasmonic nanoparticle lattices. *Accounts of Chemical Research*, 52(11), 2997-3007.
58. Amendola, V., Bakr, O. M. and Stellacci, F. (2010). A study of the surface plasmon resonance of silver nanoparticles by the discrete dipole approximation method: effect of shape, size, structure, and assembly. *Plasmonics*, 5(1), 85-97.
59. Park, J. E., Lee, Y. and Nam, J. M. (2018). Precisely shaped, uniformly formed gold nanocubes with ultrahigh reproducibility in single-particle scattering and surface-enhanced Raman scattering. *Nano Letters*, 18(10), 6475-6482.
60. Hu, M., Novo, C., Funston, A., Wang, H., Staleva, H., Zou, S., Mulvaney, P., Xia, Y. and Hartland, G. V. (2008). Dark-field microscopy studies of single metal nanoparticles: understanding the factors that influence the linewidth of the localized surface plasmon resonance. *Journal of Materials Chemistry*, 18(17), 1949-1960.
61. Tran, V., Thiel, C., Svejda, J. T., Jalali, M., Walkenfort, B., Erni, D. and Schlücker, S. (2018). Probing the SERS brightness of individual Au nanoparticles, hollow Au/Ag nanoshells, Au nanostars and Au core/Au satellite particles: single-particle experiments and computer simulations. *Nanoscale*, 10(46), 21721-21731.
62. Ruan, Q., Shao, L., Shu, Y., Wang, J. and Wu, H. (2014). Growth of monodisperse gold nanospheres with diameters from 20 nm to 220 nm and their core/satellite nanostructures. *Advanced Optical Materials*, 2(1), 65-73.
63. Wang, Y., Zhang, J., Liang, W., Yang, H., Guan, T., Zhao, B., Sun, Y., Chi, L. and Jiang, L. (2022). Rational design of plasmonic metal nanostructures for solar energy conversion. *CCS Chemistry*, 4(4), 1153-1168.
64. Jiang, R., Li, B., Fang, C. and Wang, J. (2014). Metal/semiconductor hybrid nanostructures for plasmon-enhanced applications. *Advanced Materials*, 26(31), 5274-5309.
65. Chen, T. and Reinhard, B. M. (2016). Assembling color on the nanoscale: multichromatic switchable pixels from plasmonic atoms and molecules. *Advanced Materials*, 28(18), 3522-3527.

66. Zhang, H., Kinnear, C. and Mulvaney, P. (2020). Fabrication of Single-Nanocrystal Arrays. *Advanced Materials*, 32(18), 1904551.
67. Nahm, C., Choi, H., Kim, J., Jung, D. R., Kim, C., Moon, J., Lee, B. and Park, B. (2011). The effects of 100 nm-diameter Au nanoparticles on dye-sensitized solar cells. *Applied Physics Letters*, 99(25), 253107.
68. Qi, J., Dang, X., Hammond, P. T. and Belcher, A. M. (2011). Highly efficient plasmon-enhanced dye-sensitized solar cells through metal@ oxide core-shell nanostructure. *ACS Nano*, 5(9), 7108-7116.
69. Brown, M. D., Suteewong, T., Kumar, R. S. S., D'Innocenzo, V., Petrozza, A., Lee, M. M., Lee, M.M., Wiesner, U. and Snaith, H. J. (2011). Plasmonic dye-sensitized solar cells using core-shell metal-insulator nanoparticles. *Nano Letters*, 11(2), 438-445.
70. Choi, H., Chen, W. T. and Kamat, P. V. (2012). Know thy nano neighbor. Plasmonic versus electron charging effects of metal nanoparticles in dye-sensitized solar cells. *ACS Nano*, 6(5), 4418-4427.
71. Zarick, H. F., Hurd, O., Webb, J. A., Hungerford, C., Erwin, W. R. and Bardhan, R. (2014). Enhanced efficiency in dye-sensitized solar cells with shape-controlled plasmonic nanostructures. *Acs Photonics*, 1(9), 806-811.
72. Elbohy, H., Kim, M. R., Dubey, A., Reza, K. M., Ma, D., Zai, J., Qian, X. and Qiao, Q. (2016). Incorporation of plasmonic Au nanostars into photoanodes for high efficiency dye-sensitized solar cells. *Journal of Materials Chemistry A*, 4(2), 545-551.
73. Bai, L., Li, M., Guo, K., Luoshan, M., Mehnane, H. F., Pei, L., Pan, M., Liao, L. and Zhao, X. (2014). Plasmonic enhancement of the performance of dye-sensitized solar cell by core-shell AuNRs@ SiO₂ in composite photoanode. *Journal of Power Sources*, 272, 1100-1105.
74. Guo, K., Li, M., Fang, X., Liu, X., Zhu, Y., Hu, Z. and Zhao, X. (2013). Enhancement of properties of dye-sensitized solar cells by surface plasmon resonance of Ag nanowire core-shell structure in TiO₂ films. *Journal of Materials Chemistry A*, 1(24), 7229-7234.
75. Gangishetty, M. K., Lee, K. E., Scott, R. W. and Kelly, T. L. (2013). Plasmonic enhancement of dye sensitized solar cells in the red-to-near-infrared region using triangular core-shell Ag@ SiO₂ nanoparticles. *ACS Applied Materials & Interfaces*, 5(21), 11044-11051.
76. Kim, H. Y. and Suh, J. S. (2015). Panchromatic quasi-monolayer of Ag nanoparticles for high-efficiency dye-sensitized solar cells. *RSC Advances*, 5(74), 59895-59902.
77. Al-Azawi, M. A., Bidin, N., Bououdina, M. and Mohammad, S. M. (2016). Preparation of gold and gold-silver alloy nanoparticles for enhancement of plasmonic dye-sensitized solar cells performance. *Solar Energy*, 126, 93-104.

78. Xu, Q., Liu, F., Liu, Y., Cui, K., Feng, X., Zhang, W. and Huang, Y. (2013). Broadband light absorption enhancement in dye-sensitized solar cells with Au-Ag alloy popcorn nanoparticles. *Scientific Reports*, 3(1), 1-7.
79. Yun, J., Hwang, S. H. and Jang, J. (2015). Fabrication of Au@ Ag core/shell nanoparticles decorated TiO₂ hollow structure for efficient light-harvesting in dye-sensitized solar cells. *ACS Applied Materials & Interfaces*, 7(3), 2055-2063.
80. Dong, H., Wu, Z., El-Shafei, A., Xia, B., Xi, J., Ning, S., Jiao, B. and Hou, X. (2015). Ag-encapsulated Au plasmonic nanorods for enhanced dye-sensitized solar cell performance. *Journal of Materials Chemistry A*, 3(8), 4659-4668.
81. Wang, Y., Zhai, J., Song, Y. and He, L. (2016). The Ag shell thickness effect of Au@ Ag@ SiO₂ core-shell nanoparticles on the optoelectronic performance of dye sensitized solar cells. *Chemical Communications*, 52(11), 2390-2393.
82. Ahn, S., Rourke, D. and Park, W. (2016). Plasmonic nanostructures for organic photovoltaic devices. *Journal of Optics*, 18(3), 033001.
83. Puspitasari, R. N., Budiarti, H. A., Hatta, A. M. and Risanti, D. D. (2017). Enhanced dye-sensitized solar cells performance through novel core-shell structure of gold nanoparticles and nano-silica extracted from Lapindo Mud Vulcano. *Procedia Engineering*, 170, 93-100.
84. Wang, B., Zhu, X., Li, S., Chen, M., Lu, H. and Yang, Y. (2018). Ag@ SiO₂ core-shell nanoparticles embedded in a TiO₂ mesoporous layer substantially improve the performance of perovskite solar cells. *Nanomaterials*, 8(9), 701.
85. Neshat, A. and Safdari, R. (2019). Enhancement in Dye-Sensitized Solar Cells Using Surface Plasmon Resonance Effects from Colloidal Core-Shell Au@ SiO₂ Nanoparticles. *Chemistry Select*, 4(17), 4995-5001.
86. Weng, L., Wang, X., Zhang, X., Guan, L., Liu, L., Zhang, H. and Cui, W. (2020). The effect of Ag@ SiO₂ core-shell nanoparticles on the dielectric properties of PVDF based nanocomposites. *Polymer Composites*, 41(6), 2245-2253.
87. Perdana, I. and Muldarisnur, M. (2021, March). Optimization of Ag-SiO₂ core-shell nanoparticles arrangement for light absorption enhancement in organic solar cells. *In AIP Conference Proceedings*, 2320 (1), 030008.
88. Alikhaidarova, E., Afanasyev, D., Ibrayev, N. and Nuraje, N. (2022). Plasmonic enhanced polymer solar cell with inclusion of Ag@ SiO₂ core-shell nanostructures. *Polymers for Advanced Technologies*, 33(3), 1000-1008.
89. Lu, M. Y., Tsai, C. Y., Chen, H. A., Liang, Y. T., Chen, K. P., Gradečak, S., Gwo, S. and Chen, L. J. (2016). Plasmonic enhancement of Au nanoparticle—embedded single-crystalline ZnO nanowire dye-sensitized solar cells. *Nano Energy*, 20, 264-271.
90. Chang, S., Li, Q., Xiao, X., Wong, K. Y. and Chen, T. (2012). Enhancement of low energy sunlight harvesting in dye-sensitized solar cells using plasmonic gold nanorods. *Energy & Environmental Science*, 5(11), 9444-9448.

91. Erwin, W. R., Zarick, H. F., Talbert, E. M. and Bardhan, R. (2016). Light trapping in mesoporous solar cells with plasmonic nanostructures. *Energy & Environmental Science*, 9(5), 1577-1601.
92. Kawawaki, T., Wang, H., Kubo, T., Saito, K., Nakazaki, J., Segawa, H. and Tatsuma, T. (2015). Efficiency enhancement of PbS quantum dot/ZnO nanowire bulk-heterojunction solar cells by plasmonic silver nanocubes. *ACS Nano*, 9(4), 4165-4172.
93. Kochuveedu, S. T., Jang, Y. H. and Kim, D. H. (2013). A study on the mechanism for the interaction of light with noble metal-metal oxide semiconductor nanostructures for various photophysical applications. *Chemical Society Reviews*, 42(21), 8467-8493.
94. Bae, S. H., Zhao, H., Hsieh, Y. T., Zuo, L., De Marco, N., Rim, Y. S., Li, G. and Yang, Y. (2016). Printable solar cells from advanced solution-processible materials. *Chem*, 1(2), 197-219.
95. Alicki, R., Gelbwaser-Klimovsky, D. and Jenkins, A. (2017). A thermodynamic cycle for the solar cell. *Annals of Physics*, 378, 71-87.
96. Khan, M. I. (2013). *A study on the optimization of dye-sensitized solar cells*. Florida: University of South Florida.
97. Tao, Y. (2016). *Screen-printed front junction n-type silicon solar cells*. London: Intech Open.
98. Kirchartz, T. and Rau, U. (2018). What makes a good solar cell?. *Advanced Energy Materials*, 8(28), 1703385.
99. Bartesaghi, D., Pérez, I. D. C., Kniepert, J., Roland, S., Turbiez, M., Neher, D. and Koster, L. (2015). Competition between recombination and extraction of free charges determines the fill factor of organic solar cells. *Nature Communications*, 6(1), 1-10.
100. Van Dyk, E. E. and Meyer, E. L. (2004). Analysis of the effect of parasitic resistances on the performance of photovoltaic modules. *Renewable Energy*, 29(3), 333-344.
101. Almomani, M., Al-Dmour, A. S. and Algharaibeh, S. (2020). Application of Artificial Intelligence Techniques for Modeling and Simulation of Photovoltaic Arrays. *Jordan Journal of Electrical Engineering* 6(4), 296-314.
102. Hagfeldt, A. and Graetzel, M. (1995). Light-induced redox reactions in nanocrystalline systems. *Chemical Reviews*, 95(1), 49-68.
103. Dai, S. (Ed.). (2022). *Dye-sensitized solar cells (Vol. 7)*. Berlin: Walter de Gruyter GmbH & Co KG.
104. Lau, K. K. and Soroush, M. (2019). Overview of dye-sensitized solar cells. In *Dye-Sensitized Solar Cells* (pp. 1-49). Cambridge: Academic Press.

105. Nazeeruddin, M. K., Kay, A., Rodicio, I., Humphry-Baker, R., Müller, E., Liska, P., Vlachopoulos, N. and Grätzel, M. (1993). Conversion of light to electricity by cis-X₂bis (2, 2'-bipyridyl-4, 4'-dicarboxylate) ruthenium (II) charge-transfer sensitizers (X= Cl-, Br-, I-, CN-, and SCN-) on nanocrystalline titanium dioxide electrodes. *Journal of the American Chemical Society*, 115(14), 6382-6390.
106. Nazeeruddin, M. K., Baranoff, E. and Grätzel, M. (2011). Dye-sensitized solar cells: A brief overview. *Solar Energy*, 85(6), 1172-1178.
107. Narayan, M. R. (2012). Dye sensitized solar cells based on natural photosensitizers. *Renewable and Sustainable Energy Reviews*, 16(1), 208-215.
108. Bakar, S. A., Marwoto, P., Wibowo, K. M., Muqoyyanah, M. and Firdaus, F. (2020). Effects of various semiconducting oxides as photoanode and counter electrode for dye sensitized solar cell application-a review. *Indonesian Journal of Applied Physics*, 10(2), 126-147.
109. Devadiga, D., Selvakumar, M., Shetty, P. and Santosh, M. S. (2021). Recent progress in dye sensitized solar cell materials and photo-supercapacitors: A review. *Journal of Power Sources*, 493, 229698.
110. Genesisio, G., Maynadić, J., Carboni, M. and Meyer, D. (2018). Recent status on MOF thin films on transparent conductive oxides substrates (ITO or FTO). *New Journal of Chemistry*, 42(4), 2351-2363.
111. Suhaimi, S., Shahimin, M. M., Alahmed, Z. A., Chyský, J. and Reshak, A. H. (2015). Materials for enhanced dye-sensitized solar cell performance: Electrochemical application. *International Journal of Electrochemical Science*, 10(4), 2859-2871.
112. Andualem, A. and Demiss, S. (2018). Review on dye-sensitized solar cells (DSSCs). *Edelweiss Applied Science and Technology*, 2, 145-150.
113. Chen, H. W., Huang, K. C., Hsu, C. Y., Lin, C. Y., Chen, J. G., Lee, C. P., Lin, L., Vittal, R. and Ho, K. C. (2011). Electrophoretic deposition of TiO₂ film on titanium foil for a flexible dye-sensitized solar cell. *Electrochimica Acta*, 56(23), 7991-7998.
114. Xu, Y., Xu, X., Li, M. and Lu, W. (2020). Prediction of photoelectric properties, especially power conversion efficiency of cells, of IQ1 and derivative dyes in high-efficiency dye-sensitized solar cells. *Solar Energy*, 195, 82-88.
115. Jasim, K. E. (2011). Dye sensitized solar cells-working principles, challenges and opportunities. *Solar Cells-Dye-Sensitized Devices*, 8, 172-210.
116. Mehmood, U., Rahman, S. U., Harrabi, K., Hussein, I. A. and Reddy, B. V. S. (2014). Recent advances in dye sensitized solar cells. *Advances in Materials Science and Engineering*, 2014.
117. M. A. Ahmed, M. Dirar, M. A. Siddig, and S. M. H. Abdalsakhi. (2018), The effect of eriochrome black t concentrations on the efficiency of dye-sensitized solar cells, *Asian Journal of Research and Reviews in Physics* 1(3), 1-13.

118. Alhorani, S., Kumar, S., Genwa, M. and Meena, P. L. (2020). Review of latest efficient sensitizer in dye-sensitized solar cells. *AIP Conference Proceedings*, 2265 (1), 030632.
119. Mohamad, A. A. (2019). Physical properties of quasi-solid-state polymer electrolytes for dye-sensitized solar cells: A characterisation review. *Solar Energy*, 190, 434-452.
120. Karuppasamy, K., Theerthagiri, J., Vikraman, D., Yim, C. J., Hussain, S., Sharma, R., Maiyalagan, T., Qin, J. and Kim, H. S. (2020). Ionic liquid-based electrolytes for energy storage devices: A brief review on their limits and applications. *Polymers*, 12(4), 918.
121. Yoo, K., Nath, N. C. D., Kang, H. C., Muthu, S. and Lee, J. J. (2021). Binary redox couples for highly transparent and high-voltage dye-sensitized solar cells. *ECS Journal of Solid State Science and Technology*, 10(2), 025007.
122. Zulkifili, A. N. B., Kento, T., Daiki, M. and Fujiki, A. (2015). The basic research on the dye-sensitized solar cells (DSSC). *Journal of Clean Energy Technologies*, 3(5), 382-387.
123. Sakthivel, S., Baskaran, V. and Mahenthiran, S. (2015). Dye sensitized solar cell properties and fabrication using *Lawsonia inermis*. *Journal of Chemical Sciences*, 5(2), 85-92.
124. Mariotti, N., Bonomo, M., Fagiolari, L., Barbero, N., Gerbaldi, C., Bella, F. and Barolo, C. (2020). Recent advances in eco-friendly and cost-effective materials towards sustainable dye-sensitized solar cells. *Green Chemistry*, 22(21), 7168-7218.
125. Tomar, N., Agrawal, A., Dhaka, V. S. and Surolia, P. K. (2020). Ruthenium complexes based dye sensitized solar cells: Fundamentals and research trends. *Solar Energy*, 207, 59-76.
126. Internet: Garcia Mayo, S. (2021). Dye-Sensitized Solar Cells: the future of consumer electronics?.
Web:<https://www.divaportal.org/smash/get/diva2:1590541/FULLTEXT01.pdf>, son Erişim tarihi: 08.06.2022.
127. Kadem, B. Y., Ali, M. J. M. and Abdulameer, A. F. (2019, October). The effects of Al-doped ZnO layer on the performance of organic solar cell. In *2019 12th International Conference on Developments in eSystems Engineering (DeSE)* (pp. 741-746). New Jersey: IEEE.
128. Anbarasan, P. M., Priyadharsini, C. I., Sathiyapriya, R., Hariharan, V., Parabakaran, K. and Aroulmoji, V. (2019). Development of TiO₂ nanomaterials and dyes selection (using DFT) for DSSC applications—a stepwise review. *International Journal of Advanced Science and Engineering*, 6(02), 1326-1350.
129. Khan, A. U., Zhao, S. and Liu, G. (2016). Key parameter controlling the sensitivity of plasmonic metal nanoparticles: aspect ratio. *The Journal of Physical Chemistry C*, 120(34), 19353-19364.

130. Wang, L., Hasanzadeh Kafshgari, M. and Meunier, M. (2020). Optical properties and applications of plasmonic-metal nanoparticles. *Advanced Functional Materials*, 30(51), 2005400.
131. Schasfoort, R. B. (Ed.). (2017). *Handbook of surface plasmon resonance*. Londra: Royal Society of Chemistry
132. Liz-Marzán, L. (Ed.). (2020). *Colloidal synthesis of plasmonic nanometals*. Florida: CRC Press.
133. Rodrigues, T. S., da Silva, A. G. and Camargo, P. H. (2019). Nanocatalysis by noble metal nanoparticles: controlled synthesis for the optimization and understanding of activities. *Journal of Materials Chemistry A*, 7(11), 5857-5874.
134. Petryayeva, E. and Krull, U. J. (2011). Localized surface plasmon resonance: Nanostructures, bioassays and biosensing—A review. *Analytica Chimica Acta*, 706(1), 8-24.
135. Habibullah, G., Viktorova, J. and Ruml, T. (2021). Current strategies for noble metal nanoparticle synthesis. *Nanoscale Research Letters*, 16(1), 1-12.
136. Jamkhande, P. G., Ghule, N. W., Bamer, A. H. and Kalaskar, M. G. (2019). Metal nanoparticles synthesis: An overview on methods of preparation, advantages and disadvantages, and applications. *Journal of Drug Delivery Science and Technology*, 53, 101174.
137. Baig, N., Kammakam, I. and Falath, W. (2021). Nanomaterials: A review of synthesis methods, properties, recent progress, and challenges. *Materials Advances*, 2(6), 1821-1871.
138. Ghassan, A. A., Mijan, N. A. and Taufiq-Yap, Y. H. (2019). Nanomaterials: an overview of nanorods synthesis and optimization. *Nanorods and Nanocomposites*, 11(11), 8-33.
139. Zhang, J., Chaker, M. and Ma, D. (2017). Pulsed laser ablation based synthesis of colloidal metal nanoparticles for catalytic applications. *Journal of Colloid and Interface Science*, 489, 138-149.
140. Chrzanowska, J., Hoffman, J., Małolepszy, A., Mazurkiewicz, M., Kowalewski, T. A., Szymanski, Z. and Stobinski, L. (2015). Synthesis of carbon nanotubes by the laser ablation method: Effect of laser wavelength. *Physica Status Solidi (b)*, 252(8), 1860-1867.
141. Duque, J. S., Madrigal, B. M., Riascos, H. and Avila, Y. P. (2019). Colloidal metal oxide nanoparticles prepared by laser ablation technique and their antibacterial test. *Colloids and Interfaces*, 3(1), 25.
142. Hut, I., Matija, L., Peric, M., Nikolovski, P. and Pelemis, S. (2018). Nanomaterials for sustainable energy production and storage: Present day applications and possible developments. In *Commercialization of Nanotechnologies—A Case Study Approach* (pp. 31-72). Berlin: Springer.

143. Park, H., Reddy, D. A., Kim, Y., Lee, S., Ma, R. and Kim, T. K. (2017). Synthesis of ultra-small palladium nanoparticles deposited on CdS nanorods by pulsed laser ablation in liquid: role of metal nanocrystal size in the photocatalytic hydrogen production. *Chemistry–A European Journal*, 23(53), 13112-13119.
144. Abid, N., Khan, A. M., Shujait, S., Chaudhary, K., Ikram, M., Imran, M., Haider, J., Khan, M., Khan, Q. and Maqbool, M. (2021). Synthesis of nanomaterials using various top-down and bottom-up approaches, influencing factors, advantages, and disadvantages: A review. *Advances in Colloid and Interface Science*, 102597.
145. Ismail, R. A., Mohsin, M. H., Ali, A. K., Hassoon, K. I. and Erten-Ela, S. (2020). Preparation and characterization of carbon nanotubes by pulsed laser ablation in water for optoelectronic application. *Physica E: Low-dimensional Systems and Nanostructures*, 119, 113997.
146. Zhang, J., Claverie, J., Chaker, M. and Ma, D. (2017). Colloidal metal nanoparticles prepared by laser ablation and their applications. *Chem Phys Chem*, 18(9), 986-1006.
147. Tong, Y., Liang, X., Bai, S. and Qin, Q. H. (2016). Laser Ablation Applications in Ablation-Resistance Characterization of Materials. In Applications of Laser Ablation-Thin Film Deposition, Nanomaterial Synthesis and Surface Modification. *IntechOpen*.
148. Schille, J., Schneider, L., Hartwig, L., Loeschner, U., Ebert, R., Scully, P., Goddard, N.J. and Exner, H. (2012). *Characterisation of interaction phenomena in high repetition rate femtosecond laser ablation of metals*. International Congress on Applications of Lasers & Electro-Optics, Orlando, 949-958
149. Leone, C., Genna, S., Tagliaferri, F., Palumbo, B. and Dix, M. (2016). Experimental investigation on laser milling of aluminium oxide using a 30 W Q-switched Yb: YAG fiber laser. *Optics & Laser Technology*, 76, 127-137.
150. Min, J., Wan, H., Carlson, B. E., Lin, J. and Sun, C. (2020). Application of laser ablation in adhesive bonding of metallic materials: A review. *Optics & Laser Technology*, 128, 106188.
151. Xiao, J., Liu, P., Wang, C. X. and Yang, G. W. (2017). External field-assisted laser ablation in liquid: An efficient strategy for nanocrystal synthesis and nanostructure assembly. *Progress in Materials Science*, 87, 140-220.
152. Amendola, V. and Meneghetti, M. (2013). What controls the composition and the structure of nanomaterials generated by laser ablation in liquid solution?. *Physical Chemistry Chemical Physics*, 15(9), 3027-3046.
153. Petersen, S., Barchanski, A., Taylor, U., Klein, S., Rath, D. and Barcikowski, S. (2011). Penetratin-conjugated gold nanoparticles— design of cell-penetrating nanomarkers by femtosecond laser ablation. *The Journal of Physical Chemistry C*, 115(12), 5152-5159.
154. Yang, S., Zeng, H., Zhao, H., Zhang, H. and Cai, W. (2011). Luminescent hollow carbon shells and fullerene-like carbon spheres produced by laser ablation with toluene. *Journal of Materials Chemistry*, 21(12), 4432-4436.

155. Besner, S. and Meunier, M. (2010). Femtosecond laser synthesis of AuAg nanoalloys: photoinduced oxidation and ions release. *The Journal of Physical Chemistry C*, 114(23), 10403-10409.
156. Verma, K. K., Song, X. P., Joshi, A., Tian, D. D., Rajput, V. D., Singh, M., ... & Li, Y. R. (2022). Recent Trends in Nano-Fertilizers for Sustainable Agriculture under Climate Change for Global Food Security. *Nanomaterials*, 12(1), 173.
157. Thodeti, S., Reddy, R. M. and Kumar, J. S. (2016). Synthesis and characterization of pure and indium doped SnO₂ nanoparticles by sol-gel methods. *International Journal of Scientific and Engineering Research*, 7, 310-317.
158. Boddolla, S. and Thodeti, S. (2018). A review on characterization techniques of nanomaterials. *International Journal of Engineering, Science and Mathematics*, 7(1), 169-175.
159. Khan, H., Yerramilli, A. S., D'Oliveira, A., Alford, T. L., Boffito, D. C. and Patience, G. S. (2020). Experimental methods in chemical engineering: X-ray diffraction spectroscopy—XRD. *The Canadian Journal of Chemical Engineering*, 98(6), 1255-1266.
160. Ali, A., Chiang, Y. W. and Santos, R. M. (2022). X-ray diffraction techniques for mineral characterization: a review for engineers of the fundamentals, applications, and research directions. *Minerals*, 12(2), 205.
161. Waseda, Y., Matsubara, E. and Shinoda, K. (2011). *X-ray diffraction crystallography: introduction, examples and solved problems*. Berlin: Springer.
162. Tun, K. P. P. (2019). XRD and SEM Analysis, and Semiconductor Type Determination of TiO₂ for Dye-sensitized Solar Cell. *Science*, 4(2), 103-107.
163. Fatimah, S., Ragadhita, R., Al Husaeni, D. F. and Nandiyanto, A. B. D. (2022). How to calculate crystallite size from x-ray diffraction (XRD) using Scherrer method. *ASEAN Journal of Science and Engineering*, 2(1), 65-76.
164. He, K., Chen, N., Wang, C., Wei, L. and Chen, J. (2018). Method for determining crystal grain size by x-ray diffraction. *Crystal Research and Technology*, 53(2), 1700157.
165. Velumani, S., Mathew, X. and Sebastian, P. J. (2003). Structural and optical characterization of hot wall deposited CdSexTe1-x films. *Solar Energy Materials and Solar Cells*, 76(3), 359-368.
166. Salman, O. N., ALIa, M. D. A., Ahmed, D. And Hassoon, K. (2017). Low cost synthesis of ZnO nano thin films by electrochemical deposition. *Digest Journal of Nanomaterials and Biostructures*, 12, 719-726.
167. Picollo, M., Aceto, M. and Vitorino, T. (2019). UV-Vis spectroscopy. *Physical Sciences Reviews*, 4(4), 1-12.
168. Tissue, B. M. (2002). Ultraviolet and visible absorption spectroscopy. In *Characterization of Materials*. New York: John Wiley & Sons.

169. Internet: Tom, J. (2021). *UV-Vis spectroscopy: principle, strengths and limitations and application*. Web: <https://www.technologynetworks.com/analysis/articles/uv-vis-spectroscopy-principle-strengths-and-limitations-and-applications-349865>, Erişim tarihi: 07.06.2022.
170. De Caro, Cosimo & Claudia, Haller. (2015). *UV/VIS spectrophotometry - fundamentals and applications*. Ohio: Mettler-Toledo Publication.
171. Jassim, S. A. J., Zumaila, A. A. R. A. and Al Waly, G. A. A. (2013). Influence of substrate temperature on the structural, optical and electrical properties of CdS thin films deposited by thermal evaporation. *Results in Physics*, 3, 173-178.
172. M. Hussein, A., Dannoun, E. M., Aziz, S. B., Brza, M. A., Abdulwahid, R. T., Hussien, S. A., Rostam, S., Mustafa, D.M.T. and Muhammad, D. S. (2020). Steps toward the band gap identification in polystyrene based solid polymer nanocomposites integrated with tin titanate nanoparticles. *Polymers*, 12(10), 2320.
173. Tebyetekerwa, M., Zhang, J., Xu, Z., Truong, T. N., Yin, Z., Lu, Y., Ramakrishna, S., Macdonald, D. and Nguyen, H. T. (2020). Mechanisms and applications of steady-state photoluminescence spectroscopy in two-dimensional transition-metal dichalcogenides. *ACS nano*, 14(11), 14579-14604.
174. Zheng, T., Fan, B., Zhao, Y., Jin, B., Fan, L. and Peng, R. (2021). Tailored conductive fullerenes-based passivator for efficient and stable inverted perovskite solar cells. *Journal of Colloid and Interface Science*, 598, 229-237.
175. Titus, D., Samuel, E. J. J. and Roopan, S. M. (2019). Nanoparticle characterization techniques. In *Green synthesis, characterization and applications of nanoparticles* (pp. 303-319). Amsterdam: Elsevier.
176. Datta, S., Dey, A., Singha, N. R. and Roy, S. (2020). Enhanced performance of dye-sensitized solar cell with thermally stable natural dye-assisted TiO₂/MnO₂ bilayer-assembled photoanode. *Materials for Renewable and Sustainable Energy*, 9(4), 1-11.
177. González-Castillo, J. R., Rodriguez, E., Jimenez-Villar, E., Rodríguez, D., Salomon-García, I., de Sá, G. F., Fernandez, G., Almeida, D.B., Cesar, C.L., Johnes, R. and Ibarra, J. C. (2015). Synthesis of Ag@ Silica nanoparticles by assisted laser ablation. *Nanoscale Research Letters*, 10(1), 1-9.
178. Riabinina, D., Chaker, M. and Margot, J. (2012). Dependence of gold nanoparticle production on pulse duration by laser ablation in liquid media. *Nanotechnology*, 23(13), 135603.
179. Raj, S., Rai, P., Majhi, S. M. and Yu, Y. T. (2014). Morphology controlled Ag@ SiO₂ core-shell nanoparticles by ascorbic acid reduction. *Journal of Materials Science: Materials in Electronics*, 25(3), 1156-1161.
180. Internet: Al-Obaidi, D. H., Mahmood, O. A., Habeeb, A. A. and Abdullah, M. Z.(2022). Preparation and investigation of gold nanoparticles by the technique of laser ablation for biological application. Web: <http://dspace.unimap.edu.my/xmlui/handle/123456789/76325>, Erişim tarihi: 04.08.2022.

181. Bai, Z., Chen, R., Si, P., Huang, Y., Sun, H. and Kim, D. H. (2013). Fluorescent pH sensor based on Ag@ SiO₂ core-shell nanoparticle. *ACS Applied Materials & Interfaces*, 5(12), 5856-5860.
182. Singh, S., Bharti, A. and Meena, V. K. (2015). Green synthesis of multi-shaped silver nanoparticles: optical, morphological and antibacterial properties. *Journal of Materials Science: Materials in Electronics*, 26(6), 3638-3648.
183. M. H. Jaduaa, A. N. Abd, D. J. Hussein, and M. H. Jaduaa Alzubaidy. (2017). Silver Nanoparticles (Ag NP s) Prepared By Laser Ablation In Ethanol . *Journal of Multidisciplinary Engineering Science Studies*. Vol. 3 Issue 7.
184. Alnayli, R. S. and Alkazaali, H. (2019). Properties studies of silver nanoparticles colloids in ethanol prepared by means pulses laser. *Journal of Nano Research*, 60(1), 154-161
185. Samson, D., Adeeko, T. and Makama, E. (2017). Synthesis and optical characterization of silver nanoparticles (Ag-NPs) thin films (TFs) prepared by silar technique. *International Journal of Current Research and Academic Review*, 5(12), 15-24.
186. Abedini, A., Susthitha Menon, P., Daud, A. R., Hamid, M. A. A. and Shaari, S. (2016). Radiolytic formation of highly luminescent triangular Ag nanocolloids. *Journal of Radioanalytical and Nuclear Chemistry*, 307(2), 985-991.
187. Kang, J., Li, Y., Chen, Y., Wang, A., Yue, B., Qu, Y., Zhao, Y. and Chu, H. (2015). Core-shell Ag@ SiO₂ nanoparticles of different silica shell thicknesses: Preparation and their effects on photoluminescence of lanthanide complexes. *Materials Research Bulletin*, 71, 116-121.
188. Lévy, A., de Anda Villa, M., Laurens, G., Blanchet, V., Bozek, J., Gaudin, J., Lamour, E., Mace, S., Mignon, P., Milosavljevic, A., Nicolas, C., Patanen, M., Prigent, C., Robert, E., Steydii, S., Trassinell, M., Vernhet, D., Veteleinen, O. and Amans, D. (2021). Surface chemistry of gold nanoparticles produced by laser ablation in pure and saline water. *Langmuir*, 37(19), 5783-5794.
189. Martinez Pancorbo, P., Thummavichai, K., Clark, L., Tabish, T. A., Mansfield, J., Gardner, B., Chang, H., Stone, N. and Zhu, Y. (2019). Novel AU-SIO₂-WO₃ core-shell composite nanoparticles for surface-enhanced raman spectroscopy with potential application in cancer cell imaging. *Advanced Functional Materials*, 29(46), 1903549.
190. Alluhaybi, H. A., Ghoshal, S. K., Shamsuri, W. W., Alsobhi, B. O., Salim, A. A. and Krishnan, G. (2019). Pulsed laser ablation in liquid assisted growth of gold nanoparticles: Evaluation of structural and optical features. *Nano-Structures & Nano-Objects*, 19, 100355.
191. Ismail, R. A., Hamoudi, W. K. and Abbas, H. F. (2018). Synthesis of Au nanoparticles-decorated CdS nanowires via laser ablation in liquid for optoelectronic applications. *Applied Physics A*, 124(10), 1-8.

192. Peter, J., Backialakshmi, M., Karpagavinayagam, P. and Vedhi, C. (2014). Green synthesis and characterization of colloidal gold nanoparticles for optical properties. *Journal of Advanced Chemical Sciences*, 1-5.
193. Mallikarjuna, K., Sushma, N. J. and Deva Prasad Raju, B. (2013). Novel, fast, bio-derivatized sonochemical synthesis of gold nanoparticles by using Piper betle leaf broth as a reducing and capping agent. *In Advanced Nanomaterials and Nanotechnology* (pp. 41-49). Berlin: Springer.
194. Mosiori, C. O., Njoroge, W. K. and Ochoo, L. O. (2017). Optical Analysis of Ag-NPs Containing Methyl Ammonium Lead Tri-Iodide Thin Films. *Traektoriâ Nauki= Path of Science*, 3(9), 26-36.
195. Majeed, M. S., Hassan, S. M. and Fadhil, S. A. (2022). AgO Nanoparticles Synthesis by Different Nd: YAG Laser Pulse Energies. *Lasers in Manufacturing and Materials Processing*, 1-13.
196. Jamaludin, N., Chaudhary, K. T., Haider, Z., Duralim, M., Ismail, F. D., Roslan, M. S., Amira, N.H. and Ali, J. (2020). Effect of laser energy and wavelength on average size of gold nanoparticles synthesized by pulsed laser ablation in deionized water. *Journal of Physics: Conference Series*, 1484(1), 012029
197. Manikandan, V. S., Palai, A. K., Mohanty, S. and Nayak, S. K. (2018). Surface plasmonic effect of Ag enfold ZnO pyramid nanostructured photoanode for enhanced dye sensitized solar cell application. *Ceramics International*, 44(17), 21314-21322.
198. Solaiyammal, T. and Murugakoothan, P. (2019). Green synthesis of Au and the impact of Au on the efficiency of TiO₂ based dye sensitized solar cell. *Materials Science for Energy Technologies*, 2(2), 171-180.
199. Rho, W. Y., Kim, H. S., Chung, W. J., Suh, J. S., Jun, B. H. and Hahn, Y. B. (2018). Enhancement of power conversion efficiency with TiO₂ nanoparticles/nanotubes-silver nanoparticles composites in dye-sensitized solar cells. *Applied Surface Science*, 429, 23-28.
200. Ghahremanirad, E., Olyaei, S. and Hedayati, M. (2019, March). The influence of embedded plasmonic nanostructures on the optical absorption of perovskite solar cells. *Photonics* 6(2), 237
201. Liu, Q., Wei, Y., Shahid, M. Z., Yao, M., Xu, B., Liu, G., Jiang, K. and Li, C. (2018). Spectrum-enhanced Au@ ZnO plasmonic nanoparticles for boosting dye-sensitized solar cell performance. *Journal of Power Sources*, 380, 142-148.



GAZİ GELECEKTİR..